

Numerical simulation of foam flow in porous media

van der Meer, Jakolien

DOI

[10.4233/uuid:c64d0e63-9e2f-406c-930d-ae33cc077edb](https://doi.org/10.4233/uuid:c64d0e63-9e2f-406c-930d-ae33cc077edb)

Publication date

2018

Document Version

Final published version

Citation (APA)

van der Meer, J. (2018). *Numerical simulation of foam flow in porous media*. [Dissertation (TU Delft), Delft University of Technology]. <https://doi.org/10.4233/uuid:c64d0e63-9e2f-406c-930d-ae33cc077edb>

Important note

To cite this publication, please use the final published version (if applicable). Please check the document version above.

Copyright

Other than for strictly personal use, it is not permitted to download, forward or distribute the text or part of it, without the consent of the author(s) and/or copyright holder(s), unless the work is under an open content license such as Creative Commons.

Takedown policy

Please contact us and provide details if you believe this document breaches copyrights. We will remove access to the work immediately and investigate your claim.

NUMERICAL SIMULATION OF FOAM FLOW IN POROUS MEDIA

NUMERICAL SIMULATION OF FOAM FLOW IN POROUS MEDIA

Proefschrift

ter verkrijging van de graad van doctor
aan de Technische Universiteit Delft,
op gezag van de Rector Magnificus prof. dr. ir. T.H.J.J. van der Hagen,
voorzitter van het College voor Promoties,
in het openbaar te verdedigen op 31 januari 2018 om drie uur

door

Jakolien Marianne VAN DER MEER

Master of Science in Applied Mathematics,
Rijksuniversiteit Groningen,
geboren te 's-Gravenhage, Nederland.

Dit proefschrift is goedgekeurd door de

promotor: Prof. dr. ir. J.D. Jansen

copromotor: Dr. M. Möller

Samenstelling promotiecommissie:

Rector Magnificus,	voorzitter
Prof. dr. ir. J.D. Jansen	Technische Universiteit Delft
Dr. M. Möller	Technische Universiteit Delft
Dr. J.F.B.M. Kraaijevanger	Technische Universiteit Delft/ Radboud Universiteit Nijmegen, hiervoor Shell Projects & Technology

Onafhankelijke leden:

Prof. dr. W.R. Rossen	Technische Universiteit Delft
Prof. dr. ir. C. Vuik	Technische Universiteit Delft
Prof. dr. ir. A.W. Heemink	Technische Universiteit Delft
Prof. dr. R.J. Schotting	Universiteit Utrecht

This research was carried out within the context of the Recovery Factory project at TU Delft, sponsored by Shell Global Solutions International.

Keywords: Foam flow in porous media, Local-equilibrium models, Finite volume methods, Stability analysis, Reservoir simulation

Printed by: Gildeprint, Enschede

Cover design: Estel Alcaraz

Copyright © 2017 by J.M. van der Meer

ISBN 978-94-6233-863-0

An electronic version of this dissertation is available at

<http://repository.tudelft.nl/>.

*It is not knowledge, but the act of learning,
not possession but the act of getting there,
which grants the greatest enjoyment.*

Carl Friedrich Gauss

*Sometimes, immersed in his books,
there would come to him the awareness of all that he did not know,
of all that he had not read;
and the serenity for which he labored was shattered
as he realized the little time he had in life to read so much,
to learn what he had to know.*

John Williams, Stoner

CONTENTS

Summary	xi
Samenvatting	xiii
References	xv
1 Introduction	1
1.1 Foam Enhanced Oil Recovery	1
1.1.1 Population balance models	2
1.1.2 Local equilibrium models	3
1.1.3 Combining the two classes	7
1.2 Stability problems.	7
1.3 Numerical Approach	8
1.4 Research Objective and Questions	9
1.5 Thesis Outline	10
References	10
2 Discretization schemes for the simulation of foam EOR	13
2.1 Introduction	14
2.2 Mathematical model	14
2.2.1 Conservation law	14
2.2.2 Foam model	15
2.2.3 Non-dimensional formulation	17
2.3 Numerical oscillations	18
2.4 Heat equation with a discontinuous conductivity.	19
2.4.1 Temporal oscillations	22
2.5 Foam model with a discontinuous mobility.	24
2.5.1 Finite volume scheme using an integral average	24
2.6 Discussion and Conclusion	26
References	26
3 Mimetic discretisation schemes for generic phase change problems	35
3.1 Introduction	37
3.2 Generic model for phase change problems	39
3.3 Survey of existing numerical schemes.	40
3.3.1 Fixed grid methods: Enthalpy formulation.	40
3.3.2 Deforming grid methods: Front tracking.	41
3.3.3 Mimetic schemes	42

3.4	Development & Analysis of new mimetic schemes	44
3.4.1	Fourth mimetic schemes	45
3.4.2	Fifth mimetic schemes	49
3.4.3	Shifting the grid interface	50
3.5	Numerical examples	50
3.5.1	Example 1: Freezing of water	50
3.5.2	Example 2: Strongly degenerate problem	56
3.5.3	Example 3: Foam model	57
3.6	Conclusions	60
	References	61
4	High-Order Simulation of Foam Enhanced Oil Recovery	71
4.1	Introduction	72
4.2	Mathematical model	73
4.2.1	State variables and parameters	73
4.2.2	Conservation law	73
4.2.3	Foam model	73
4.2.4	Scaling the model	74
4.3	Numerical methods	75
4.3.1	Hyperbolic equation	76
4.3.2	Source term	77
4.3.3	Elliptic equation	78
4.4	Results	78
4.4.1	Case 1: gravity override	78
4.4.2	Case 2: viscous fingering	80
4.5	Conclusions	82
4.6	Acknowledgements	82
	References	82
5	The stability characteristics of foam flow in porous media	85
5.1	Introduction	87
5.2	Foam model	88
5.3	Linear stability analysis	91
5.4	Stability characteristics	92
5.5	Numerical methods	97
5.6	Numerical results	98
5.6.1	Test case 1	98
5.6.2	Test case 2	99
5.6.3	Test case 3	99
5.6.4	Test case 4	99
5.6.5	Reference cases without foam	99
5.7	Numerical stability analysis	100
5.8	Additional test cases	103
5.8.1	Test case 5 and 6	104
5.8.2	Test case 7	104
5.8.3	Test case 8 and 9	104

5.8.4	Test case 10	105
5.8.5	Numerical stability analysis	106
5.9	Conclusions.	106
5.10	Acknowledgements	109
	References	109
6	Conclusions and discussion	115
6.1	Conclusions.	115
6.1.1	Non-linear heat equation with a discontinuous coefficient	115
6.1.2	Local-equilibrium foam model.	116
6.1.3	Summary	118
6.2	Suggestions for future research	118
6.2.1	Improved model for gas-foam front	118
6.2.2	Adaptive grid methods.	119
6.2.3	Bubble-flow models for porous media	119
6.2.4	Influence of oil on the stability of foam EOR	119
	References	119
	Acknowledgements	123
A	Appendix A: Derivation two-phase flow equations	125
A.1	Conservation laws	125
A.2	Two-phase flow	125
A.3	Non-dimensional formulation	126
	References	128
B	Appendix B: Derivation perturbation equations	129
	References	131
C	Appendix C: Model parameters	133
	References	134
	Curriculum Vitae	135
	List of Publications	137

SUMMARY

If secondary hydrocarbon recovery methods, like water flooding, fail because of the occurrence of viscous fingering one can turn to an enhanced oil recovery method (EOR) like the injection of foam. The generation of foam in a porous medium can be described by a set of partial differential equations with strongly non-linear functions, which impose challenges for the numerical modeling. Former studies [1–3] show the occurrence of strongly temporally oscillating solutions when using forward simulation models, that are entirely due to discretization artifacts. We describe the foam process by an immiscible two-phase flow model where gas is injected in a porous medium filled with a mixture of water and surfactants. The change from pure gas into foam is incorporated in the model through a reduction in the gas mobility. Hence, the two-phase description of the flow stays intact. Since the total pressure drop in the reservoir is small, both fluids can be considered incompressible [3]. However, whereas the fractional flow function for a gas-flooding process is a smooth function of water saturation, the generation of foam will cause a rapid increase of the flux function over a very small saturation scale. Consequently, the derivatives of the flux function can become extremely large and impose a severe constraint on the time step. We address the stability issues of the foam model, by numerous numerical approaches that improve the accuracy of the solutions. First, we study several averaging schemes and introduce a novel way of approximating the foam mobility functions on the grid interfaces in a finite volume framework. This will lead to solutions that are significantly smoother than can be achieved with standard averaging schemes. Next, we discuss several novel discretization schemes where the discontinuity is incorporated in the numerical fluxes for a simplified compressible flow model. These include the indirect addition of an extra grid interface at the location of the discontinuity, to preserve monotonicity of the solutions in time. Variations on this method, are the addition of an extra grid cell around the highly non-linear phase transition and the adaption of the flux terms based on the location of the discontinuity or non-linearity in the grid. As a practical example to demonstrate these techniques we study a simplified model for foam flow in porous media. The model is then extended to a two-dimensional reservoir, where the accuracy of the solutions is a main concern. The two-dimensional simulator that is used for this, was build and tested for the foam model. It includes higher-order hyperbolic Riemann solvers, and flux correction schemes to compute the saturation of the different fluid phases in the model. The elliptic solver for the pressure equation is also adapted to the stiffness of the problem. With this simulator we perform a quantitative study of the stability characteristics of the flow, to gain more insight in the important wave-lengths and scales of the foam model. This insight forms an essential step towards the design of a suitable computational solver that captures all the appropriate scales, while retaining computational efficiency. In addition, we present a qualitative analysis of the effect of different reservoir and fluid properties on the foam fingering behavior. In particular, we consider the effect of heterogeneity of the reservoir,

injection rates, and foam quality. This leads to interesting observations about the influence of the different foam parameters on the stability of the solutions, and we are able to predict the flow stability for different foam qualities. Finally, we discuss several other approaches that were addressed during this PhD-project to increase the understanding of solving highly non-linear flow problems in a porous medium.

SAMENVATTING

Als secundaire oliewinningsmethoden, zoals waterinjectie in een oliereservoir, falen als gevolg van het optreden van visceuse instabiliteiten tussen vloeistoffen, kan men kijken naar een verbeterde oliewinningsmethode (EOR) zoals schuiminjectie. De formatie van schuim kan worden beschreven door een reeks partiële differentiaalvergelijkingen met sterk niet-lineaire variabelen. Deze niet-lineariteiten kunnen leiden tot numerieke problemen. Eerdere studies [1–3] tonen dat de numerieke oplossingen van voorwaardse simulatiemodellen sterk oscilleren in de tijd. Deze oscillaties worden geheel veroorzaakt door de discretisatie van het model en zijn dus niet fysische verschijnselen. We beschrijven het schuimproces door een stromingsmodel van twee niet-mengbare fases, namelijk gas en water. Het gas wordt geïnjecteerd in een poreus medium gevuld met een mengsel van water en oppervlakte-actieve stoffen. De verandering van zuiver gas in schuim is in het model opgenomen door de gasmobiliteit drastisch te verminderen. Vandaar dat de twee-fase beschrijving intact blijft. Aangezien de totale drukval in het reservoir klein is, kunnen beide vloeistoffen worden beschouwd als onsamendrukbaar [3]. Hoewel de fractionele fluxfunctie voor een gasinjectieproces een gladde functie van de waterverzadiging is, zal het ontstaan van schuim een snelle toename van de fluxfunctie op een zeer kleine verzadigingschaal veroorzaken. Derhalve kunnen de afgeleiden van de fluxfunctie extreem groot worden, zodat heel kleine tijdstappen gebruikt moeten worden. Wij behandelen de stabiliteitsproblemen van het schuimmodel door talrijke numerieke benaderingen die de nauwkeurigheid van de oplossingen verbeteren. Ten eerste onderzoeken we een aantal middelingsmethodieken en introduceren een nieuwe manier om de schuimmobiliteitsfuncties op de randen van het numerieke raster te benaderen doormiddel van eindige-volume methoden. Vervolgens bespreken we een aantal nieuwe discretisatieschemas waarbij de discontinuïteit in de numerieke fluxfunctie is opgenomen voor een vereenvoudigd samendrukbaar stromingsmodel. Het gaat hierbij om de indirecte toevoeging van een extra rasterlijn op de locatie van de discontinuïteit, voor het behoud van de monotonie van de oplossingen in de tijd. Variaties op deze methode zijn de toevoeging van twee extra rasterlijnen rond de sterk niet-lineaire faseovergang en de aanpassing van de fluxtermen op basis van de locatie van de discontinuïteit of de niet-lineariteit in het raster. Als een praktisch voorbeeld om deze technieken te demonstreren bestuderen we een vereenvoudigd stromingsmodel van schuim in een één-dimensionaal poreus medium. Het model wordt vervolgens uitgebreid naar een schuimmodel toegepast op een twee-dimensionaal reservoir, waar de nauwkeurigheid van de verschillende oplossingen onder de loep wordt genomen. De twee-dimensionale simulator die hiervoor wordt gebruikt, werd speciaal ontworpen en getest voor dit schuimmodel. De simulator bevat hogere-orde hyperbolische Riemann oplossingsmethoden en flux-correctie schemas voor het berekenen van de verzadiging van de verschillende fases in het model. De elliptische oplossingsmethode voor de drukvergelijking is ook aangepast aan de stijfheid van het probleem. Met

deze simulator voeren we een kwantitatieve studie uit naar de stabiliteitskarakteristieken van de stroming, om meer inzicht te krijgen in de belangrijke golflengtes en schalen van het schuimmodel. Dit inzicht vormt een essentiële stap naar het ontwerp van een geschikte numerieke oplossingsmethode die alle juiste schalen meeneemt met behoud van rekenkundige efficiëntie. Daarnaast presenteren wij een kwalitatieve analyse van het effect van de verschillende reservoir- en vloeistof-eigenschappen op de stabiliteit en het gedrag van het schuim. In het bijzonder kijken we naar het effect van de reservoir-heterogeniteit, injectiesnelheden en kwaliteit van het schuim. Dit leidt tot interessante observaties over de invloed van verschillende schuimparameters op de stabiliteit van de oplossingen, waarmee een voorspelling kan worden gemaakt over de stabiliteit van de stromingen voor verschillende schuimkwaliteiten. Tenslotte bespreken we verschillende andere benaderingen die tijdens dit PhD-project werden aangepakt om het begrip van zeer niet-lineaire stromingsproblemen in een poreus medium te vergroten.

REFERENCES

- [1] M. Namdar Zanganeh, *Simulation and optimization of foam EOR processes*, [Ph.D. thesis](#), Delft University of Technology (2011).
- [2] E. Ashoori, *Foam for Enhanced Oil Recovery: Modeling and Analytical Solutions*, [Ph.D. thesis](#), Delft University of Technology (2012).
- [3] T. N. Leeftink, C. A. Latooij, and W. R. Rossen, *Injectivity errors in simulation of foam EOR*, [Journal of Petroleum Science and Engineering](#) **126**, 26 (2015).

1

INTRODUCTION

1.1. FOAM ENHANCED OIL RECOVERY

Foam was first applied in the oil industry in the late 1950s to decrease gas mobility and hence reduce the undesirable effect of viscous fingering and gravity override in subsurface porous media flow [1]. To generate foam in a subsurface oil reservoir, usually a mixture of chemicals (surfactants) and water is injected into the reservoir, which together with the injected gas forms a foam. These chemicals make a large contribution to the production costs, and therefore, the goal is to minimize their amount. To determine the required amount of chemicals for an economically profitable production level and to decide on the optimal chemical composition of the surfactants for the site-specific rock and fluid properties, reliable simulations are needed [2].

There are several models describing foam flow in porous media to answer this need. However, they are not always based on the same principles or parameters. For example, the exact time that it takes to form the foam is under discussion because it is difficult to determine experimentally. Also the influence of oil on the strength of the foam is not sufficiently understood. Here we offer a short overview of the different models that are used to simulate foam enhanced oil recovery (EOR) processes.

We can roughly distinguish between two classes of foam models: dynamic population balance models that take into account the strength (bubble size) of the foam and local equilibrium methods that incorporate the effect of the foam through a limit function¹.

The first class of models tries to capture the real dynamics of the process, while the second class assumes that there is only one equilibrium in foam strength. Because of the complex nature of the foam the first class is more complex and has a higher number of degrees of freedom than the second class. From a computational point of view the second class of models is therefore more suitable to perform large simulations of a reservoir in less time, and hence, very useful for test purposes.

¹There is also an additional class of (semi-)empirical models, but we do not take them into account here.

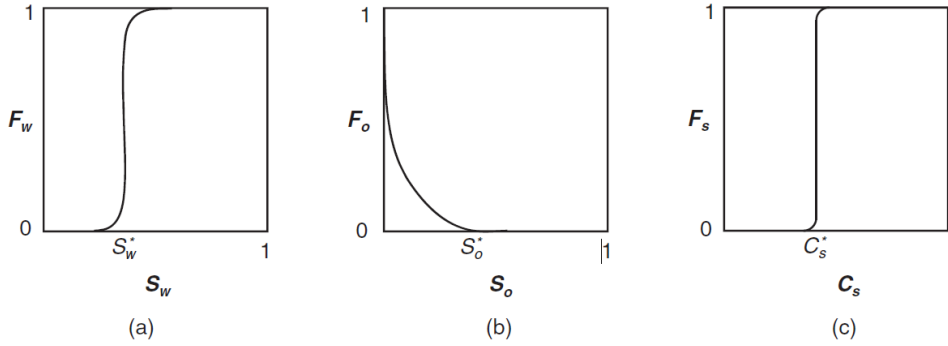


Figure 1.1: Sensitivity of foam to (a) water, (b) oil, (c) surfactant concentration (from Namdar Zanganeh and Rossen [4])

1.1.1. POPULATION BALANCE MODELS

We will first consider the class of population balance models. In these models foam is considered as a collection of bubbles or lamellae, which are conserved during the simulation. The rate of growth of the lamellae depends on several mechanisms such as influx rate, efflux, creation, destruction and trapping of lamellae [3]. So besides the conservation of fluids (gas, water and oil) there is an additional equation describing the conservation of (the dimensionless) lamellae or bubble density n_D , given by

$$\frac{\partial n_D}{\partial t} = -\nabla \cdot (f(n_D)) + q(n_D), \quad (1.1)$$

where f is the flux function and the creation and destruction of the bubbles is described by incorporating the source term q in the conservation equation. The mobility of the gas in a foam is controlled by the bubble density as follows

$$k_{rg}^f = \frac{k_{rg}^0}{\mu_g^f}, \quad \mu_g^f = h(\mu_g^0, n_D), \quad (1.2)$$

where k_{rg}^f and k_{rg}^0 are the relative permeability of the gas in a foam and in its original form respectively, μ_g^f is the foam viscosity and h is a function of the original gas viscosity and the bubble density.

Simulations with these kind of models show that there exist several equilibrium solutions for a certain parameter range corresponding to different strengths of the foam. The intermediate state was shown to be unstable both by experimental work [5] and numerical results [6]. There are different approaches to the definition of a foam in equilibrium. According to Kavscek *et al.* [7] lamellae are still constructed and destructed but the corresponding construction rates cancel out. This is based on the 'Roof' snap-off principle, where lamellae are continuously constructed and destructed [3]. By this principle, gas mobility, which is closely related to foam density [8], can undergo a sudden change. Others [5, 9–11] state that foam in a steady-state can only influence the mobility of gas by mobilization and division of the lamellae.

The gas mobility in a foam is strongly influenced by the bubble density. Stable foam has a larger bubble density (i.e. finer bubble texture) than foam in an unstable equilibrium. Since the gas mobility depends on the area over which the gas can flow and the pressure gradient in this area, smaller bubbles reduce the mobility more than larger bubbles. Hence, a stable foam has a larger reduction factor on the gas mobility [8].

The disadvantage of the population balance models is their complexity, because they lead to a large number of degrees of freedom and parameters. Finite volume methods have been applied to these models but are difficult to implement [3] and require a lot of computational power. Below we list some important population balance models that have been successfully used to simulate foam flow in porous media.

KAM AND ROSSEN (2003)

Kam and Rossen [12] assumed that the sudden jump in the gas mobility during foam formation is due to the mobilization and division of lamellae [5]. The process of division of lamellae is only possible if the pressure gradient is large enough [8]. Hence the model assumes that bubble creation is controlled by the pressure gradient, which should exceed a minimum value. Since the model allows for bubble sizes smaller than the average pore size of the rock, a lower bound is imposed for the bubble size via an additional condition [3]. This model performs good for average pressure gradients, but exhibits numerical instabilities for large pressure gradients [3].

KAM *et al.* (2007)

In Kam *et al.* [6], the model introduced by Kam and Rossen [12] was improved by putting a constraint on the bubble creation rate for high pressure gradients,

$$\mu_g^f = \mu_g^0 + \frac{C_f n_{\max} n_D}{(\mu_g / \varphi S_g)^{1/3}}, \quad (1.3)$$

where C_f is a constant parameter that is adapted to the problem, S_g the gas volume fraction, φ the porosity of the medium, and n_{\max} is the minimum bubble size, which is related to the minimum pore size [3].

1.1.2. LOCAL EQUILIBRIUM MODELS

The second class of models is based on the assumption that the foam is always in a local equilibrium: either there is foam or there is no foam present at a certain point in space and time. When foam is present the gas mobility is reduced by a large factor, because the foam captures the gas in lamellae bubbles. The water mobility, on the contrary, is not influenced by the foam in these models. Hence, the mobility ratio between gas and water is reduced, leading to a smoother gas (or foam) front. The question then remains when we can expect the formation or destruction of foam, and which parameters govern this process. The models in this class are based on a conservation law, conserving the phases present (usually gas, water and oil) and it is assumed that the surfactant is solved in one of the former two phases. For the formation of foam we need at least gas, water and surfactant in sufficient amounts. Moreover, we assume that if the amount of oil present is high, foam will break down.

CONSERVATION LAW

Starting with a conservation law, we can define a basic model (without capillarity or gravitational forces) for the phase saturation (volume fraction) S_α for the phases $\alpha = w(\text{ater}), g(\text{as}), o(\text{il})$ in a porous medium:

$$\phi \frac{\partial S_\alpha}{\partial t} = -\nabla \cdot (f_\alpha \tilde{u}) + q_\alpha \quad (1.4)$$

where f_α is the fractional flow function, q_α the mass flow rate of the α -phase and the total Darcy velocity $\tilde{u} = \sum_{\alpha}^{N_\alpha} \tilde{u}_\alpha$ follows from Darcy's law for the fluid phase velocity

$$\tilde{u} = -K(\lambda \nabla p_w), \quad (1.5)$$

where p is the fluid pressure and λ is the total mobility given by $\lambda = \sum_{\alpha}^{N_\alpha} \lambda_\alpha$. The phase mobilities are given by

$$\lambda_\alpha = \frac{k_{r\alpha}(S_\alpha)}{\mu_\alpha}, \quad (1.6)$$

where ρ_α, μ_α and $k_{r\alpha}$ are the density, viscosity and the relative permeability of phase α , respectively. The fractional flow function of the wetting phase is defined by the fraction of the phase mobility and the total mobility

$$f_\alpha(S_\alpha) = \frac{\lambda_\alpha}{\lambda}. \quad (1.7)$$

MOBILITY REDUCTION FACTOR FOAM

If gas comes in contact with a sufficient amount of water and surfactants, a foam will form. This will cause a rapid decrease in the gas mobility, which can be modeled by decreasing the relative gas permeability function with a mobility reduction factor f_{mr} , so that

$$k_{rg} := \frac{k_{rg}^o}{f_{mr}}, \quad (1.8)$$

where k_{rg}^o is the relative gas permeability of the gas in its original state and

$$f_{mr} = 1 + R \cdot F_w \cdot F_o \cdot F_s, \quad (1.9)$$

where R is a constant that accounts for the maximum resistance of the flow to foam, and F_w, F_o, F_s are functions that describe the sensitivity of the foam to water, oil and surfactant concentration, respectively, as shown in Figure 1.1. The value of f_{mr} depends on the strength of the foam, being very large for strong foams and small for weak foams [3, 4, 13].

CRITICAL WATER SATURATION

First, we will neglect the influence of the oil by considering a two-phase model with only gas and water mixed with surfactants. Experimental results show that foam will form above a certain limiting water saturation S_w^* [14], so that

$$k_{rg} := \begin{cases} k_{rg}^g, & \text{if } S_w < S_w^*, \\ k_{rg}^f < k_{rg}^* < k_{rg}^g, & \text{if } S_w = S_w^*, \\ k_{rg}^f, & \text{if } S_w > S_w^*, \end{cases} \quad (1.10)$$

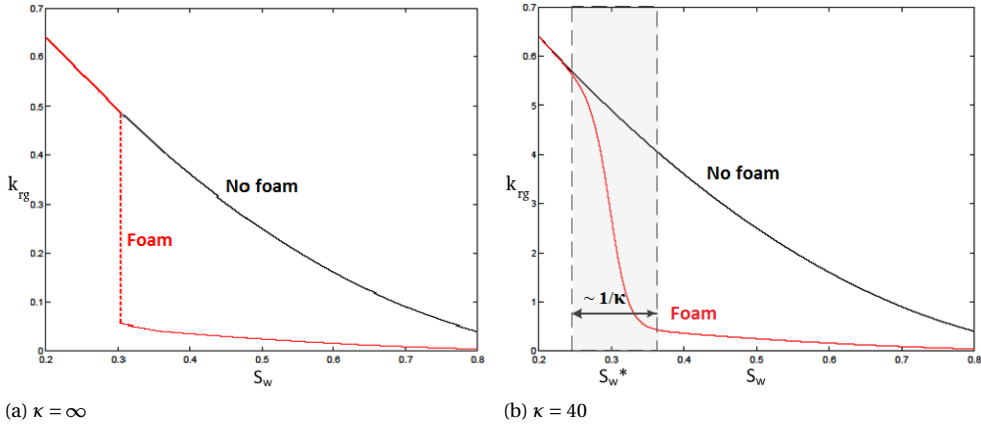


Figure 1.2: Relative permeability function for a model with foam (red line) and without foam (black line). In the right figure the sudden transition due to foam is approximated by a continuous function with a mollifying parameter $\kappa = 40$ and mobility reduction factor $f_{mr} = 10$.

where k_{rg}^g is the relative gas permeability of the gas, and k_{rg}^f is the relative foam permeability, which is much lower than that of gas. In Figure 1.2a the relative permeability function described here is plotted. The sudden jump in the mobility of the gas at S_w^* cannot be accurately incorporated in standard finite volume schemes. For this and other reasons, the jump in mobility is approximated by a continuous function. This function differs per model and we will list a few of them below.

CHENG *et al.* (2000)

The local-equilibrium foam model by [13], which is sometimes referred to as the STARS model [15], approximates the jump in the mobility by a continuous function, given by Eq. 1.8, 1.9 and

$$F_w = 0.5 + \frac{\arctan(\kappa(S_w - S_w^*))}{\pi}, \quad (1.11)$$

where S_w^* represents the limiting water saturation and κ is a positive parameter that controls the width of the gas-foam transition.

VAN DER MEER *et al.* (2014)

If we assume that f_{mr} is a constant factor equation 1.10 can be rewritten as follows

$$k_{rg} := k_{rg}^o H(S_w^* - S_w) + \frac{1}{f_{mr}} k_{rg}^o H(S_w - S_w^*), \quad (1.12)$$

where H denotes the Heaviside step function given by

$$H(x) = \begin{cases} 0, & \text{if } x < 0, \\ 1, & \text{if } x \geq 0. \end{cases} \quad (1.13)$$

The Heaviside function $H: \mathbb{R} \rightarrow \{0, 1\}$ can be approximated by the C^{inf} continuous hyperbolic function

$$H_{\kappa}(x) = \frac{1}{2} + \frac{1}{2} \tanh \kappa x \quad (1.14)$$

The parameter $\kappa \gg 1$ describes the behavior of the function around S_w^* , and can be used as a mollifying parameter to make model less stiff as shown in Figure 1.2b

ASHOORI (2012)

To approximate the discontinuous jump given by equation (1.12), Ashoori [3] uses a function that is based on the population balance model. This function approximates the discontinuity in S_w^* by a C^0 continuous function given by Eq. 1.8 and

$$f_{mr}(S_w) = Rn_D^{LE}(S_w) + 1, \quad (1.15)$$

where R is a constant and n_D^{LE} is the dimensionless bubble density function in local equilibrium, which is defined as

$$n_D^{LE}(S_w) = \begin{cases} \frac{n_f^{LE}}{n_{\max}} = \tanh \kappa (S_w - S_w^*), & \text{if } S_w > S_w^*, \\ 0, & \text{if } S_w \leq S_w^*, \end{cases} \quad (1.16)$$

where n_f^{LE} is the local equilibrium foam density, n_{\max} the maximum foam density, and κ is a mollifying parameter controlling the steepness of the gas-foam transition.

NAMDAR ZANGANEH AND ROSSEN (2013)

A similar function as the former, which is also C^{inf} continuous, is used in Namdar Zanganeh and Rossen [4]. Here, the mobility reduction factor is given by Eq. 1.8, 1.9 and

$$F_w = \frac{1}{\pi} [\arctan(\kappa(S_w - S_w^*)) - \arctan(\kappa(S_{wr} - S_w^*))], \quad S_{wr} \leq S_w \leq (1 - S_{or}), \quad (1.17)$$

where S_{wr} is the residual water saturation and S_{or} the residual oil saturation. This approach ensures that there is no foam left once the saturation is below the residual saturation. The difference between the hyperbolic tangent ($\tanh(x)$) and arctangent ($\arctan(x)$) is negligible for small x , since they are similar up to the fourth order ($O(x^4)$).

CRITICAL SURFACTANT CONCENTRATION

Earlier in this chapter we assumed that there is always enough surfactant solution in the water to form a foam. This is not necessarily true, so instead we can also model surfactant concentration C_s separately. This implies that in certain parts of the reservoir, surfactant concentration will be lower than in other parts. For the generation of foam, at least a certain amount is required, called the critical surfactant concentration, which we denote by C_s^* . Consequently (assuming that $S_w > S_w^*$),

$$k_{rg} = \begin{cases} k_{rg}^0, & \text{if } C_s < C_s^* \\ k_{rg}^f < k_{rg}^* < k_{rg}^0, & \text{if } C_s = C_s^* \\ k_{rg}^f, & \text{if } C_s > C_s^*. \end{cases} \quad (1.18)$$

NAMDAR ZANGANEH AND ROSSEN (2013)

In [4], the effect of the surfactant concentration is defined by the following term,

$$F_s = \begin{cases} \left(\frac{C_s}{C_s^*}\right)^{n_s}, & \text{if } C_s \leq C_s^*, \\ 1, & \text{if } C_s > C_s^*, \end{cases} \quad (1.19)$$

where n_s controls the steepness of the transition between gas and foam, similar to the parameter κ .

CRITICAL OIL SATURATION

The model becomes more complicated if oil is added. Apart from having an extra conservation equation, we also have to take into account the devastating effect of oil on the foam. There has been little research on this issue, but it is assumed that too much oil can kill the foam, i.e. if the oil saturation is above some limit S_o^* , there will be no foam.

NAMDAR ZANGANEH AND ROSSEN (2013)

In [4], the factor describing the effect of the oil on foam is modeled by

$$F_o = \begin{cases} 1, & \text{if } S_o < S_o^*, \\ \left(\frac{S_o^* - S_o}{S_o^* - S_o^{**}}\right)^{n_o}, & \text{if } S_o^{**} \leq S_o < S_o^*, \\ 0, & \text{if } S_o^* \leq S_o \leq (1 - S_{wr}), \end{cases} \quad (1.20)$$

where n_o controls the steepness of the function and S_o^{**} is a lower oil saturation that accounts for the effect of oil on foam [4].

1.1.3. COMBINING THE TWO CLASSES

In her thesis, Ashoori [3] found that local equilibrium methods often perform just as good as population balance models, except at the entrance regions close to the injection well and at the shock front. To employ the advantages of both models at the same time, she applied a local equilibrium model in the smooth regions, while switching to a population balance model in the critical regions (shock, entrance region), where non-local equilibrium effects dominate. This strategy costs more implementation time but can result in a better accuracy and less computation time [3].

1.2. STABILITY PROBLEMS

The generation of foam will cause a rapid increase of the flux function over a very small saturation scale. Consequently, the derivatives of the flux function can become extremely large and impose a severe stability constraint on the numerical scheme [16]. Except for numerical constraints, foam also imposes a stability issue from a physical perspective, due to the very sensitive nature of foam relative to changes in physical variables, like water and oil saturation and surfactant concentrations. A small offset in the approximated saturation values can have a huge effect on the physical outcome of the simulations. We have to take this into account, when talking about the accuracy, convergence and predictive value of the foam simulations.

1.3. NUMERICAL APPROACH

The accuracy and stability of the solutions are strongly linked to the numerical solver. We have to look at both the suitability of the numerical solver to the given problem and the suitability of the model, like well-posedness and its physical meaning. The stability problems we are facing for the studied foam model are not restricted to this model, but include a wider class of hyperbolic-elliptic or parabolic problems that contain a discontinuity or highly non-linear transition in the diffusion term. We therefore start by exploring a parabolic problem that has a single discontinuity in the diffusion coefficient, and hence is not well defined at this point. To address this, we need to redefine the problem as two differential equations, each representing the phase left and right of the discontinuity, and enforce stability conditions at the interface between those two problems. This is also called a moving-interface or Stefan problem in literature [17–19]. It occurs when a phase change happens, for example a liquid turning into a solid. For such a problem, an additional Stefan-condition is needed at the phase interface to make the numerical model well-posed.

The transition from gas to foam could be viewed as such, when considering foam as a gas that turns into another phase by the addition of some water and surfactant, whose total volume is negligible (see f.e. Rossen *et al.* [14]). Physically, this makes sense, since the mobility and thermal properties of foam are more like that of a liquid moving through a porous medium than a gas. When we take into account that foam breakage occurs locally, whenever the local capillary pressure exceeds a critical value, we can see some similarities with ordinary liquid-gas phase change problems (for example, the condensation of water). The critical capillary pressure, which is strongly linked with the critical water saturation and critical surfactant concentration [20, 21], defines the location of the moving interface between gas and foam. Hence, when we reformulate the gas-foam transition as a moving-interface or Stefan problem, we can choose an appropriate numerical solver, to simulate the foam process.

There are roughly two classes of numerical solvers that can handle Stefan-like problems. The first class are the fixed-grid methods [19] that use an enthalpy formulation to find a solution. The advantage of those schemes is that the interface does not need to be tracked, since the Stefan condition is indirectly included in the enthalpy formulation. This means that a fixed grid can be used. The second class, called the deforming grid methods, includes the adaptive grid methods, that track or approximate the interface location, and do so by either adding additional grid points around the moving interface, or use level-set techniques. We propose an alternative to those methods that approximate the interface location, and indirectly include an extra grid interface or grid cell at the phase interface. This grid cell or interface is then used to update the fluxes through the grid interfaces surrounding the phase interface. Hence, oscillatory behavior of the solution is decreased, without changing the grid. Therefore, this does not require any major additional computational effort, as in the adaptive grid methods. We also study the effect of smart averaging schemes on the solutions, which does not involve approximation or tracking of the phase interface. The disadvantage of the proposed scheme is that it is very grid-dependent, whereas the addition of a grid interface or grid cell is less grid-dependent.

To test these numerical schemes we developed a one-dimensional solver in MATLAB

to solve a parabolic problem involving a phase change, and a one-dimensional solver in C++ to solve the local-equilibrium foam model. Those solvers are based on finite volume methods in space, and make use of both first-order and second-order time integration methods. We also developed a two-dimensional foam simulator in C++ that can handle highly non-linear flux functions, without adding additional numerical diffusion [2]. A first-order upwind scheme might be stable but introduces a lot of numerical diffusion around the shock front. In order to improve the accuracy near the foam front we make use of a higher-order total variation diminishing (TVD) scheme that preserves the numerical stability of the solution. Two-dimensional simulations are then performed to examine the conditions under which foam exhibits viscous fingering behavior and gravity override. As an example, we use a two-dimensional quarter five-spot setup, where gas is injected at a constant injection rate via a well at the bottom-left corner and water and gas are produced at the same injection rate via the production well at the right-top corner (Chapter 4) and a horizontal injection and production well (Chapter 5).

1.4. RESEARCH OBJECTIVE AND QUESTIONS

The main objective of this thesis is to quantify and resolve the stability issues that arise due to highly non-linear flux functions in existing reservoir simulators that are based on mass-conservative finite volume schemes. So the main question is:

How to improve the accuracy and stability of the numerical solutions of the local-equilibrium foam model?

To answer this question, we study the local equilibrium foam model that was introduced in Section 1.1.2, with a mobility reduction factor given by Eq. 1.9 and 1.11, a constant amount of surfactants dissolved in the water and no oil present ($F_o = F_s = 1$)². To be able to understand the mathematics underlying the unstable numerical solutions of the foam model, we also study a simpler model, that is the non-linear heat equation with a piecewise continuous diffusivity. The conclusions we can draw from this study can be used to improve the numerical techniques applied to the local-equilibrium foam model. For each model studied, we derived a set of sub-questions "a posteriori", that will be addressed in the next chapters. These sub-questions can be categorized as follows:

Non-linear heat equation with a piecewise continuous coefficient

1. Is the equation well-posed? (Chapter 3)
2. How does a piecewise continuous diffusivity coefficient affect the numerical solutions of the equation? (Chapter 2, 3)
3. How can we improve the finite volume method to handle discontinuous coefficients in the equation? (Chapter 2, 3)

²This model was derived from the model in Cheng *et al.* [13]. In the rest of this thesis, we will refer to this model when talking about the local-equilibrium foam model.

Local-equilibrium foam model

4. How does a highly non-linear diffusion coefficient affect the numerical solutions of the model? (Chapter 2)
5. What is the cause of the temporal oscillations observed in the numerical solutions of the model? (Chapter 2, 3)
6. What is the connection between the non-linear heat-equation with a piecewise continuous coefficient and the local-equilibrium foam model, and what can we learn from that? (Chapter 3)
7. How can we improve the numerical solutions of the model? (Chapter 2, 3, 4, 5, 6)
8. What is the effect of foam on the two-dimensional solutions of the model? (Chapter 4, 5)
9. How stable and accurate are the solutions of the model in two dimensions? (Chapter 4, 5)
10. How suitable is the model? Are there any suitable alternatives? (Chapter 6)

1.5. THESIS OUTLINE

In Chapter 2, we address the temporal stability of one-dimensional foam simulations, where we compare the stability of different averaging methods to approximate the parameters on a finite volume grid. We introduce a novel averaging approach for the considered model that smoothes out the oscillatory behavior observed for standard averaging procedures. This method is illustrated by applying it to a diffusion equation with a discontinuous diffusion coefficient and shows a significant improvement of the temporal stability of the solutions. In Chapter 3, we build further on this approach by examining different discretization and interpolation procedures that can be applied to parabolic equations with strongly non-linear or discontinuous coefficients. To make the link with the preceding chapter a parabolic diffusion equation describing the pressure decay of a foam in a porous medium is studied. This equation can be used to describe foam flow when coupled with an hyperbolic equation for the fluid saturations, and is extended to a two-dimensional reservoir model in Chapter 4. Here, we perform a qualitative study of the numerical stability of the foam simulations under the influence of different numerical and physical parameters. In Chapter 5, this is supported by a linear stability analysis of foam flow, to validate the numerical simulations and identify the important scales and wave lengths of the model. This lays the foundation for a tailor-made solver that can handle both the fast waves induced by the foam and the slow waves behind the foam front. In the conclusions in Chapter 6 we will come back to the research questions above, and summarize the results from this thesis.

REFERENCES

- [1] A. N. Fried, *United States Bureau of Mines Bulletin 5866*, Tech. Rep. (Bureau of Mines, 1961).

- [2] J. M. Van der Meer, D. E. A. Van Odyck, P. Wirnsberger, and J. D. Jansen, *High-order Simulation of Foam Enhanced Oil Recovery*, in *Proc. 14th European Conference on Mathematics in Oil Recovery (ECMOR XIV)* (Catania, 2014) pp. 8–11.
- [3] E. Ashoori, *Foam for Enhanced Oil Recovery: Modeling and Analytical Solutions*, Ph.D. thesis, Delft University of Technology (2012).
- [4] M. Namdar Zanganeh and W. R. Rossen, *Optimization of Foam Enhanced Oil Recovery: Balancing Sweep and Injectivity*, *SPE Reservoir Evaluation & Engineering* **16**, 51 (2013).
- [5] P. A. Gauglitz, F. Friedmann, S. I. Kam, W. R. Rossen, P. A. Gauglitz, S. Kam, and W. R. Rossen, *Foam generation in homogeneous porous media*, *Chemical Engineering Science* **57**, 4037 (2002).
- [6] S. Kam, Q. Nguyen, Q. Li, and W. R. Rossen, *Dynamic Simulations With an Improved Model for Foam Generation*, *SPE Journal* **12**, 35 (2007).
- [7] A. R. Kovscek, T. Patzek, and C. Radke, *Mechanistic Prediction of Foam Displacement in Multidimensions: A Population Balance Approach*, in *SPE/DOE Improved Oil Recovery Symposium* (Society of Petroleum Engineers, 1994).
- [8] A. H. Falls, G. J. Hirasaki, T. W. Patzek, P. A. Gauglitz, D. D. Miller, and T. Ratulowski, *Development of a Mechanistic Foam Simulator: The Population Balance and Generation by Snap-Off*, *SPE Reservoir Engineering*, 884 (1988).
- [9] W. R. Rossen and P. A. Gauglitz, *Percolation theory of creation and mobilization of foams in porous media*, *AIChE Journal* **36**, 1176 (1990).
- [10] T. Dickson, G. J. Hirasaki, and C. A. Miller, *Conditions for Foam Generation in Homogeneous Porous Media*, in *Proceedings of SPE/DOE Improved Oil Recovery Symposium* (Society of Petroleum Engineers, 2002).
- [11] W. R. Rossen, *A critical review of Roof snap-off as a mechanism of steady-state foam generation in homogeneous porous media*, *Colloids and Surfaces A: Physicochemical and Engineering Aspects* **225**, 1 (2003).
- [12] S. Kam and W. R. Rossen, *A Model for Foam Generation in Homogeneous Media*, *SPE Journal* **8**, 417 (2003).
- [13] L. Cheng, A. B. Reme, D. Shan, D. A. Coombe, and W. R. Rossen, *Simulating Foam Processes at High and Low Foam Qualities*, in *SPE* (Tulsa, Oklahoma, 2000) pp. 1–15.
- [14] W. R. Rossen, S. Zeilinger, J. Shi, and M. Lim, *Simplified Mechanistic Simulation of Foam Processes in Porous Media*, *SPE Journal* **4**, 279 (1999).
- [15] Computer Modeling Group, *STARS Reservoir Simulator (2014)*, (2014).
- [16] W. R. Rossen, *Numerical Challenges in Foam Simulation : A Review*, in *SPE Annual Technical Conference and Exhibition held in New Orleans*, October (SPE International, New Orleans, 2013).

- [17] J. R. Cannon, *The One-Dimensional Heat Equation - John Rozier Cannon - Google Books* (Cambridge University Press, 1984).
- [18] L. Tao, *A Method for Solving Moving Boundary Problems on JSTOR*, Siam Journal for Applied Mathematics **46**, 254 (1986).
- [19] V. R. Voller, *An overview of numerical methods for solving phase change problems*, in *Advances in Numerical Heat Transfer* (CRC Press, 1996) Chap. 9.
- [20] Z. Khatib, G. Hirasaki, and A. Falls, *Effects of Capillary Pressure on Coalescence and Phase Mobilities in Foams Flowing Through Porous Media*, *SPE Reservoir Engineering* **3**, 919 (1988).
- [21] R. Farajzadeh, M. Lotfollahi, A. Eftekhari, W. R. Rossen, and G. J. H. Hirasaki, *Effect of Permeability on Implicit-Texture Foam Model Parameters and the Limiting Capillary Pressure*, *Energy & Fuels* **29**, 3011 (2015).

2

DISCRETIZATION SCHEMES FOR THE SIMULATION OF FOAM ENHANCED OIL RECOVERY

Many enhanced oil recovery (EOR) processes can be described using partial differential equations with parameters that are strongly non-linear functions of one or more of the state variables. Typically, these non-linearities result in solution components changing several orders of magnitude over small spatial or temporal distances. The numerical simulation of such processes with the aid of finite volume or finite element techniques poses challenges. In particular, temporally oscillating state variable values are observed for realistic grid sizes when conventional discretization schemes are used. These oscillations, which do not represent a physical process but are discretization artifacts, hamper the use of the forward simulation model for optimization purposes. To analyze these problems, we study the dynamics of a simple foam model describing the interaction of water, gas and surfactants in a porous medium. It contains sharp gradients due to the formation of foam. The simplicity of the model allows us to gain a better understanding of the underlying processes and difficulties of the problem. The foam equations are discretized by a first-order finite volume method. Instead of using a finite volume method with a standard interpolation procedure, we opt for an integral average, which smoothes out the discontinuity caused by foam generation. We introduce this method by applying it to the heat equation with discontinuous thermal conductivity. A similar technique is then applied to the foam model, reducing the oscillations drastically, but not removing them.

Parts of this chapter were prepared for presentation at the 15th European Conference on the Mathematics of Oil Recovery held in Amsterdam, The Netherlands, 29 August - 1 September 2016 [1].

2.1. INTRODUCTION

The generation of foam can be described by a system of partial differential equations with strongly non-linear functions, which impose challenges for the numerical modeling. Former studies [2], [3] and [4] show the occurrence of temporally strongly oscillating solutions when using forward simulation models that are entirely due to discretization artifacts (Fig. 2.1).

To analyze these problems, we study the dynamics of a one-dimensional, two-phase incompressible foam model based on the Buckley-Leverett equation [5]. In this simplified model, we consider a one-dimensional horizontal reservoir with one injection and one production well. Gas is injected in the reservoir, which consists of a porous medium filled with a mixture of water and surfactants (to simplify the model, oil is assumed to be absent). As soon as the injected gas comes into contact with a sufficient amount of water and surfactant, a foam is generated. The foam will cause a rapid decrease of the gas mobility, because it captures the gas in bubbles that are separated by liquid films (lamellae) between the pore walls [6]. The water mobility is not influenced by foam in these models, and hence, the mobility ratio between gas and water is reduced. This will increase the time that the injected gas needs to reach the production well (breakthrough time).

The governing equations of the foam model are solved sequentially in time by the implicit pressure explicit saturation (IMPES) method [7]. In space, the saturation equation is solved by a second-order MUSCL scheme [8], and in time by the second-order semi-implicit trapezoidal method. The pressure equation is discretized in space by a first-order finite volume method, and the resulting linear system is solved by the Cholesky method [9]. Instead of using a standard interpolation procedure for the phase mobilities when discretizing the pressure equation, we opt for an integral average. The highly non-linear transition caused by the generation of foam is hence integrated over a range of saturation values between two neighboring grid blocks, reducing jumps in the solution.

We first introduce this method by applying it to the heat equation with discontinuous thermal conductivity. The initially strongly oscillating solution becomes monotonic by introducing this small change in the discretization scheme. A similar technique is then applied to the foam model, reducing the oscillations drastically, but not removing them entirely. We analyze this difference in behavior by performing a continuity analysis of the numerical scheme for each model. Furthermore, we illustrate the effectiveness of our numerical scheme by comparing it with other finite volume schemes, which vary in order, interpolation procedure and the amount of artificial diffusion.

2.2. MATHEMATICAL MODEL

2.2.1. CONSERVATION LAW

We study the one-dimensional foam model defined in Van der Meer *et al.* [9]. In case of an incompressible fluid in a porous medium, mass conservation of the phase saturation $S_\alpha \in [0, 1]$ is given by

$$\phi \partial_t S_\alpha = -\partial_x (f_\alpha \mathbf{u}), \quad \forall x \in [0, 1], t \geq 0, \quad (2.1)$$

where the subscript $\alpha \in \{w, g\}$ denotes the water or gas phase, ϕ is the reservoir porosity, $f_\alpha = \lambda_\alpha / \lambda$ is the phase fractional flow function, and \mathbf{u} is the total Darcy velocity, which

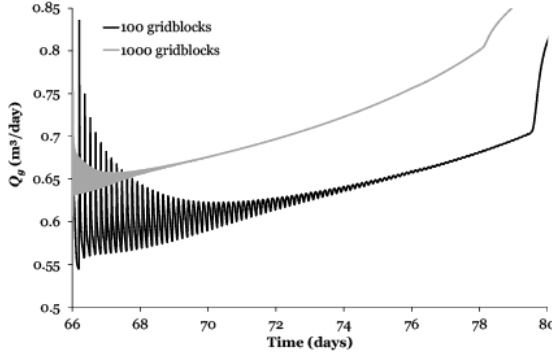


Figure 2.1: Temporal oscillations in the injection rate due to generation of foam, that are highly dependent on the grid resolution (from [2]).

follows from Darcy's law

$$u = -\lambda \partial_x p. \quad (2.2)$$

Here, p is the reservoir pressure, and λ is the total mobility, which is given by the sum of the phase mobilities as

$$\lambda_\alpha = k \frac{k_{r\alpha}(S_\alpha)}{\mu_\alpha}, \quad (2.3)$$

where k is the absolute permeability, μ_α the phase viscosity and $k_{r\alpha}$ the phase relative permeability, defined by the Brooks-Corey model [10]. The Brooks-Corey relative permeability functions for gas and water are given by

$$k_{rw} = k_{rwe} \left(\frac{S_w - S_{wc}}{1 - S_{wc} - S_{gr}} \right)^{n_w}, \quad k_{rg} = k_{rge} \left(\frac{S_g - S_{gr}}{1 - S_{wc} - S_{gr}} \right)^{n_g}, \quad (2.4)$$

where k_{rwe} and k_{rge} are the endpoint relative permeabilities, S_{wc} is the residual (con-note) water saturation, S_{gr} is the residual gas saturation and n_w and n_g are power coefficients, which all depend on the specific interface properties of the rock and the fluids. From the definition of saturation it follows that the sum of the phase saturations is one everywhere, i.e.

$$\sum_\alpha S_\alpha = 1, \quad \text{with } \alpha \in \{w, g\}, \quad (2.5)$$

so that we only have to solve for one phase. Hence, Eq. 2.1, 2.2 and 2.5 imply that

$$\partial_x u = \partial_x (-\lambda \partial_x p) = 0, \quad \Rightarrow u(x, t) = \bar{u}(t), \quad (2.6)$$

which describes the pressure decay in the porous medium.

2.2.2. FOAM MODEL

If gas comes into contact with a sufficient amount of water and surfactants a foam will form. This will cause a rapid decrease in the gas mobility λ_g , which can be modeled by

decreasing the relative gas permeability function by a mobility reduction factor f_{mr}

$$k_{rg} := \frac{k_{rg}^o}{f_{mr}}, \quad f_{mr} = 1 + R \cdot F_w \cdot F_s, \quad (2.7)$$

where k_{rg}^o is the relative permeability of the gas in its original state using the Brooks-Corey model, R is a constant that accounts for the maximum flow resistance of the foam, and F_w and F_s are functions that describe the sensitivity of the foam to water saturation and surfactant concentration, respectively [11]. We assume that the surfactant concentration is the same everywhere, so that $F_s = 1$. Because foam forms almost instantly, F_w is modeled by the Heaviside step function

$$F_w = H(S_w - S_w^*), \quad (2.8)$$

where S_w^* is the least amount of water that is needed to form a foam. Since a sudden jump in the mobility of the gas at S_w^* will lead to discontinuous derivatives in the simulator, this jump is approximated by a continuous arctangent function, so that it is smeared over a width that scales with $1/\kappa$

$$F_w = 0.5 + \frac{\arctan(\kappa(S_w - S_w^*))}{\pi}, \quad (2.9)$$

where κ is a positive parameter that controls the width of the gas-foam transition. (Eq. 2.7 and Eq. 2.9, with different symbols, are taken from the foam model in the STARS simulator [12].) In Fig. 2.2 the relative permeability function described here is shown. The flux function and its derivative for the scaled parameters are shown in Fig. 2.3.

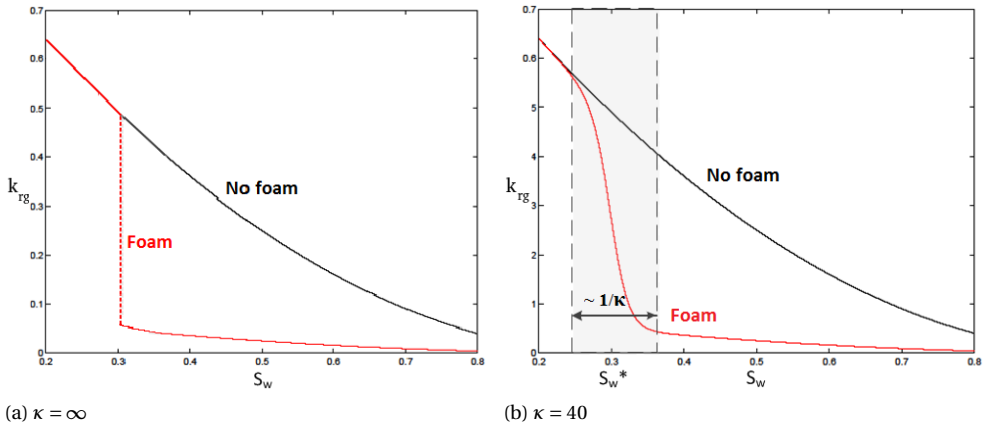


Figure 2.2: Relative permeability function for the model with and without foam. The sudden transition due to foam in the left figure given by Eq. 2.7 and 2.8 is approximated in the right figure by a continuous line given by Eq. 2.7 and 2.9, where $S_w^* = 0.3$, $\kappa = 40$, $R = 10$ and $M = 1$.

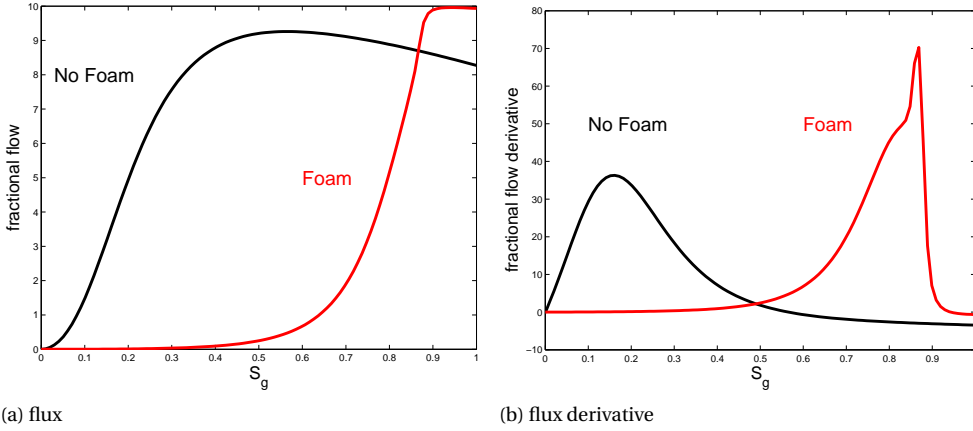


Figure 2.3: Flux function and derivative for the STARS model with and without foam, where $S_w^* = 0.15$, $\kappa = 1000$, $R = 1000$ and $M = 10$.

2.2.3. NON-DIMENSIONAL FORMULATION

To reduce the number of parameters we scale the model given by Eq. 2.1, 2.2 and 2.6, in a similar way as done by Riaz and Tchelepi [13]. If we let L be a characteristic length scale of the model, and U a characteristic velocity scale we can scale the variables as follows

$$x = Lx^*, \quad (2.10)$$

$$\partial_x = \frac{\partial_{x^*}}{L}, \quad (2.11)$$

$$u = Uu^*, \quad (2.12)$$

$$t = \frac{\phi L(1 - S_{wc} - S_{gr})}{U} t^*, \quad (2.13)$$

$$p = \frac{\mu UL}{k} p^*, \quad (2.14)$$

where the asterisk denotes a non-dimensional variable. The relative permeability functions are scaled by their endpoint relative permeabilities, i.e. the relative permeability of the residual water and gas saturation, $k_{rwe} = k_{rw}(S_{gr})$ and $k_{rge} = k_{rg}(1 - S_{wc})$, respectively. The gas saturation is normalized by $S_g^* = \frac{(S_g - S_{gr})}{(1 - S_{wc} - S_{gr})}$. Substituting these variables into the dimensional model leads to a non-dimensional system of the form

$$\partial_{t^*} S_g^* = -\partial_{x^*} \left(\frac{k_{rg}^* M}{\lambda^*} u^* \right), \quad (2.15)$$

$$u^* = -\lambda^* \partial_{x^*} p^*, \quad (2.16)$$

$$\partial_{x^*} u^* = 0, \quad (2.17)$$

where $\lambda^* = Mk_{rg}^* + k_{rw}^*$ is the dimensionless mobility function. Here, the variable M denotes the dimensionless mobility ratio, given by

$$M = \frac{\mu_w}{\mu_g} \frac{k_{rge}}{k_{rwe}}. \quad (2.18)$$

The mobility ratio together with the dimensionless foam parameters R , κ and S_w^* , dimensionless injection rate I^* and porosity ϕ , determine the entire behavior of the fluids for a certain initial boundary value problem. In the rest of the article we will drop the asterisk for readability and define $S \equiv S_g$ and $f \equiv \frac{k_{rg}M}{\lambda}$.

Together with initial and boundary conditions, we then have the following initial boundary-value problem

$$\partial_t S = -\partial_x(fu), \quad \forall x \in [0, 1], t \geq 0, \quad (2.19)$$

$$\partial_x u = 0, \quad \forall x \in [0, 1], \quad (2.20)$$

$$u = -\lambda \partial_x p, \quad \forall x \in [0, 1], \quad (2.21)$$

$$S(x, 0) = 0, \quad \forall x \in [0, 1], \quad (2.22)$$

$$S(0, t) = 1, \quad \forall t \geq 0, \quad (2.23)$$

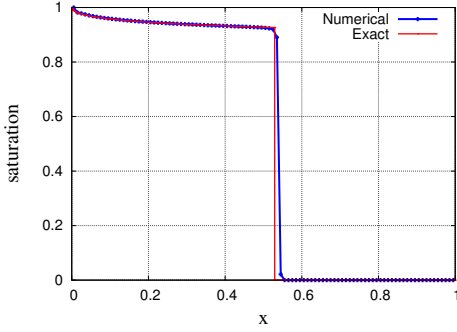
$$u(0, t) = u_L, \quad \forall t \geq 0, \quad (2.24)$$

$$p(1, t) = p_R, \quad \forall t \geq 0, \quad (2.25)$$

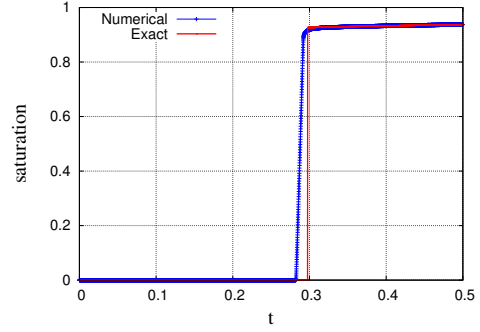
where we fix the velocity on the left boundary and the pressure on the right boundary. Due to the incompressibility condition, the velocity will now be constant in time and space. Hence, the solution of Eq. 2.19 is independent of Eq. 2.20 and the system is only weakly coupled through the total mobility. Later in this chapter, we will also investigate the strongly coupled system, where the pressure is fixed on both sides of the domain (i.e. Eq. 2.24 is replaced by $p(0, t) = p_L$).

2.3. NUMERICAL OSCILLATIONS

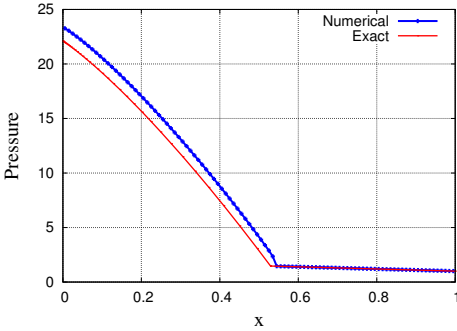
We solve the foam model numerically for multiple sets of foam parameters, where we use the IMPES method with a second-order MUSCL solver for the explicit part. A necessary condition for stability of the saturation update, is given by the Courant-Friedrichs-Lewy (CFL) condition. Due to the high wave speeds around the critical water saturation, as shown in Fig. 2.3b, the time step can become extremely restricted if κ is increased. In Fig. 2.4, the saturation profile of the foam model for one parameter set is shown, which is stable in both space and time. However, if we take a look at the pressure solutions in Fig. 2.4, we see that the pressure solution is oscillating in time. In Fig. 2.5, we show that the amplitude of the oscillations is highly dependent on the value of the foam parameters R and κ . Both increasing the foam resistance R and the steepness of the foam transition κ will cause stronger oscillatory behavior. Both the amplitude and frequency of the oscillations seem directly related to the grid size. Decreasing the grid size will decrease the amplitude of the oscillations and increase its frequency, as depicted in Fig. 2.1. Moreover, we can connect each oscillation to a grid block the shock has passed, as shown in Fig. 2.6, which was also observed in Zanganeh *et al.* [2]. So, unless the step size is drastically reduced, the oscillations will not disappear by using a higher resolution in space



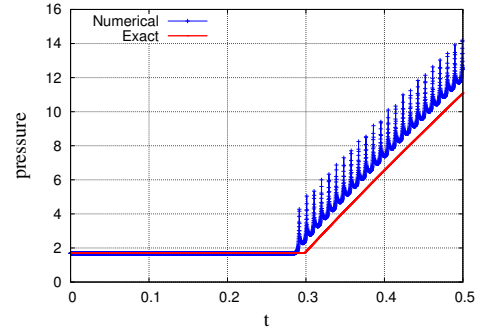
(a) $t = 0.5$



(b) $x = 0.3$



(c) $t = 0.5$



(d) $x = 0.3$

Figure 2.4: Numerical and analytical saturation and pressure profiles of the foam model with resolution $N = 100$ and $M = 1$, $S_{w}^* = 0.15$, $\kappa = 1000$ and $R = 10000$, $u_L = 1, \rho_R = 1$.

(Fig. 2.7). Considering the already small time step size due to the CFL condition, it is not feasible to further reduce the step size significantly.

2.4. HEAT EQUATION WITH A DISCONTINUOUS CONDUCTIVITY

Similar oscillations in time were observed for the one-dimensional heat equation with a discontinuous coefficient, defined by

$$\partial_t T = -\partial_x q, \quad \forall x \in [0, 1], t \geq 0, \quad (2.26)$$

$$q = -a(T)\partial_x T, \quad (2.27)$$

$$T(x, 0) = 0, \quad \forall x \in [0, 1], \quad (2.28)$$

$$T(0, t) = 1, \quad \forall t \geq 0, \quad (2.29)$$

$$T(1, t) = 0, \quad \forall t \geq 0, \quad (2.30)$$

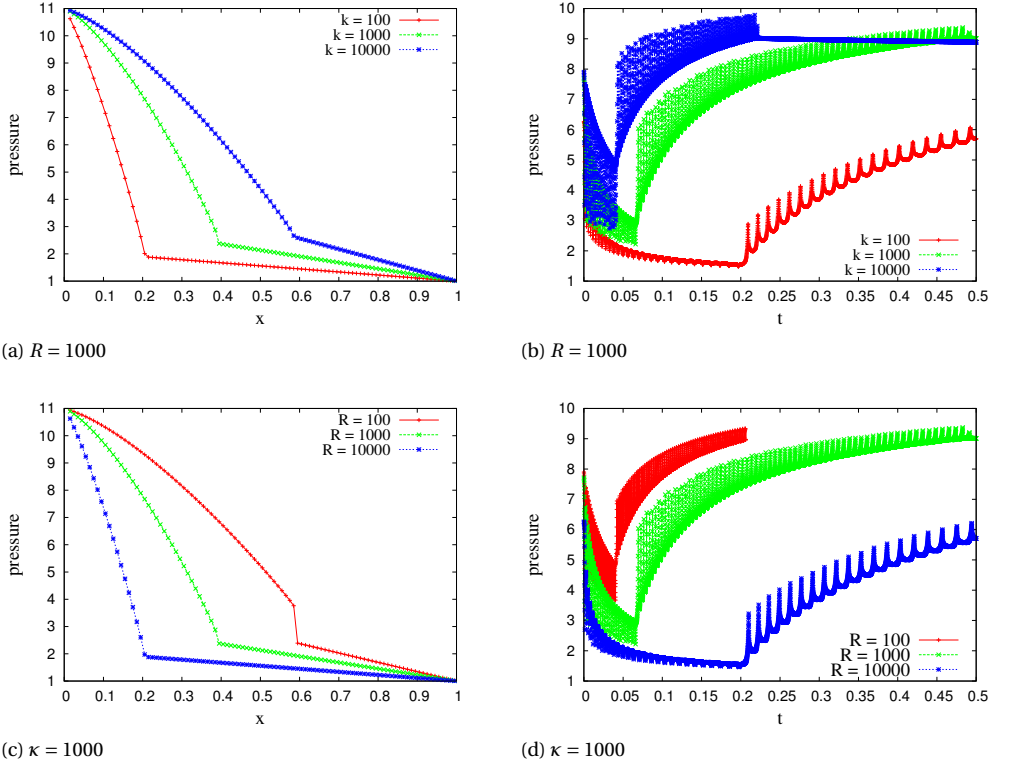


Figure 2.5: (Left) pressure versus spatial coordinate at $t = 0.1$, (Right) pressure versus time at $x = 0.5$, of the foam model with resolution $N = 100$ and $M = 1$, $S_w^* = 0.2$, $p_L = 11$, $p_R = 1$.

where T is the temperature and a the thermal conductivity given by a step function

$$a(T) := \begin{cases} e & \text{if } T \leq T^*, \\ 1 & \text{if } T > T^*, \end{cases} \quad (2.31)$$

as depicted in Fig. 2.8. We semi-discretize this equation with the finite volume method over a finite interval $[0, 1]$ that is divided into N grid cells with size $\Delta x = 1/N$ as shown in Fig. 2.9, where $x_i = i\Delta x$ denotes the midpoint of the i -th grid cell and $T_i = T(x_i)$ the average temperature in the i -th grid cell. The cell centers are indexed by $i \in \{0, \dots, N\}$ and the cell interfaces by $i \in \{-\frac{1}{2}, \frac{1}{2}, \dots, N + \frac{1}{2}\}$. Hence, we obtain a system of ordinary

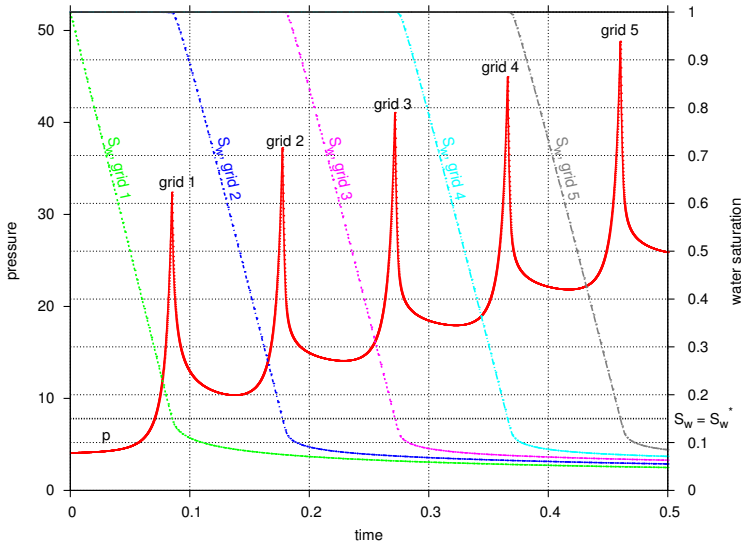


Figure 2.6: Pressure versus time for $x = 0.15$, compared to the saturation versus time at $x = 0.15$, $x = 0.25$, $x = 0.35$, $x = 0.45$ and $x = 0.55$, for $N = 10$, $M = 1$, $S_w^* = 0.2$, with $u_L = 10$ described on the left boundary and $p_R = 1$ prescribed on the right boundary

differential equations for the unknowns

$$\dot{T}_i = \frac{q_{i-\frac{1}{2}} - q_{i+\frac{1}{2}}}{\Delta x}, \quad \forall i \in \{0, \dots, N\}, \quad (2.32)$$

$$q_{i+\frac{1}{2}} = -a_{i+\frac{1}{2}} \frac{T_{i+1} - T_i}{\Delta x}, \quad \forall i \in \{0, \dots, N-1\}, \quad (2.33)$$

$$q_{-\frac{1}{2}} = -a(T_0) \frac{T_0 - T_L}{\Delta x/2}, \quad (2.34)$$

$$q_{N+\frac{1}{2}} = -a(T_N) \frac{T_R - T_N}{\Delta x/2}, \quad (2.35)$$

where \dot{T}_i is the time derivative of T_i , and $a_{i+\frac{1}{2}}$ is the approximation of the thermal conductivity on the cell interface, which can be computed by one of the following approaches

- upwind: $a_{i+\frac{1}{2}} = \begin{cases} a(T_i), & \text{if } T_i \geq T_{i+1}, \\ a(T_{i+1}), & \text{if } T_i < T_{i+1}, \end{cases}$
- harmonic average: $a_{i+\frac{1}{2}} = \frac{2a(T_i)a(T_{i+1})}{a(T_i)+a(T_{i+1})}$,
- arithmetic average: $a_{i+\frac{1}{2}} = \frac{1}{2}(a(T_i) + a(T_{i+1}))$,

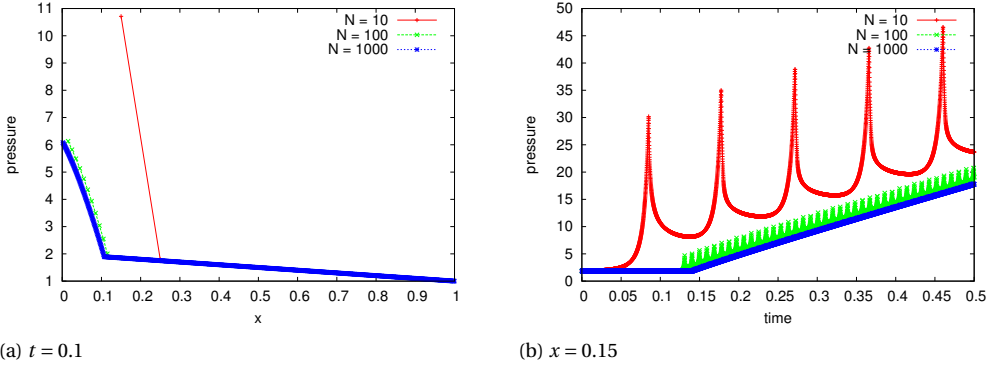


Figure 2.7: Non-oscillatory solutions in space (left) and oscillatory solutions in time (right) for different grid resolutions and $M = 1$, $S_{iw}^* = 0.15$, $\kappa = 1000$ and $R = 10000$, $u_L = 1, p_R = 1$.

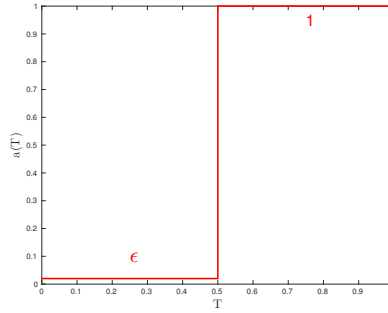


Figure 2.8: Discontinuous thermal conductivity $a(T)$ for $T^* = 0.5$ and $\epsilon = 0.01$.

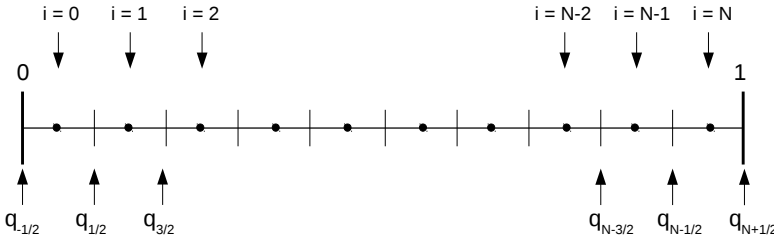
- maximum average: $a_{i+\frac{1}{2}} = \max\{a(T_i), a(T_{i+1})\}$.

Because the temperature decreases from left to right, the maximum average is identical to the upwind average for this problem, and the harmonic average is unsuitable since it converges very slowly if ϵ is small. Eq. 2.32 is then solved by the forward Euler method for the other two averaging procedures and a constant time step $\Delta t = 1.8 \cdot 10^{-4}$, which satisfies the CFL condition.

2.4.1. TEMPORAL OSCILLATIONS

Independent of the choice of the flux discretization, this will lead to an oscillatory behavior in time, as shown in Fig. 2.10b and 2.10d. As a remedy, we take the integral over the discontinuous parameter a defined by

$$A(T) \equiv \int_0^T a(v) dv, \quad (2.36)$$

Figure 2.9: Numerical grid over the domain $[0, 1]$.

so that the solution of the heat equation satisfies

$$q = -a(T)\partial_x T = -\frac{\partial A}{\partial x}. \quad (2.37)$$

This suggests the following choice for the numerical flux

$$q_{i+\frac{1}{2}} = \frac{A(T_i) - A(T_{i+1})}{\Delta x} = -\frac{1}{\Delta x} \int_{T_i}^{T_{i+1}} a(v) dv, \quad (2.38)$$

which corresponds to the choice

$$a_{i+\frac{1}{2}} = \frac{A(T_{i+1}) - A(T_i)}{T_{i+1} - T_i} = \frac{1}{T_{i+1} - T_i} \int_{T_i}^{T_{i+1}} a(v) dv. \quad (2.39)$$

If this integral is approximated using the Trapezoidal rule, it will reduce to the arithmetic average discretization, leading to non-physical oscillations. However, if we evaluate the integral exactly, $A(T)$ becomes a C^0 -continuous function of the temperature. Hence the flux q will be a continuous function of the temperature. From Eq. (2.32) it then follows that \hat{T} is a C^0 -continuous function and so the solution for T is C^1 -continuous [14]. In Fig. 2.10f the solution in time using the integral average (2.39) is depicted. The resulting temperature is monotone in time, but exhibits a stepwise increase that will damp out after some time. Also note that the integral average approaches the exact solution most closely among the three methods. Of all cases the upwind average performs worst.

To determine the nature of the oscillations we analyze the (almost) semi-discrete behavior of the equation by taking a very small time step. The results are shown in Fig. 2.11 and 2.12. The integral average method does not show any improvement by decreasing the time step, since the stepwise behavior is still visible. The smoothness of the solution using the other two averaging methods improves significantly by taking a smaller time step, since the amplitude of the oscillations is smaller and the oscillations are mainly restricted to a small time interval occurring after the shock wave has passed. Behind the shock front, the solutions show some low-frequency oscillations, with a decreasing amplitude that resemble the stepwise pattern we observed for the integral average method. The integral average is thus able to remove the high-frequency oscillations, but not enough to get rid of the low-frequency oscillations.

Let us examine the time interval where the high frequency oscillations occur for the first two averaging methods. The length of this interval seems to be dependent on the grid

resolution and it reduces if the grid is refined. As the time step is reduced, the oscillations decrease in amplitude, and finally a constant state is reached, which approaches the temperature at which the heat conductivity is discontinuous. The length of this time interval corresponds to the time that the numerical shock precedes the analytical shock. If the integral average is applied, no such constant state is obtained and the numerical shock fits the analytical shock quite well.

2

2.5. FOAM MODEL WITH A DISCONTINUOUS MOBILITY

If we consider the foam model given by Eq. 2.19 to 2.24, we observe many similarities with the heat equation with discontinuous conductivity. The system contains a discontinuous parameter λ , shown in Fig. 2.13. Like the thermal conductivity a , this parameter λ is responsible for the time oscillations that were observed in the pressure solution.

2.5.1. FINITE VOLUME SCHEME USING AN INTEGRAL AVERAGE

If we discretize the system of equations with the finite volume method we obtain the following semi-discrete system in x_i

$$\dot{S}_i = -\bar{u} \frac{f_{i+\frac{1}{2}} - f_{i-\frac{1}{2}}}{\Delta x}, \quad \text{for } i \in \{0, \dots, N\}, \quad (2.40)$$

$$\partial_x \bar{u}_i = \frac{\bar{u}_{i+\frac{1}{2}} - \bar{u}_{i-\frac{1}{2}}}{\Delta x} = 0, \quad \text{for } i \in \{0, \dots, N\}, \quad (2.41)$$

$$\bar{u}_{i+\frac{1}{2}} = -\lambda_{i+\frac{1}{2}} \frac{p_{i+1} - p_i}{\Delta x}, \quad \text{for } i \in \{0, \dots, N-1\}, \quad (2.42)$$

$$\bar{u}_{-\frac{1}{2}} = -\lambda(S_0) \frac{p_0 - p_L}{\Delta x/2}, \quad (2.43)$$

$$\bar{u}_{N+\frac{1}{2}} = -\lambda(S_N) \frac{p_R - p_N}{\Delta x/2}, \quad (2.44)$$

where $\lambda_{i+\frac{1}{2}}$ is approximated on the cell interface by one of the following interpolation methods

- upwind: $\lambda_{i+\frac{1}{2}} = \begin{cases} \lambda(S_i), & \text{if } u_i > 0, \\ \lambda(S_{i+1}), & \text{if } u_i < 0, \end{cases}$
- harmonic average: $\lambda_{i+\frac{1}{2}} = \frac{2\lambda(S_i)\lambda(S_{i+1})}{\lambda(S_i)+\lambda(S_{i+1})}$,
- arithmetic average: $\lambda_{i+\frac{1}{2}} = \frac{1}{2}(\lambda(S_i) + \lambda(S_{i+1}))$,
- maximum: $\lambda_{i+\frac{1}{2}} = \max(\lambda(S_i), \lambda(S_{i+1}))$.

It was shown earlier that this approach leads to non-physical oscillations in time. The amplitude of these oscillations depends, besides the foam parameters and the grid size, on the adopted interpolation method. The upwind average will cause similar oscillations as the harmonic average applied to the finite volume discretization of the foam model. The mean average method suffers much less from oscillations than the harmonic average method. It is reasonable to assume that if we choose this average in a smarter way, it will be possible to reduce the oscillations even further.

Starting from Eq. 2.2 and 2.6 with $\bar{u}(t) = 1$, it follows that

$$p(x, t) = \int_x^1 \frac{dx}{\lambda(S(x, t))} + p_R, \quad (2.45)$$

A central two-point discretization for the spatial derivative leads to the semi-discrete equation for the pressure as a function of time only

$$p_i(t) = \Delta x \sum_{j=i}^N \frac{1}{\lambda(S_j(t), S_{j+1}(t))} + p_R. \quad (2.46)$$

Hence, p is a smooth function of time if $\frac{1}{\lambda(S_i, S_{i+1})}$ and $\bar{u}(t)$ are smooth. If we fix the velocity at the left boundary, it will be constant in time and space, due to the incompressibility condition. This means we only have to obtain a smooth formulation for the sum over the mobilities in time. In order to achieve this we take the cell-integral average of $\frac{1}{\lambda}$ over the interval $[S_i, S_{i+1}]$, given by

$$\frac{1}{\lambda(S_j, S_{j+1})} = \frac{1}{S_{i+1} - S_i} \int_{S_i}^{S_{i+1}} \frac{1}{\lambda(S)} dS, \quad (2.47)$$

so that

$$\lambda_{i+\frac{1}{2}} = \frac{S_{i+1} - S_i}{\int_{S_i}^{S_{i+1}} \frac{1}{\lambda(S)} dS}. \quad (2.48)$$

Alternatively, we can take the integral over λ directly, so that

$$\lambda_{i+\frac{1}{2}} = \frac{1}{S_{i+1} - S_i} \int_{S_i}^{S_{i+1}} \lambda(S) dS. \quad (2.49)$$

If λ is a smooth function of S and $\Delta S_i = |S_{i+1} - S_i|$ is small, the integral averages are similar to standard averages like the arithmetic average. It can be shown that in this case

$$\frac{1}{S_{i+1} - S_i} \int_{S_i}^{S_{i+1}} \lambda(S) dS = \frac{\lambda(S_i) + \lambda(S_{i+1})}{2} + \mathcal{O}((\Delta S_i)^2). \quad (2.50)$$

Finally, to avoid very large contributions to the sum of inverse mobilities $\frac{1}{\lambda(S_i, S_{i+1})}$, we could opt for another 'averaging method', given by

$$\lambda_{i+\frac{1}{2}} = \max\{\lambda(S_i), \lambda(S_{i+1})\}. \quad (2.51)$$

We solve the system given by Eq. 2.19 to 2.20 with the IMPES method, where we make use of different averaging methods for the total mobility. The resulting pressure solutions in time are shown in Fig. 2.14 for a grid resolution $N = 100$.

From these results it is clear that the integral average is not sufficient to remove the oscillations, although the amplitude is halved compared to the upwind and harmonic average. However, if we use a coarser grid with resolution $N = 10$, the oscillations are more pronounced, and it becomes apparent that the integral average has a smoothing effect on the oscillations (Fig. 2.15). There are several things worth noting in Fig. 2.15. First, the number of oscillations is the same for all averaging methods and matches the number of grid blocks behind the saturation front. Furthermore, note that the amplitude of the oscillations differs drastically, with approximately a factor five between the upwind average and the maximum average (Fig. 2.16). Besides that, the nature of the discontinuity varies for the different averaging methods. It can be seen that for the maximum mobility the oscillations are saw teeth, also called removable discontinuities, since the limit on both sides is equal. These discontinuities are not continuously differentiable and hence are C^0 -continuous functions. The integral average, on the contrary, is continuously differentiable.

2.6. DISCUSSION AND CONCLUSION

We studied two types of temporal oscillations, that are entirely due to the grid discretization. The first type of oscillations appear in the parabolic heat equation with discontinuous conductivity, when discretized with the finite volume method. The second type of oscillations are found in the elliptic part of a two-phase, incompressible foam model, with (almost) discontinuous mobility.

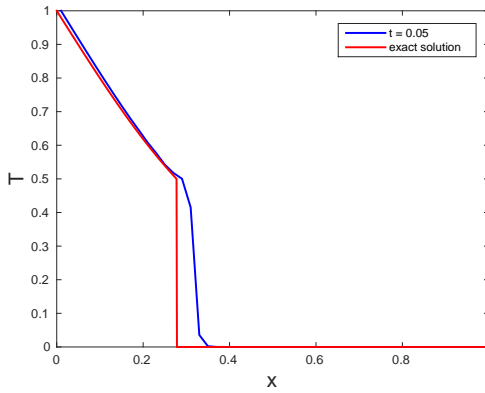
To get rid of these non-physical oscillations we changed the averaging method on the grid interfaces of the finite volume scheme. Instead of taking an average of the conductivity/mobility on each side of the grid interface, all (unknown) values in-between are taken into account, by integrating the conductivity/mobility over the given temperature/saturation range. This can be seen as a sort of flux correction method, where linear interpolation is used to approximate the in-between values.

Applying the integral average to the non-linear heat equation with discontinuous heat conductivity removes the oscillations for our test cases. Applying the same scheme to the foam model, does not solve the numerical problems. However, integration over the mobility does change the nature of the discontinuities. The pressure solution becomes continuously differentiable in time, and the amplitude of the oscillations is reduced by a significant amount. Still, the maximum average performs best, when we compare the different averaging schemes for all test cases.

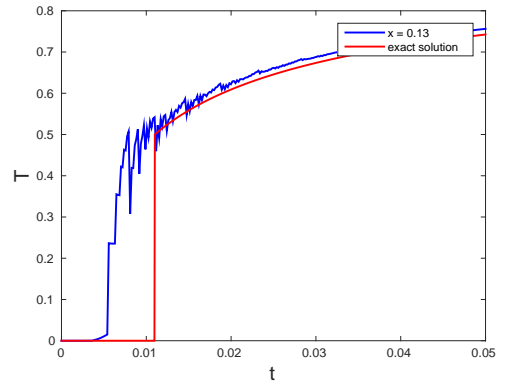
REFERENCES

- [1] J. M. Van der Meer, J. B. F. M. Kraaijevanger, M. Möller, and J. D. Jansen, *Temporal oscillations in the simulation of foam enhanced oil recovery*, in *Proc. 15th European Conference on Mathematics in Oil Recovery (ECMOR XIV)* (Amsterdam, 2016).

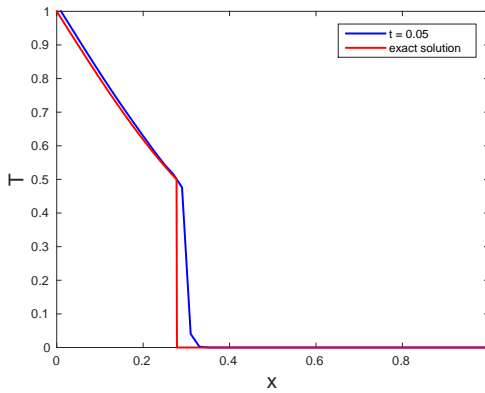
- [2] M. N. Zanganeh, J. F. B. M. F. M. Kraaijevanger, H. W. Buurman, J. D. Jansen, W. R. Rossen, M. Namdar Zanganeh, J. F. B. M. F. M. Kraaijevanger, H. W. Buurman, J. D. Jansen, W. R. Rossen, and M. N. Zanganeh, *Challenges in adjoint-based optimization of a foam EOR process*, *Computational Geosciences* **18**, 563 (2014).
- [3] E. Ashoori, D. Marchesin, and W. R. Rossen, *Roles of transient and local equilibrium foam behavior in porous media: Traveling wave*, *Colloids and Surfaces A: Physicochemical and Engineering Aspects* **377**, 228 (2011).
- [4] E. Ashoori, D. Marchesin, and W. R. Rossen, *Stability Analysis of Uniform Equilibrium Foam States for EOR Processes*, *Transport in Porous Media* **92**, 573 (2012).
- [5] S. E. Buckley and M. C. Leverett, *Mechanism of fluid displacements in sands*, *Transactions of the AIME* **146**, 107 (1942).
- [6] W. R. Rossen, *Numerical Challenges in Foam Simulation : A Review*, in *SPE Annual Technical Conference and Exhibition held in New Orleans*, October (SPE International, New Orleans, 2013).
- [7] K. Aziz and A. Settari, *Petroleum reservoir simulation* (Chapman & Hall, 1979).
- [8] B. van Leer, *Towards the Ultimate Conservative Difference Scheme. V. A Second-Order Sequel to Godunov's Method*, *Journal of Computational Physics* **32**, 101 (1979).
- [9] J. M. Van der Meer, D. E. A. Van Odyck, P. Wirnsberger, and J. D. Jansen, *High-order Simulation of Foam Enhanced Oil Recovery*, in *Proc. 14th European Conference on Mathematics in Oil Recovery (ECMOR XIV)* (Catania, 2014) pp. 8–11.
- [10] R. Brooks and T. Corey, *Hydraulic properties of porous media*, Tech. Rep. (Colorado State University, Fort Collins, Colorado, 1964).
- [11] C. S. Boeije and W. R. Rossen, *Fitting Foam Simulation Model Parameters for SAG Foam Applications*, in *SPE Enhanced Oil Recovery Conference* (Society of Petroleum Engineers, 2013).
- [12] Computer Modeling Group, *STARS Reservoir Simulator (2014)*, (2014).
- [13] A. Riaz and H. A. Tchelepi, *Stability of two-phase vertical flow in homogeneous porous media*, *Physics of Fluids* **19**, 072103 (2007).
- [14] E. A. Coddington and N. Levinson, *Theory of ordinary differential equations* (McGraw-Hill, 1955).



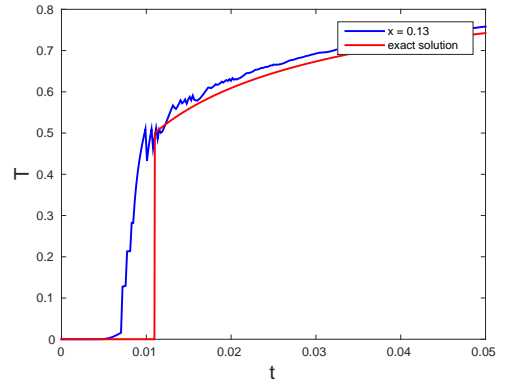
(a) Upwind average vs x



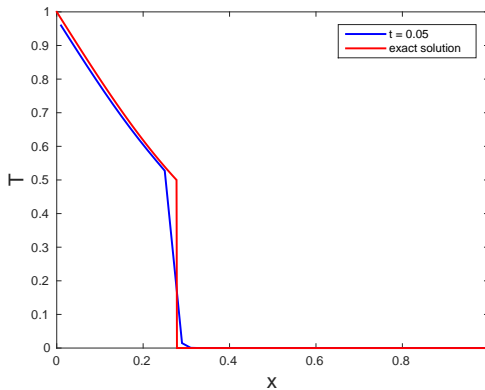
(b) Upwind average vs t



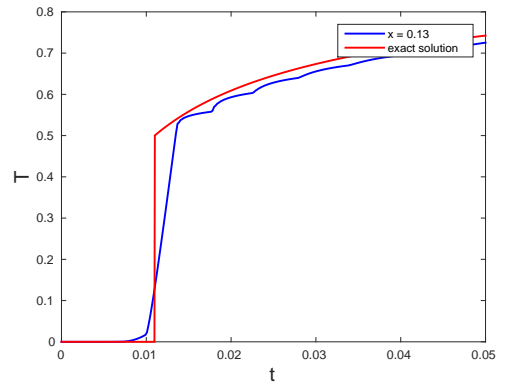
(c) Arithmetic average vs x



(d) Arithmetic average vs t

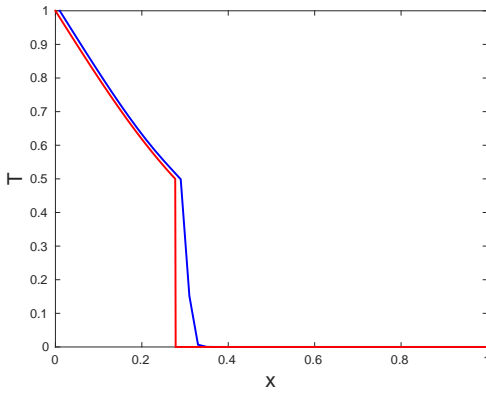


(e) Integral average vs x

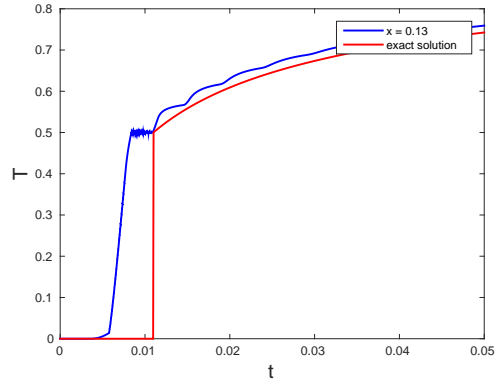


(f) Integral average vs t

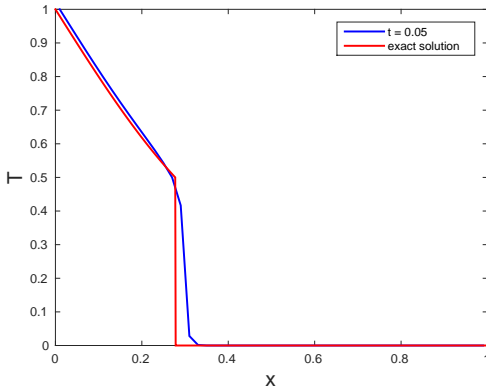
Figure 2.10: Numerical and analytical temperature profiles of the heat equation with discontinuous conductivity, where $\Delta x = 0.02$, $\Delta t = 1.8 \cdot 10^{-4}$, $T^* = 0.5$ and $\epsilon = 0.01$.



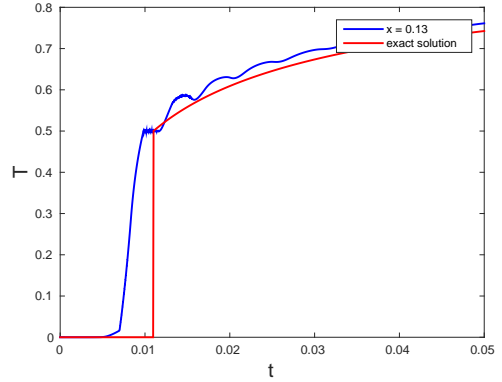
(a) Upwind average vs x



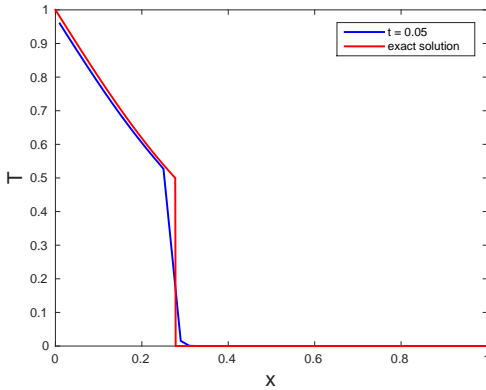
(b) Upwind average vs t



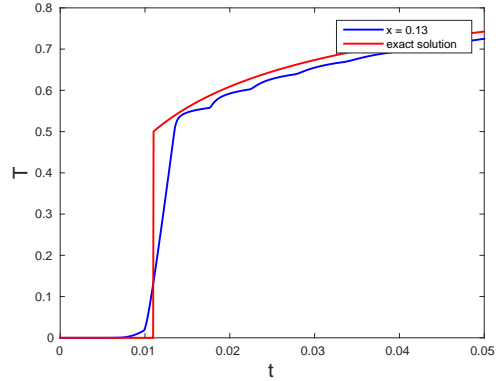
(c) Arithmetic average vs x



(d) Arithmetic average vs t

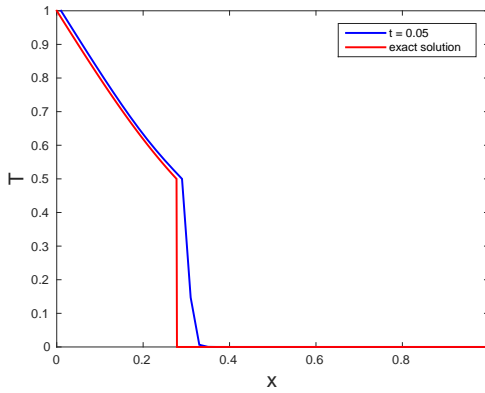


(e) Integral average vs x

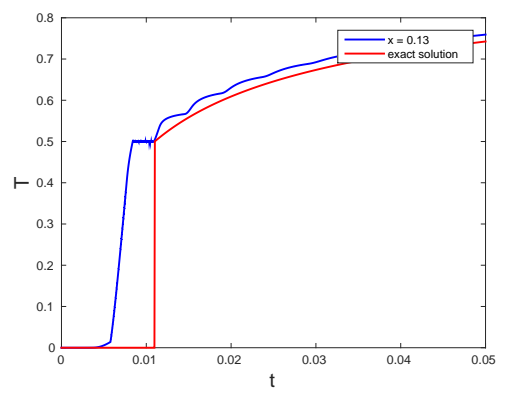


(f) Integral average vs t

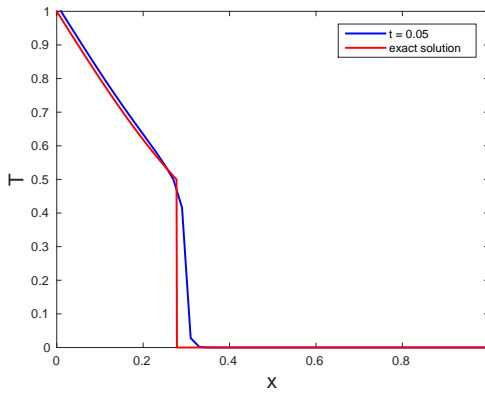
Figure 2.11: Numerical and analytical temperature profiles of the heat equation with discontinuous conductivity, where $\Delta x = 0.02$, $\Delta t = 1.8 \cdot 10^{-6}$, $T^* = 0.5$ and $\epsilon = 0.01$.



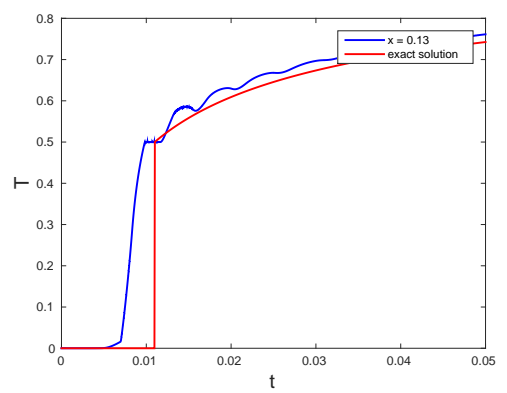
(a) Upwind average vs x



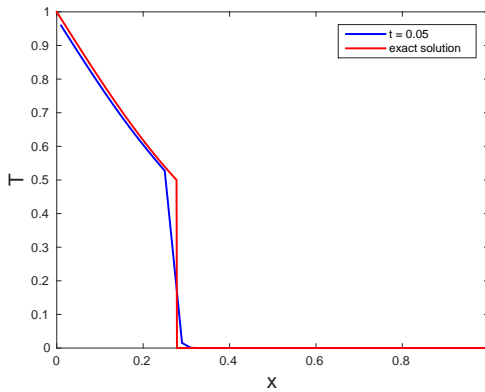
(b) Upwind average vs t



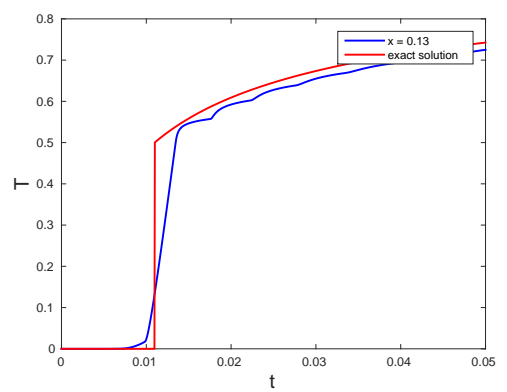
(c) Arithmetic average vs x



(d) Arithmetic average vs t



(e) Integral average vs x



(f) Integral average vs t

Figure 2.12: Numerical and analytical temperature profiles of the heat equation with discontinuous conductivity, where $\Delta x = 0.02$, $\Delta t = 1.8 \cdot 10^{-7}$, $T^* = 0.5$ and $\epsilon = 0.01$.

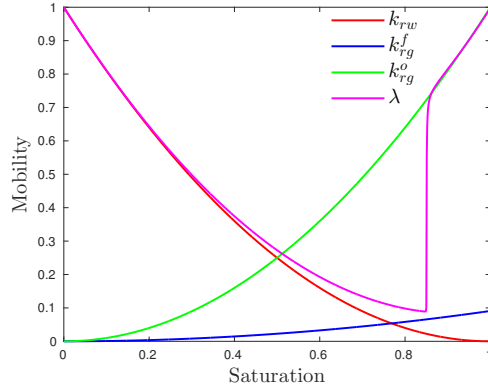
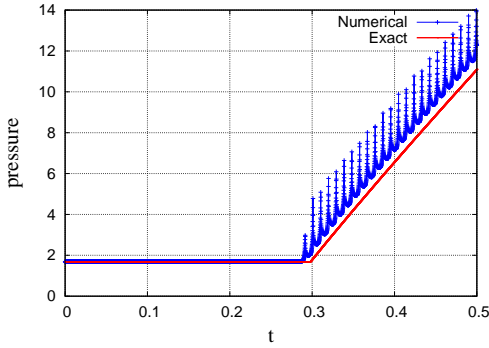
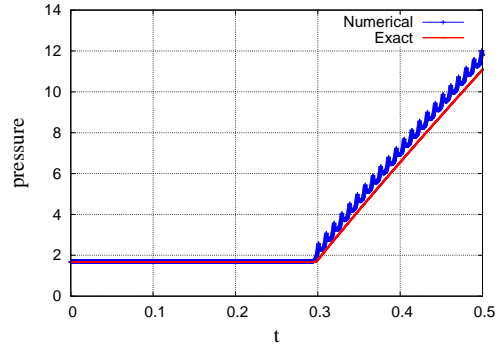


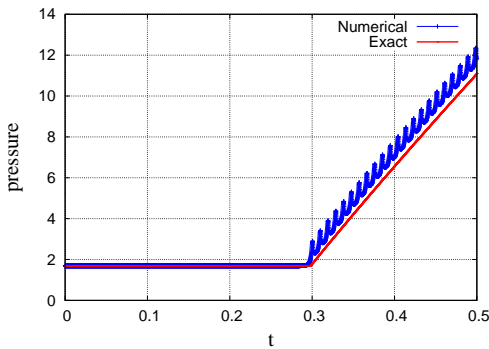
Figure 2.13: Relative permeability functions of water, gas and foam and the total mobility λ at a fixed time for $M = 1, S_w^* = 0.15$.



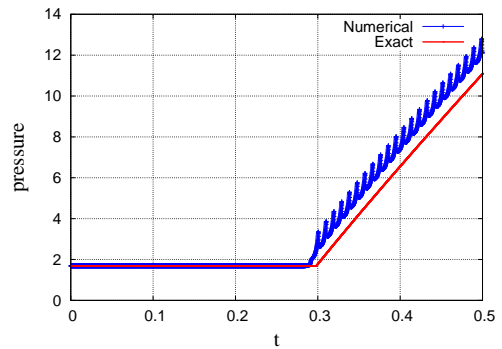
(a) Harmonic average



(b) Arithmetic average



(c) Integral average over λ



(d) Integral average over $\frac{1}{\lambda}$

Figure 2.14: Pressure vs time $x = 0.15$ for $N = 100, M = 1, S_w^* = 0.2$, with $u_L = 1$ described on the left boundary and $p_R = 1$ prescribed on the right boundary.

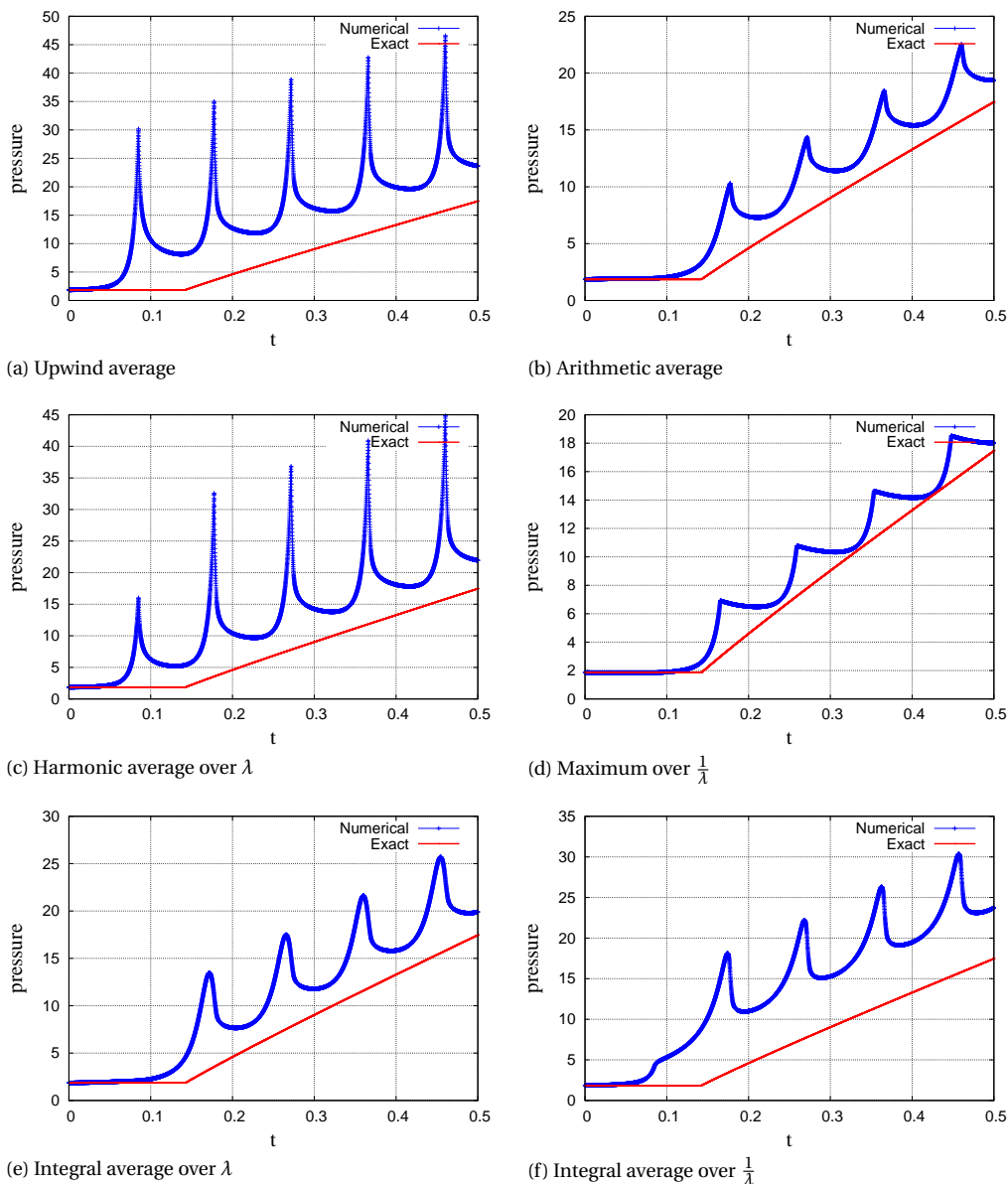


Figure 2.15: Pressure vs time at $x = 0.15$ for $N = 10$, $M = 1$, $S_w^* = 0.2$, with $u_L = 10$ described on the left boundary and $p_R = 1$ prescribed on the right boundary.

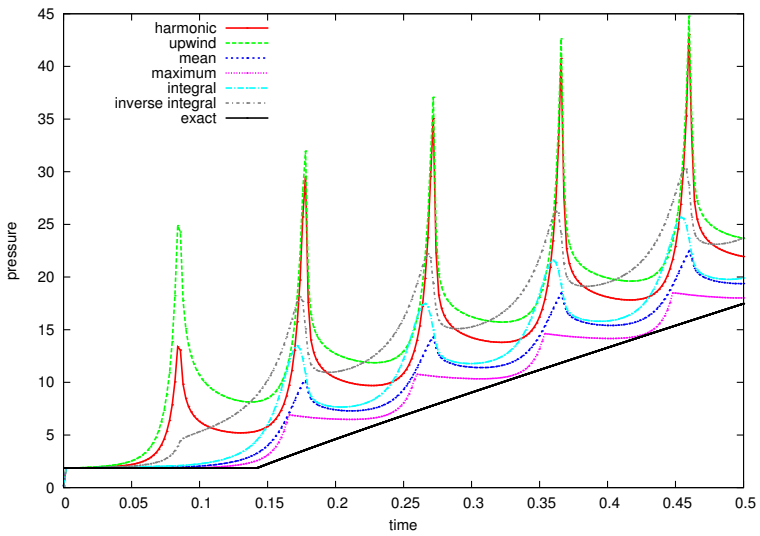


Figure 2.16: Pressure versus time for $N = 10$, $M = 1$, $S_w^* = 0.2$, with $u_L = 10$ prescribed on the left boundary and $p_R = 1$ prescribed on the right boundary.

3

MIMETIC DISCRETISATION SCHEMES FOR GENERIC PHASE CHANGE PROBLEMS

The essential numerical difficulty in dealing with phase change problems rests in the requirement to account for non-linear phenomena that change in time and space.

V.R. Voller, 1996

When dealing with parabolic equations with a continuous initial function and a continuous diffusion coefficient, existence and uniqueness of the solutions is ensured and stability of the numerical method is generally not considered an issue since diffusion will smooth out any perturbations. However, if we are considering the class of parabolic equations with discontinuous and/or strongly degenerate parameters this may not be true. Indeed, it was shown in [1] that for a convection-diffusion problem with a strongly degenerate diffusion function, the solutions admit discontinuities in the form of shock waves. Hence, an additional entropy condition is needed to ensure uniqueness of the solution. When solving these problems numerically, standard discretization schemes give rise to stability issues in time [2]. Therefore, we have to take into account the non-linearity in the coefficients of the system. It is possible to write the parabolic equation as a hyperbolic equation plus an ordinary differential equation. The stability of numerical schemes for hyperbolic equations has been widely addressed. Total variation diminishing and oscillation diminishing methods are two important classes of solvers that control the stability of the solutions of conservation laws. Since we are not dealing with strictly hyperbolic conservation laws, developing a similar method for parabolic equations, is not straightforward. For this we have to consider both stability in space and in time in a finite volume framework. In this

chapter we provide a short overview of numerical schemes suitable for parabolic equations with discontinuous variables. We propose some ideas to improve existing schemes, like the addition of an extra node at the discontinuous interface. There are, however, several ways to incorporate this node in the scheme, which can involve interpolation of the solution between adjacent grid points or redefining the problem in terms of internal energy (enthalpy). In this chapter, we compare some of these methods, and discuss the advantages and limitations.

3.1. INTRODUCTION

Many numerical methods have been proposed to treat hyperbolic and parabolic equations with discontinuous parameters that vary only in space, but are time-independent (among many others [3–11]). When discontinuities are space- and time-dependent [2, 12, 13], other difficulties arise. We illustrate this by looking at the heat equation with a piecewise continuous thermal diffusivity, which contains a discontinuity at a critical temperature. This situation occurs for example when a block of ice is heated from one side, and melts into water when the temperature passes zero degree Celsius. The discontinuity in the diffusivity represents the phase interface. In case of a piecewise constant thermal diffusivity we can derive an analytical solution, that consist of two separate solutions that are connected through a moving interface by means of three interface conditions. This is also called a Stefan problem in literature [14–16] and the main interface condition a Stefan condition.

When solved on a numerical grid with standard finite volume methods, the numerical solution of these problems on a coarser grid has stability issues due to the discontinuous derivatives at the phase interface. The solutions remain smooth in space, when the Courant-Friedrichs-Levy (CFL) stability criterion on the time step is met. However, strong oscillations in time appear, whenever the discrete temperature in a grid block drops below the critical value, and hence, it undergoes a jump in the thermal diffusivity.

To enhance the stability of the numerical finite volume scheme applied to phase-change problems, there are several routes we can take. First, the averaging of the diffusivity at the grid interface has a big influence on the amount of oscillation in the solution. Instead of a standard arithmetic or harmonic average, we can opt for an integral average to smooth out the jump in the diffusivity [2]. This can also be viewed as applying a flux-corrector method that interpolates between neighboring diffusivity values, similar to hyperbolic solvers with a flux-correction scheme. While the integral average removes most of the temporal oscillations and increases stability and convergence of the method, it is very grid-dependent and assumes a linear temperature transition around the discontinuous interface, which is highly non-linear in reality.

To have a more robust, stabilizing scheme that works for a general set of discontinuous or strongly non-linear parabolic problems, we look at alternatives that are less grid-dependent and mimic the intrinsic properties of the original equations. The class of mimetic schemes is based on the underlying properties of the partial differential equations, and uses theorems from vector calculus to derive the discrete equations (See for example, in [17–19]). This approach can also be used to handle discontinuities in the variables. In [19], a mimetic discretization is derived on a staggered grid for discontinuities that are located at grid interfaces.

In this Chapter, we provide some ideas to extend the mimetic discretization schemes to problems with discontinuities that do not lie on grid interfaces (if one uses an equidistant, static grid this is usually the case for phase change problems). For example, when dealing with one or more discontinuities, an extra node can be added at the approximated place of each discontinuity. This node can be indirectly solved for, so no extra degrees of freedom are added, to retain the computational efficiency of the scheme. This means that in the grid block containing a discontinuity, the fluxes through the interface are adapted, allowing for a more accurate solution when using a coarser grid. There are

several ways to incorporate this extra node in the numerical scheme. We address some of them and discuss their respective (dis)advantages. This method can also be extended to highly non-linear functions, where the coefficient changes several orders of magnitude over a small distance, by introducing an artificial grid block around the non-linearity. If the transition width goes to zero, this approach equals the one where we introduce an extra node. We compare the outcome of these methods with each other, and show that solving the discontinuity over an extra grid block increases the accuracy of the problem if we manage to approximate the phase interface position correctly. This provides us with a better control over the stability of the scheme.

Before we introduce the mimetic schemes, we give a short overview of other discretization methods that are used to solve phase change problems. These can be roughly divided into two classes, the deforming grid methods and the fixed grid methods. In the first class, the spatial or temporal grid is adapted so that discontinuities are always located at the grid interfaces, and hence, an appropriate interface condition can be enforced. For this one needs to track the interface, by using a level-set method, for example. In the second class of methods, the problem is rewritten in terms of enthalpy to approximate the interface position correctly without tracking it [16, 20]. From the enthalpy in the grid-cell containing the phase interface, the phase-fraction can be determined, which is then used to locate the approximate interface position. A disadvantage of these methods is that it is not always possible to rewrite the equations in terms of enthalpy. However, if there is an enthalpy formulation, we show in a comparative study that this method is a good alternative to the methods described above.

This chapter is organized as follows, in Section 3.2 we describe the general model for phase change problems. After that, we present a short survey of existing classes of numerical schemes for phase change problems in Section 3.3. This includes the fixed grid-methods, which make use of an enthalpy formulation, and an introduction to deforming grid schemes. Also we discuss the class of mimetic finite volume methods in Section 3.3.3, where special attention is paid to the computation of the diffusion coefficient at the grid interfaces. This last class of methods is then extended to semi-adaptive methods in Section 3.4, in which an extra grid node or grid cell is added implicitly to the scheme. This results in two new discretization schemes for phase change problems. These new schemes are compared with existing approaches for some practical examples in Section 3.5.

The first example is about a liquid that is cooled at the outer edge, so that it will freeze. By using the enthalpy method and an adaptive grid method, we can observe an improvement in the solutions compared to the standard finite volume method. The semi-adaptive grid methods, however, suffer from instabilities. The second example, considers the strongly degenerate function that was studied in Chapter 2, and we show that the observed numerical error increases when the functions become more degenerate. In the third example, we solve a discontinuous diffusivity function that resembles the total mobility function of the local equilibrium foam model studied in [2]. This leads to extra complications, due to an additional third immiscible phase. In the conclusions we summarize the used methods, and give suggestions for how to extend them to more dimensions and more complicated models, like the two-phase local-equilibrium foam model introduced in Chapter 1.

3.2. GENERIC MODEL FOR PHASE CHANGE PROBLEMS

We consider a one-dimensional parabolic equation with a discontinuous coefficient. As a general example of this we use the one-dimensional heat equation, defined by

$$\partial_t T = \partial_x(a(T)\partial_x T), \quad 0 < x < l, t > 0, \quad (3.1)$$

where T is the temperature, $a(T) = k/(c\rho)$ is the thermal diffusivity coefficient, k is the thermal conductivity, c the specific heat and ρ the density of the material. The thermal diffusivity is given by a piecewise continuous function, defined as

$$a(T) := \begin{cases} \alpha_1, & T < T^*, \\ \alpha_2, & T > T^*, \end{cases} \quad (3.2)$$

with a fixed threshold value $T^* \in \mathbb{R}$ and $\alpha_{1,2}$ can be constants or continuous functions of the temperature. This model describes the temperature change of a medium that undergoes a phase change, for example a liquid that turns into a solid as described in an example in Section 3.5. A model that describes this problem is referred to in literature as a Stefan problem [14–16]. At the phase interface $x(t) = \xi(t)$ where $T(\xi(t), t) = T^*$ the partial differential equation (PDE) is not valid, because of the discontinuous derivatives. Therefore an additional (physical) constraint, called the Stefan condition, is required here. For example, for constant $\alpha_{1,2}$ we can require that the derivatives of the temperature on both sides of the boundary are continuous in ξ , and hence

$$\alpha_1 \partial_x T(\xi(t)^-, t) = \alpha_2 \partial_x T(\xi(t)^+, t), \quad t > 0, \quad (3.3)$$

or alternatively we can require conservation of the heat flux at the interface, given by

$$\xi'(t) = \alpha_1 \partial_x T(\xi^-, t) - \alpha_2 \partial_x T(\xi^+, t), \quad t > 0. \quad (3.4)$$

Using a standard finite volume scheme to solve Eq. 3.1 will not incorporate this interface condition, instead it will ignore the fact that we are dealing with a discontinuous variable, and solve it as if it was a continuous phase. This is when potential stability problems occur around the interface, because every time the interface passes through a grid block, the scheme will over- or underestimate the actual temperature in a grid block. After the interface has passed, this will be corrected, because it is again in a continuous region. Hence the solutions will display an oscillatory behavior in time, as was shown in Van der Meer *et al.* [2]. In this chapter it was observed that these stability issues not only occur because of discontinuous variables, but that highly non-linear variables can have the same effect. Moreover, by ignoring the fact that we are dealing with two different phases instead of one, the scheme will converge much slower and give less accurate or even diverging solutions. Hence, it is important to incorporate the interface condition in the numerical scheme. According to Voller [16], there are two classes of numerical solvers to treat this problem. First, there is the class of fixed-grid methods, which reformulate the problem in terms of enthalpy and solve for the enthalpy. The Stefan condition is indirectly incorporated in these kind of schemes through the enthalpy formulation. These methods are introduced in Section 3.3. Then there is a second class of front-tracking and deforming grid methods that track the front and add additional

nodes around or at the interface. The Stefan condition can be enforced directly through the flux at the interface location. We will discuss these methods in the second part of Section 3.3. In Section 3.4, we propose some alternative methods that are a combination of those two classes. Instead of deforming the grid, we approximate the interface location by using polynomial interpolation, and then we adapt the flux through the grid interface surrounding the phase interface by indirectly adding an extra node at the interface location. We will show that this is computationally less expensive than the adaptive grid method, but the results can be less accurate because of the assumptions we have to make on the solution. We start, however, by introducing an alternative way to look at the spatial discretization of parabolic equations by Lipnikov *et al.* [19], which will serve as a framework for the other methods.

3.3. SURVEY OF EXISTING NUMERICAL SCHEMES

Below we give a short overview of two classes of methods that are used for phase change problems, namely the fixed grid methods that make use of an alternative formulation of the problem, if available, and the class of deforming grid methods, that somehow track the interface and adapt the grid accordingly. The third class of methods we discuss are the mimetic finite volume discretization methods. Those methods are a generalization of standard finite volume methods, and aim to mimic the properties of the continuous solution of the analytic equations by making use of the underlying theorems and identities of vector Calculus [17–19]. Because of this approach, these methods are able to handle discontinuities in the variables when they appear at a grid interface [19]. We will introduce this class of methods in Section 3.3.3, and provide our own extension in Section 3.4 to handle discontinuities that do not appear at a grid interface, but lie in-between two interfaces.

3.3.1. FIXED GRID METHODS: ENTHALPY FORMULATION

Instead of discretizing and solving the heat equation in terms of the temperature, it can be rewritten in terms of enthalpy [16], which can be defined as a function of temperature and pressure. The advantage of this formulation is that no additional interface condition is needed, since this information is indirectly included in the formulation through the liquid fraction. The liquid fraction at each point is described as a function of the enthalpy, and can have a continuous value between zero and one. Hence, we do not need to keep track of the interface location in our numerical scheme. This means also that it is possible to solve for both phases at once, as if it was one phase. According to Voller [16] this scheme can be applied to more general cases, involving a phase change that is not necessarily described by a single discontinuity, if one can come up with a proper enthalpy formulation.

The discretized version of the enthalpy formulation of Eq. 3.1 can be derived by conservation of energy in a control volume, which leads to

$$\partial_t E_\Delta + \mathbf{div}^k q_\Delta = 0, \quad (3.5)$$

where k is the thermal conductivity and

$$\left(\mathbf{div}^k q_\Delta\right)_i = \frac{(k_{i+1/2} q_{i+1/2} - k_{i-1/2} q_{i-1/2})}{\Delta x}, \quad (3.6)$$

is the divergence operator applied to the heat flux. The heat flux can be computed by using any suitable finite volume method. For example we can approximate $k_{i+1/2}$ by a the harmonic average $k_{i+1/2}^H$, so that

$$k_{i+1/2} q_{i+1/2} = -k_{i+1/2}^H (T_{i+1} - T_i), \quad k_{i+1/2}^H = \frac{2\tilde{k}^{i-1}\tilde{k}^{i+1}}{\tilde{k}^{i-1} + \tilde{k}^{i+1}}, \quad (3.7)$$

where \tilde{k} are the averaged values of k in a grid cell.

LIQUID FRACTION APPROXIMATION

Since the liquid fraction in each node, λ_i , can take on a continuous value between zero and one, it is a measure for the interface position within that cell. To approximate the location of the interface using the enthalpy of the solution, one needs to know the grid cell in which the interface is located. This is done by linear interpolation between the enthalpy values in the grid cells, and locating the root of the interpolated function. The approximate location is then determined by [20]

$$\xi^n = x_{m-1/2} + (1 - \lambda_m^n) \Delta x, \quad (3.8)$$

where $\lambda_m^n \in [0, 1]$ is the liquid fraction in the control volume $V_m = [x_{m-1/2}, x_{m+1/2}]$, given by

$$\lambda_i^n = \begin{cases} 0, & E_i^n \leq 0, & \text{(solid)} \\ E_i^n / \rho L, & 0 \geq E_i^n \geq \rho L, & \text{(interface)} \\ 1, & E_i^n \geq \rho L, & \text{(liquid)} \end{cases} \quad (3.9)$$

where L is the latent heat and ρ the material density.

For a standard finite volume scheme the liquid fraction is assumed to be either zero or one in a grid node, based on the temperature in that node. Hence, for these kind of schemes the interface position is always assumed to be on the grid interface for an equidistant grid, leading to significant numerical errors.

3.3.2. DEFORMING GRID METHODS: FRONT TRACKING

The second class of adaptive or deforming grid methods track the phase interface to ensure the interface conditions are met. Hence, these methods are based on the complete Stefan formulation, in which the problem is defined as two separate problems that are connected through the phase interface [16]. The advantage of these methods over the fixed grid methods is that they are more accurate, the disadvantage is the larger computational effort due to grid deformation. Initially, the phase interface is assumed to be at one of the domain boundaries. As the solution evolves in time, the interface will move through the domain with a velocity $\xi'(t)$, which is given by the Stefan condition 3.4. If this equation is discretized in space it follows that

$$\xi'(t) = \alpha_1 \frac{T^* - T(\xi(t) - \Delta x, t)}{\Delta x} - \alpha_2 \frac{T(\xi(t) + \Delta x, t) - T^*}{\Delta x}, \quad (3.10)$$

where $\Delta x = \Delta x(t)$ depends on the chosen grid method, which will change for every time step as the phase interface evolves. Hence, by using the forward Euler method in time, one obtains

$$\xi(t^{n+1}) = \xi(t^n) + \frac{\Delta t}{\Delta x} (\alpha_1(T^* - T(\xi(t^n) - \Delta x, t^n)) - \alpha_2(T(\xi(t^n) + \Delta x, t^n) - T^*)). \quad (3.11)$$

By using interpolation between the grid nodes, the new solution is mapped from the old one onto the new grid [21]. Together with the semi-discrete heat equation for the left and right phase (T_1 and T_2 , respectively)

$$\partial_t T_1 = \alpha_1 \partial_{xx} T_1, \quad 0 < x < \xi(t), t > 0, \quad (3.12)$$

$$\partial_t T_2 = \alpha_2 \partial_{xx} T_2, \quad \xi(t) < x < l, t > 0. \quad (3.13)$$

This gives a system of three equations and three unknowns, $T_1(x, t)$, $T_2(x, t)$ and $\xi(t)$. Alternatively, the Stefan condition can be added as a Lagrangian constraint to the discretized equations, as is done for the third mimetic scheme in Section 3.3.3. The system can be solved on the deformed grid with an appropriate time integration method. If chosen with care this will lead to a very accurate solution. A poorly chosen grid however, can lead to erroneous solutions. For more details we refer to Voller [16], which provides a good insight into the particularities of deforming grid methods.

Another way to make sure that the phase interface will be located at a grid interface for each time step [16], is to tune the time step accordingly. Then the third mimetic method in Section 3.3.3 can be applied at the discontinuous interface. Alternatively the time step can be chosen such that the interface is always located in a grid node as described in Javierre *et al.* [21]. The advantage of this method is that we can be sure no temporal oscillations will occur in the solutions. The disadvantage is that in order to compute the solution at a certain in-between time, interpolation is required. Moreover, if the time step is too large compared to the grid step (i.e. the interface moves very slowly) the solutions can become unstable in space. Hence it is recommended to use an implicit time discretization, like the backward Euler scheme, in this case. A major disadvantage of this method is that it is not possible to apply it in higher spatial dimensions, which is why we do not consider it suitable for our purposes.

3.3.3. MIMETIC SCHEMES

We can rewrite the parabolic heat equation 3.1 as a hyperbolic conservation law, as follows

$$\partial_t T + \partial_x(a(T)q) = 0, \quad q = -\partial_x T, \quad (3.14)$$

where q is the heat flux. This equation is discretized on an equidistant grid with grid size Δx using the mimetic scheme described in Lipnikov *et al.* [19], such that

$$\dot{T}_\Delta + \mathbf{div}^a q_\Delta = 0, \quad q_\Delta = -\mathbf{grad} T_\Delta, \quad (3.15)$$

where T_Δ and q_Δ are the semi-discrete unknowns, and the primary mimetic operator \mathbf{div} in the i -th grid cell is given by

$$(\mathbf{div}^a q_\Delta)_i = \frac{(a_{i+1/2} q_{i+1/2} - a_{i-1/2} q_{i-1/2})}{\Delta x}. \quad (3.16)$$

The secondary mimetic operator **grad** is derived by discretizing the integration by parts formula

$$\int_0^1 a(\partial_x T) q dx = - \int_0^1 \partial_x(aq) T dx. \quad (3.17)$$

The left side of this formula can be discretized in several ways, leading to three different types of discretization schemes (see Lipnikov *et al.* [19]). The main difference with standard finite volume schemes is that these schemes discretize the **div^a** operator, instead of the **div** operator. This leads to a more versatile set of schemes that can handle a larger range of functions a .

FIRST MIMETIC SCHEME

In the first mimetic scheme, a is assumed to be constant in every grid block, so that

$$a_{i+1/2} q_{i+1/2} = -a_{i+1/2} (\mathbf{grad} T)_{i+1/2} = \frac{a_{i+1/2}^2}{a_{i+1/2}^A} \frac{T_i - T_{i+1}}{\Delta x}, \quad (3.18)$$

where $a_{i-1/2}$ is the approximated value of a at the i -th interface, and

$$a_{i+1/2}^A = \frac{\tilde{a}^i + \tilde{a}^{i+1}}{2\Delta x} \quad (3.19)$$

is the arithmetic average at the i -th interface, and \tilde{a} denotes the constant approximation of a in a grid block. For example, $\tilde{a}^i = k(T_i)$ and $a_{i+1/2}$ can be the harmonic or arithmetic average of \tilde{a}^i and \tilde{a}^{i+1} , or a different approximation.

SECOND MIMETIC SCHEME

The second mimetic scheme assumes that a is a linear function of x in each grid block, connecting the values of $a_{i+1/2}$ at the interfaces. This leads to a simple approximation of the flux, given by

$$a_{i+1/2} q_{i+1/2} = -a_{i+1/2} (\mathbf{grad} T)_{i+1/2} = a_{i+1/2} \frac{T_i - T_{i+1}}{\Delta x}, \quad (3.20)$$

This scheme is commonly used as the standard finite volume method, in which **div** is discretized directly.

THIRD MIMETIC SCHEME

The last mimetic scheme considers a parameter a , which can become discontinuous at the grid interfaces, thus leading to an undefined quantity at the interface. As a solution the authors of [19] allow a to make a jump at the interface and replace $a_{i+1/2}$ and $q_{i+1/2}$ by two limiting values on both sides of the interface, $a_{i+1/2}^i$ and $a_{i+1/2}^{i+1}$, that are coupled through the following interface condition

$$a_{i+1/2}^i q_{i+1/2}^i = a_{i+1/2}^{i+1} q_{i+1/2}^{i+1}, \quad (3.21)$$

which is enforced in the numerical scheme through a Lagrangian constraint. Deriving the gradients on both sides of the interface and coupling them through the above condition leads to a scheme that is able to solve for the PDE with a discontinuous coefficient:

$$(\mathbf{grad} T)_{i+1/2}^i = \frac{\lambda_{i+1/2} - T_i}{\Delta x}, \quad (\mathbf{grad} T)_{i+1/2}^{i+1} = \frac{T_{i+1} - \lambda_{i+1/2}}{\Delta x}. \quad (3.22)$$

Here, $\lambda_{i+1/2}$ is a Lagrange multiplier to ensure that Eq. 3.21 is satisfied on each interface. If these equations are substituted into Eq. 3.21, this gives the value of $\lambda_{i+1/2}$

$$\lambda_{i+1/2} = \frac{a_{i+1/2}^i T_i - a_{i+1/2}^{i+1} T_{i+1}}{a_{i+1/2}^i + a_{i+1/2}^{i+1}}. \quad (3.23)$$

Substituting this back into the flux equations 3.22 leads to a numerical flux given by

$$a_{i+1/2} q_{i+1/2} = \frac{2a_{i+1/2}^i a_{i+1/2}^{i+1}}{a_{i+1/2}^i + a_{i+1/2}^{i+1}} \frac{T_i - T_{i+1}}{\Delta x}. \quad (3.24)$$

Hence, if the limiting values are equal when there is no discontinuity at the interface, such that $a_{i+1/2} = a_{i+1/2}^i = a_{i+1/2}^{i+1}$, and the scheme resembles the second mimetic scheme. For staggered grids, the scheme becomes:

$$a_{i+1/2} q_{i+1/2} = \frac{a_{i+1/2}^i a_{i+1/2}^{i+1} (\Delta x_i + \Delta x_{i+1})}{a_{i+1/2}^i \Delta x_{i+1} + a_{i+1/2}^{i+1} \Delta x_i} \frac{T_i - T_{i+1}}{(\Delta x_i + \Delta x_{i+1})/2}. \quad (3.25)$$

A limitation of this scheme is that the discontinuity is assumed to be located at a grid interface. In our problem the discontinuity can be anywhere in the grid, and moves in both space and time. Therefore, in the coming sections we review the problems that arise when dealing with these kind of functions, and come up with alternatives to this scheme. In Section 3.4.1 we look at ways to generalize the third mimetic scheme to cases where the discontinuity moves through the grid in time, while maintaining an equidistant scheme, which we call the fourth mimetic schemes.

3.4. DEVELOPMENT & ANALYSIS OF NEW MIMETIC SCHEMES

As we can see from the numerical results in Section 2.4 in Chapter 3, the first temporal oscillation is always upward, which means that in the grid block under consideration $f_{in} > f_{out}$. To compensate for this non-physical rise in temperature, the scheme will overcompensate in the next time step and hence $f_{out} > f_{in}$, causing an oscillatory pattern, that moves through the domain. Hence, from an engineering perspective, we need to decrease f_{in} initially, and increase f_{out} a little bit for the grid block where the discontinuity is located. This can be obtained, by making sure that the interface conditions established in Section 3.2 and applied in the third mimetic method of Section 3.3.3, are obeyed.

To enforce the interface conditions we need to know the interface location. Instead of tracking the interface and/or adapting the grid, we choose to keep the same discretization and grid, but in each time step the location of the interface is approximated by a polynomial function. Then the fluxes through the grid cell interfaces surrounding the discontinuous phase interface, are adapted to ensure monotonicity of the solution in time. This can be done by introducing a grid interface at the phase interface, so that we split the grid cell in two cells. The flux through the interface is then computed by the third mimetic method from Section 3.3.3 and used to compute the new temperature values at the next time step. Then the solution is interpolated back to the old grid, using

a linear or higher-order polynomial through the grid centers making sure that we have energy conservation. If the model contains a highly non-linear coefficient instead of a discontinuity, instead of an additional grid interface an additional grid cell can be introduced around the non-linearity. The width of this grid cell can be much smaller than the other grid cells, depending on the steepness of the non-linearity. Now the flux through the new grid interfaces can be computed, by using either the first or second mimetic scheme, and the temperature values at the next time step can be interpolated back to the original grid. In the next Section 3.4.1 these methods are explained further, and are referred to as the fourth mimetic schemes.

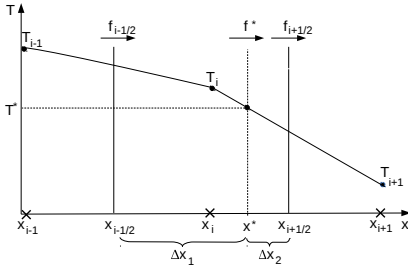
Alternatively, the temperature variables in the new grid cells left and right of the discontinuous interface, can be solely used to compute the diffusivity coefficients in those cells. Those coefficients are then used to approximate the fluxes through the surrounding grid interfaces, based on the distance between the grid interfaces and the phase interface. Hence, the flux through the approximated phase interface is not used, and the additional interface just serves as a separation, to allow multiple diffusivity values in one grid cell. In case of a non-linearity instead of a discontinuity, the scheme is split in three cells, and three diffusivity values are allowed for. Only the two outer values are used to update the fluxes at the surrounding grid interfaces. Energy conservation is not an issue here, since only the fluxes are adapted. We call these schemes the fifth mimetic schemes. In the following sections we will explain these approaches and present a comparative numerical study in Section 3.5.

3.4.1. FOURTH MIMETIC SCHEMES

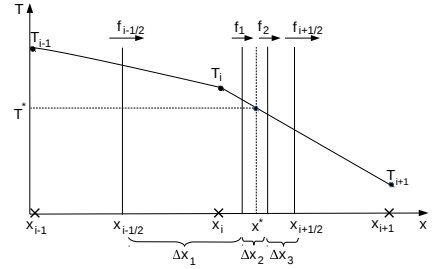
The fourth mimetic schemes incorporate the discontinuity in the coefficients by adapting the unknowns in the grid cell where the discontinuous interface is located. This is done by splitting the cell in two or three sub-cells and calculating the new value of the unknowns in those cells. The fluxes through the interface are then calculated based on these new unknowns. Below we give three alternative ways we looked at to implement these ideas, of which the first one has the highest potential and the last method leads to more numerical problems.

INTRODUCING AN EXTRA GRID INTERFACE

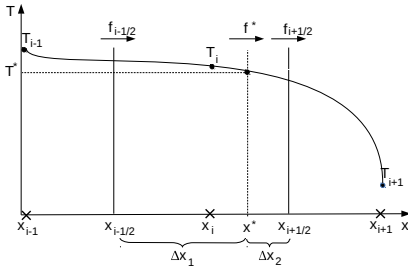
To get around the problem of having to track the interface, we first propose to add an extra grid interface at the approximate location of the phase interface and solve for this node implicitly so that the grid remains the same. We consider the numerical solution of the heat equation with discontinuous conductivity given by Eq. 3.2, with a discontinuity located at the right of grid center $x_{i-1/2}$ at a certain time t^n , as depicted in Fig. 3.1. Since we know the temperature values in the grid centers, we can approximate the location of the discontinuity by interpolating a linear or quadratic curve through these points left and right from the discontinuity. We then introduce an extra interface at the approximated location of discontinuity, so that the grid cell of the discontinuity is split into two parts. The new temperature values, called T_1 and T_2 for now, can be approximated at the discrete time interval by integration of the linear polynomial approximating T in this grid cell. Since we want our method to be mass conservative, the following condition



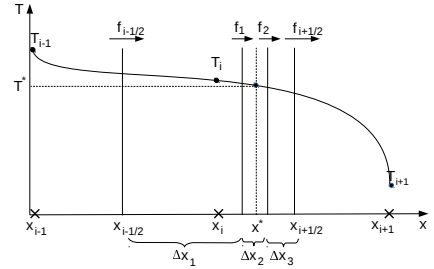
(a) extra node linear approximation



(b) extra cell linear approximation



(c) extra node higher-order polynomial



(d) extra cell higher-order polynomial

Figure 3.1: Schematic representation of the fourth mimetic method on a one-dimensional grid, for a problem with a discontinuous or highly non-linear diffusion coefficient in T^* . The point ξ is the approximate location of the discontinuity at a certain discrete time t^n , which is approximated by a linear (upper figures) or higher-order polynomial (lower figures). The flux f^* through ξ is the approximated numerical flux through that point, and f_1 and f_2 are the approximated fluxes through the grid boundaries of the added grid cell (right figures).

has to be satisfied

$$\Delta x T_i = \Delta x_1 T_1 + \Delta x_2 T_2, \quad (3.26)$$

where Δx_1 and Δx_2 are the sizes of the respective grid blocks, such that $\Delta x = \Delta x_1 + \Delta x_2$. Concisely, the scheme is as follows:

1. Find the interface location $x_{i-1/2}$ for which $T_{i-1}^n > T^* > T_i^n$.
2. Approximate ξ at time t^n such that $p(\xi) = T^*$, where the coefficients of the polynomial p are found by linear or quadratic interpolation through T_{i-1}^n and T_i^n .
3. Find the index j for which $x_{j-3/2} < \xi < x_{j-1/2}$.
4. Split the j -th cell in two parts, separated by the approximated phase interface.

5. Approximate T in the center of both new cells, T_1 and T_2 , by the polynomial p and make sure the total temperature in the cell is "conserved".
6. Calculate the temperature values in the next time step, by using the third mimetic scheme of Section 3.3.3 on the new grid interface. Apply a standard averaging scheme (mimetic 2) or the first mimetic method, to approximate the diffusivity on the other grid interfaces.
7. Interpolate the new temperature values back to the original grid by linear or quadratic interpolation, and take into account the conservation of energy.

Below, we develop these ideas further for a linear and quadratic polynomial. Of course, higher order polynomials can be used too, but this involves more grid points and thus leads to complications at the boundary and a more extensive implementation and higher computational costs. On the other hand, it is possible to approximate the real solution better with a higher order polynomial, which will lead to a better approximation of the interface location. We leave it to the interested reader to develop this further.

Linear interpolation A linear approximation of the temperature is depicted in Fig. 3.1a. It then follows that

$$\Delta x \partial_t T_i = \Delta x_1 \partial_t T_1 + \Delta x_2 \partial_t T_2, \quad (3.27)$$

with

$$\dot{T}_1 = -\frac{1}{\Delta x_1} [f^*(T_2 - T_1) - f_{i-1/2}(T_1 - T_{i-1})], \quad (3.28)$$

$$\dot{T}_2 = -\frac{1}{\Delta x_2} [f_{i+1/2}(T_{i+1} - T_2) - f^*(T_2 - T_1)], \quad (3.29)$$

where f^* is the flux through the interface ξ , where the diffusivity a is discontinuous. The numerical fluxes $f_{i-1/2}$ and $f_{i+1/2}$ denote the fluxes through the cell interfaces located at $x_{i-1/2}$ and $x_{i+1/2}$, respectively, and are given by

$$f_{i-1/2} = \frac{a_{i-1/2}^2}{\Delta x \tilde{a}^{i-3/2} + \Delta x_1 \tilde{a}^1}, \quad (3.30)$$

$$f_{i+1/2} = \frac{a_{i+1/2}^2}{\Delta x_2 \tilde{a}^2 + \Delta x \tilde{a}^{i+1/2}}. \quad (3.31)$$

Substituting Eq. 3.29 into 3.26 yields an expression for the time derivative of T_i :

$$\dot{T}_i = \frac{1}{\Delta x} [f_{i+1/2}(T_{i+1} - T_2) - f_{i-1/2}(T_1 - T_{i-1})]. \quad (3.32)$$

Hence, in this expression the flux f^* cancels out. Furthermore, if either T_1 or T_2 is expressed as a function of T_i , we can derive the other one from Eq. 3.26. For example, if we approximate the temperature by a continuous linear polynomial $u(x)$, T_2 follows immediately from evaluating this function in $x_2 = x^* + \Delta x_2/2$. In this case, we obtain

$$\dot{T}_i = \frac{1}{\Delta x} [\tilde{f}_{i+1/2}(T_{i+1} - T_2) - f_{i-1/2}(T_1 - T_{i-1})], \quad (3.33)$$

$$\tilde{f}_{i+1/2} = (1 - \alpha) f_{i+1/2} - \frac{\Delta x_2}{\Delta x_1} \alpha f_{i-1/2}. \quad (3.34)$$

where $\alpha = \frac{(x_2 - x_{i-1/2})}{\Delta x}$ is the distance of the new (virtual) grid point to the old one. Hence, the right flux $f_{i+1/2}$ is replaced by $\tilde{f}_{i+1/2}$, which contains an additional term to account for the discontinuity. When the discontinuity is exactly at the center of the i -th grid block, it follows that $\tilde{f}_{i+1/2} = \frac{f_{i-1/2} + f_{i+1/2}}{2}$, and hence, the change of T_i is mainly dictated by the diffusion coefficients left of the discontinuity. On the other hand, if the discontinuity is located at the right interface, i.e. $\Delta x_1 = 1$ and $\Delta x_2 = 0$, the original scheme is recovered.

Quadratic interpolation For a more accurate approximation of the interface position we can take into account three nodes around and including the grid cell containing the discontinuity and draw a quadratic polynomial \tilde{T} through them. Starting from

$$\dot{T}_i = \frac{1}{\Delta x} [f_{i+1/2}(T_{i+1} - T_2) - f_{i-1/2}(T_1 - T_{i-1})]. \quad (3.35)$$

The value of the temperature in x_2 , T_2 , can now be expressed by integrating over the quadratic polynomial through T_i , T_{i+1} and T_{i+2} , such that

$$T_2 = \frac{1}{\Delta x_2} \int_{\Delta x_2} \tilde{T}(x) dx|_{x=x_2} = \frac{1}{\Delta x_2} \int_{\Delta x_2} \frac{1}{3} ax_2^3 + \frac{1}{2} bx_2^2 + cx_2 \quad (3.36)$$

where a, b, c are the coefficients of the quadratic polynomial, and T_1 follows from Eq. 3.26. Alternatively, we can evaluate the polynomial in x_2 , such that $T_2 = \tilde{T}(x_2)$. We can rewrite \tilde{T} in terms of T_i , T_{i+1} and T_{i+2} , such that

$$\tilde{T} = \alpha T_{i-1} + \beta T_i + \gamma T_{i+1}. \quad (3.37)$$

If we rewrite Eq. 3.32, deriving T_2 from Eq. 3.37, it follows that

$$\dot{T}_i = \frac{1}{\Delta x} [\tilde{f}_{i+1/2} T_{i+1} - T_2) - \tilde{f}_{i-1/2} (T_1 - T_i)], \quad (3.38)$$

with

$$\tilde{f}_{i-1} = (1 - \gamma) f_{i+1/2} - \frac{\Delta x_2}{\Delta x_1} \gamma f_{i-1/2}, \quad (3.39)$$

$$\tilde{f}_{i+1/2} = (1 + \frac{\Delta x_2}{\Delta x_1} \alpha) f_{i-1/2} - \alpha f_{i+1/2}, \quad (3.40)$$

and hence

$$\tilde{f}_{i-1} + \tilde{f}_{i+1/2} = (1 + \frac{\Delta x_2}{\Delta x_1} (1 - \beta)) f_{i-1/2} + \beta f_{i+1/2}. \quad (3.41)$$

INTRODUCING AN EXTRA GRID CELL

In case of a highly non-linear conductivity function, instead of a truly discontinuous one, we could consider to introduce an extra grid cell that contains this transition (see Fig. 3.1b) if we know the approximate transition width. This way, we split the cell under consideration into three parts. Each part that is connected to the left and the right cell, is used to compute the average flux on the grid interfaces. The flux through the two additional interfaces surrounding the non-linearity is computed through a variation of the third mimetic method. When the size of the transition width goes to zero (i.e. a discontinuous conductivity) this will lead to the scheme discussed in Section 3.4.1 with an additional node.

3.4.2. FIFTH MIMETIC SCHEMES

In the previous schemes in Section 3.4.1, we altered the temperature based on a polynomial through the grid center values and energy conservation, and then implemented this directly into the numerical scheme. Here we also split the grid block in two at the discontinuity, and approximate the temperature in the middle of each new grid block, but we only use this information to calculate the value of a in the new grid block and use this to adapt the numerical flux at the interface. The temperature that is used in the scheme stays unaltered.

Since the value of the diffusivity coefficient a is averaged over each grid block, a jump in a is not recognized and instead averaged out over the entire grid length. Hence, left of the discontinuity the value of a is lower than in reality and right of the discontinuity it is higher. This causes the fluxes through the grid interfaces to be distorted. We allow the discrete diffusivity coefficient to undergo a jump at the approximated phase interface, and use the value left and right of this jump for each respective interface approximation.

Hence, we allow for a discontinuity in the parameters, while always keeping an energy conservative scheme. The averaging method on the grid interfaces can be adapted to the phase interface, by using weighted averaging that takes into account the distance of the grid interface to the phase interface. In the next paragraphs we introduce this scheme for cases with a single discontinuity in the parameters (See also Section 3.5.1), and we explain how to extend it for highly non-linear coefficients (See also Section 3.5.3). The extension to several discontinuities or non-linearities is trivial if the distance between the discontinuities is larger than the grid size.

ADAPTING THE NUMERICAL FLUX FOR DISCONTINUOUS COEFFICIENTS

Instead of substituting the interpolated variables into the numerical scheme, we can also just adapt the coefficients on each side of the interface by allowing for a jump inside a grid block. This means that we split the grid cell containing the discontinuity at the approximated location of the discontinuity and then determine the diffusivity value of the coefficient in the center of each new grid block. These values are then used to compute the (weighted) average on the interfaces. Hence, the scheme is as follows:

1. Find the interface location $x_{i-1/2}$ for which $T_{i-1}^n > T^* > T_i^n$.
2. Approximate ξ at time t^n such that $p(\xi) = T^*$, where the coefficients of the polynomial p are found by linear or quadratic interpolation through T_{i-1}^n and T_i^n .
3. Find the index j for which $x_{j-3/2} < \xi < x_{j-1/2}$.
4. Split the j -th cell in two parts, separated by the approximated discontinuous interface.
5. Approximate T in the center of both new cells, T_1 and T_2 , by the polynomial p .
6. Calculate the diffusivity in the new grid cells, by using the new temperature values T_1 and T_2 . Then apply a standard averaging scheme to approximate the diffusivity on the grid boundaries.
7. Adapt $f_{j-1/2}^n$ and $f_{j+1/2}^n$, by the approximated diffusivity values at the grid interfaces.

ADAPTING THE NUMERICAL FLUX FOR HIGHLY NON-LINEAR COEFFICIENTS

If one deals with highly non-linear coefficients, the previous scheme can be adapted for this. Again a linear or higher-order polynomial is drawn through the discrete temperature values. Instead of calculating the weights based on the approximate distance to the discontinuity, the approximate distance to the point with the steepest gradient is utilized. This is the point where the diffusivity coefficient is steepest with respect to the temperature, which is a fixed temperature value that can be calculated beforehand. This value is then applied in the previous scheme, as if it contained a discontinuity. This method can only be applied if the discontinuity is indeed highly non-linear. For smoother transitions, a standard finite volume scheme can be used.

3.4.3. SHIFTING THE GRID INTERFACE

Alternatively, we could shift the interface to the place of the discontinuity, hereby applying an adapted flux f^* on the discontinuous interface that is given by the third mimetic scheme described in Section 3.3.3. The difference with the scheme proposed in Section 3.4.1 is that we keep the same amount of grid cells, by shifting the grid interface closest to the phase interface to coincide with the phase interface. To do so, we approximate the location of the discontinuity by linear or quadratic interpolation. In the next time step the solution is interpolated back to the original grid, because otherwise we will have a highly unstructured grid with grid sizes that approach zero. However, it turns out that this approach triggers and worsens the oscillations, probably because of the interpolation errors and the large difference in grid sizes between neighboring grid cells. Therefore we do not proceed with this idea further, but with some improvements it could have more potential.

3.5. NUMERICAL EXAMPLES

3.5.1. EXAMPLE 1: FREEZING OF WATER

As an example of the techniques described above, we use a physical model from Tarwidi and Pudjaprasetya [20] describing a block of ice that is heated from one side, and melts into water when the temperature rises above zero degree Celsius (or 273 Kelvin (K)). The thermal conductivity of ice is higher than that of water due to its molecular structure, which will cause a jump in conductivity at the water-ice interface. The diffusivity $D(u)$ is therefore defined by

$$a(T) := \begin{cases} \alpha_s = k_s / (c_s \cdot \rho), & T < T^*, \quad (\text{solid}) \\ \alpha_l = k_l / (c_l \cdot \rho), & T > T^*, \quad (\text{liquid}) \end{cases} \quad (3.42)$$

where T is the temperature and $T^* = 273K$ is the freezing point. The other parameters are given in Table 3.1. Hence we can describe the process by the following set of linear heat equations,

$$\rho c_l \partial_t u = k_l \partial_{xx} T, \quad 0 < x < \xi(t), t > 0, \quad (\text{liquid}) \quad (3.43)$$

$$\rho c_s \partial_t u = k_s \partial_{xx} T, \quad \xi(t) < x < l, t > 0, \quad (\text{solid}) \quad (3.44)$$

parameter	unit	value	explanation
c_l	kJ (kg K)^{-1}	4.187	specific heat water
c_s	kJ (kg K)^{-1}	1.7	specific heat ice
k_l	W (m K)^{-1}	0.6	thermal conductivity water
k_s	W (m K)^{-1}	2.66	thermal conductivity ice
l	m	0.1	length of the domain
L	kJ kg^{-1}	333	latent heat melting
ρ	kg m^{-3}	1000	density
T^*	K	273	freezing point water
T_l	K	310	initial liquid temperature
T_s	K	73	temperature left boundary

Table 3.1: Model parameters for the first example in Section 3.5, partly taken from [20]

with two interface conditions

$$\rho L \xi'(t) = k_s \partial_x T(\xi^-, t) - k_l \partial_x T(\xi^+, t), \quad t > 0, \quad (3.45)$$

$$T(\xi, t) = T^*, \quad t > 0, \quad (3.46)$$

to ensure conservation of the heat flux and continuity at the interface. Boundary and initial conditions are given by

$$T(0, t) = T_s, \quad t > 0, \quad (3.47)$$

$$T(l, t) = T_l, \quad t > 0, \quad (3.48)$$

$$T(x, 0) = T_l, \quad 0 < x < l, \quad (3.49)$$

$$\xi(0) = 0, \quad x \geq 0. \quad (3.50)$$

ANALYTICAL SOLUTION

For this simple piecewise-linear model we can only derive an analytical solution on the semi-infinite domain $0 < x < \infty$. For the derivation we use the same approach as in Kraaijevanger [22] applied to the heat model in Van der Meer *et al.* [2]. First, we redefine the problem as two differential equations that describe the phase left and right of the phase interface, T_1 and T_2 , and obey the interface conditions Eq. 3.45 and Eq. 3.46. These conditions are enforced at the moving interface $\xi(t)$, which splits the domain $\Omega = (0, \infty)$ in two parts $\Omega_1 = (0, \xi(t))$ and $\Omega_2 = (\xi(t), \infty)$. The solutions T_1 and T_2 satisfy

$$T_1 > T^*, \quad x \in \Omega_1, \quad t > 0, \quad (3.51)$$

$$T_2 < T^*, \quad x \in \Omega_2, \quad t > 0, \quad (3.52)$$

$$T_1 = T_2 = T^*, \quad x = \xi(t), \quad t > 0. \quad (3.53)$$

Hence, we are solving the following initial boundary value problem for the left part of the solution

$$\partial_t T_1 = \alpha_s \partial_{xx} T_1, \quad 0 < x < \xi(t), \quad t > 0, \quad (3.54)$$

$$T_1(0, t) = T_s, \quad t > 0, \quad (3.55)$$

$$T_1(\xi, t) = T^*, \quad t > 0, \quad (3.56)$$

$$\xi(0) = 0, \quad x \geq 0, \quad (3.57)$$

and the right part of the solution

$$\partial_t T_2 = \alpha_l \partial_{xx} T_2, \quad \xi(t) < x < \infty, \quad t > 0, \quad (3.58)$$

$$T_2(\infty, t) = T_l, \quad t > 0, \quad (3.59)$$

$$T_2(\xi, t) = T^*, \quad t > 0, \quad (3.60)$$

$$T_2(x, 0) = 0, \quad x \geq 0, \quad (3.61)$$

$$\xi(0) = 0, \quad x \geq 0, \quad (3.62)$$

which are combined through the Stefan condition Eq. 3.45 at $x = \xi(t)$. To construct the solution we make use of the error function and its complement

$$\operatorname{erf}(z) = \frac{2}{\sqrt{\pi}} \int_0^z \exp(-y^2) dy, \quad (3.63)$$

$$\operatorname{erfc}(z) = 1 - \operatorname{erf}(z), \quad (3.64)$$

which satisfies $\operatorname{erf}(0) = 0$ and $\operatorname{erf}(\infty) = 1$. It can be deduced that the functions

$$T_1 = T_s + A \operatorname{erf}\left(\frac{x}{2\sqrt{\alpha_s t}}\right), \quad 0 < x < \xi(t), \quad t > 0, \quad (3.65)$$

$$T_2 = T_l + B \operatorname{erfc}\left(\frac{x}{2\sqrt{\alpha_l t}}\right), \quad \xi(t) < x < \infty, \quad t > 0. \quad (3.66)$$

satisfy Eq. 3.54 and Eq. 3.58 with Dirichlet boundary conditions 3.55 and 3.56 and initial condition 3.61 for any constants A and B . Condition 3.53 requires that these constants have to satisfy

$$T_s + A \operatorname{erf}\left(\frac{\xi(t)}{2\sqrt{\alpha_s t}}\right) = T_l + B \operatorname{erfc}\left(\frac{\xi(t)}{2\sqrt{\alpha_l t}}\right). \quad (3.67)$$

Hence, it follows that $\xi(t)$ has to be of the form

$$\xi(t) = 2\beta\sqrt{\alpha_s t}, \quad (3.68)$$

for some positive constant β , and A and B are given by

$$A = \frac{T^* - T_s}{\operatorname{erf}(\beta)}, \quad (3.69)$$

$$B = \frac{T^* - T_l}{\operatorname{erfc}(\beta)}, \quad (3.70)$$

where $v = \sqrt{\alpha_s/\alpha_l}$. The phase location $\xi(t)$ can be determined from the Stefan condition 3.45. If we substitute Eq. 3.68, Eq. 3.65 and Eq. 3.66 in Eq. 3.45, we obtain

$$\sqrt{\pi}\beta = \frac{\gamma_s}{\operatorname{erf}(\beta)\exp(\beta^2)} - \frac{\gamma_l}{\operatorname{erfc}(\beta v)\exp((\beta v)^2)}, \quad (3.71)$$

where γ_s, γ_l are constants given by

$$\gamma_s = \frac{c_s(T^* - T_s)}{L}, \quad (3.72)$$

$$\gamma_l = \frac{c_l(T_l - T^*)}{Lv}. \quad (3.73)$$

The first constant γ_s is sometimes called the Stefan number [16] and is defined as the sensible heat divided by the latent heat. The positive solution of Eq. 3.71 gives us the value of β , which is unique. Putting everything together, the analytical solution to the semi-infinite problem ($l \rightarrow \infty$) with a moving interface is

$$u_{\text{exact}}(x, t) = \begin{cases} T_s + (T^* - T_s) \operatorname{erf}\left(\frac{x}{2\sqrt{\alpha_s t}}\right) \operatorname{erf}(\beta), & 0 < x < \xi(t), t > 0, \text{ (solid)} \\ T_l - (T_l - T^*) \operatorname{erfc}\left(\frac{x}{2\sqrt{\alpha_l t}}\right) \operatorname{erfc}(\beta v), & \xi(t) < x < \infty, t > 0. \text{ (liquid)} \end{cases} \quad (3.74)$$

ENTHALPY FORMULATION

To find the location of the phase interface, we can rewrite the problem in terms of enthalpy (E) as in Tarwidi and Pudjaprasetya [20]. Enthalpy is defined as the sum of internal energy and volume times the pressure. If the system is homogeneous (constant density ρ) and closed, it follows from the first and the second law of thermodynamics that

$$dE = c_p dT + V(1 - \alpha \cdot T) dp, \quad (3.75)$$

where c_p is the heat capacity at constant pressure, V is the volume of the closed system p is the pressure and α the coefficient of thermal expansion. For an ideal gas $\alpha \cdot u = 1$ and hence

$$dE = c_p dT. \quad (3.76)$$

We assume that the specific heat, c_p , is independent of the temperature, and hence,

$$E = c_p T. \quad (3.77)$$

Because we cool the system from one side, energy is taken from the system. This energy is approximated by ρL , where L is the latent heat that is needed for the ice to turn into water. Hence, the enthalpy of the system is given by

$$E(x, t) = \begin{cases} \rho c_s (T(x, t) - T^*), & T < T^*, \text{ (solid)} \\ \rho c_l (T(x, t) - T^*) + \rho L, & T > T^*, \text{ (liquid)} \end{cases} \quad (3.78)$$

as shown in Fig. 3.2.

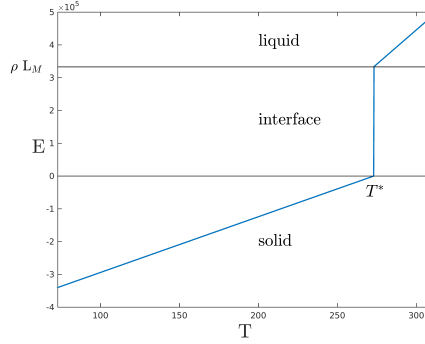


Figure 3.2: Enthalpy E (kJ) versus the temperature T (K) in Example 1.

The discretized version of these equations was given in Section 3.3 by Eq. 3.5-3.7. Using the second mimetic method, with a harmonic average for the flux approximation and a forward Euler scheme in time, this leads to

$$E_i^{n+1} = E_i^n + \frac{\Delta t}{\Delta x} (q_{i-1/2}^n - q_{i+1/2}^n), \quad i = 1, \dots, M, n = 1, \dots, N. \quad (3.79)$$

The energy flux is given by

$$q_{i-1/2} = -k_i^H (T_i - T_{i-1}), \quad (3.80)$$

where k_i^H is the harmonic average of the thermal conductivities in the grid cells. This reduces to

$$k_i^H = \begin{cases} k_s/h, & \text{(solid)} \\ k_l/h, & \text{(liquid)} \end{cases} \quad (3.81)$$

in a grid cell filled with only one phase. We can solve for this equation, and then compute the temperature by

$$T(x, t) = \begin{cases} T_m + \frac{E(x, t)}{\rho c_s}, & E \leq 0, & \text{(solid)} \\ T_m, & 0 \geq E \leq \rho L, & \text{(interface)} \\ T_m + \frac{E(x, t) - \rho L}{\rho c_l}, & E \geq \rho L. & \text{(liquid)} \end{cases} \quad (3.82)$$

The time step is chosen such that the stability condition, given by

$$\max \left(\frac{\Delta t k_s}{(\Delta x)^2}, \frac{\Delta t k_l}{(\Delta x)^2} \right) \leq \frac{1}{2}, \quad (3.83)$$

is satisfied. Because k is of order 10^{-3} , while the coefficient of the original equations $\alpha = k/(c\rho)$ is of an order 10^{-6} , the time step for the enthalpy formulation is much less restrictive than that for the original equations.

NUMERICAL RESULTS

In Fig. 3.3, the enthalpy method is compared with the mimetic schemes and the analytical solution, by using a harmonic average in space and a forward Euler scheme in time. The third mimetic scheme is applied to an adapted grid, where an additional node is added each time step at the approximated interface. The fourth and fifth mimetic methods are implemented using linear interpolation to approximate the phase interface, as described in Section 3.4.

The mimetic methods do not converge for any of the standard averaging methods. The third mimetic method is the only one that captures the right phase interface location, but has the highest numerical error for temperatures below the freezing temperature. The solutions of the first and second mimetic method, which do not make use of any interpolation techniques, move too fast. Hence the block of ice melts much faster according to these techniques, than in reality. The second mimetic method, which equals the standard finite volume method on a regular grid, performs slightly better than the first mimetic method. The last seems to converge to the same solution as for the second mimetic method, but oscillates strongly. For low grid resolution the first mimetic method approaches the true phase interface location, but then diverges away from it for higher resolutions.

The new mimetic methods implemented here, do approximate the interface by linear interpolation, but perform similarly to the second mimetic method, because they fail to approximate the correct interface location. This could be due to the low interpolation order, but also to an effect called harmonic locking: the approximated average is lower than in reality, which is why the numerical solutions are moving too fast. This effect is especially severe for problems with highly non-linear or discontinuous derivatives.

The enthalpy method performs much better for this problem and requires a less strict time step than the mimetic schemes. It is less accurate around the phase interface, as can be seen in Fig. 3.5, where the relative numerical error of the methods is depicted. The error is highest around the phase interface location and at the tail of the solution, and a convergence that is lower than first-order is observed when the grid resolution is increased. The error at the phase interface is due to a mismatch between the exact and numerical location as seen in Fig. 3.4 and the error at the tail of the solution is due to the fact that the analytic solution was derived on the semi-infinite domain, whereas the numerical solution is computed on a finite domain.

If we take a look at the approximated interface location in Fig. 3.4, we see that the numerical melting front is a little bit behind the analytical front. Of course this is also due to the fact that the analytical solution was derived on the semi-infinite domain. The interface location is indirectly incorporated into the enthalpy scheme, through the liquid fraction (Eq. 3.9), so it is not necessary to compute it separately.

The results also show that the enthalpy method, and the first three mimetic methods, lead to temporal oscillations in the solutions, which were also observed in Van der Meer *et al.* [2] for a similar model. Especially at lower resolutions ($N = 16, 32$), the oscillations are significant, but they damp out in time. Higher resolutions ($N = 64, 128$) do suffer much less from oscillatory behavior at the phase interface. The fourth and fifth mimetic scheme do not suffer from oscillatory behavior.

3.5.2. EXAMPLE 2: STRONGLY DEGENERATE PROBLEM

In this example, we look at the heat equation with a piecewise constant coefficient that was introduced in Chapter 2, where the diffusivity is given by

$$a(T) := \begin{cases} \epsilon, & T < T^*, \quad (\text{solid}) \\ 1, & T > T^*, \quad (\text{liquid}) \end{cases} \quad (3.84)$$

where $\epsilon \rightarrow 0$. The parameters are defined in Table 3.2 and the boundary and initial conditions are given by

$$T(0, t) = 1, \quad t > 0, \quad (3.85)$$

$$T(l, t) = 0, \quad t > 0, \quad (3.86)$$

$$T(x, 0) = 0, \quad 0 < x < l, \quad (3.87)$$

$$\xi(0) = 0, \quad x \geq 0. \quad (3.88)$$

This problem can be seen as a liquid-solid transformation, where the diffusivity of the liquid is much higher than for the solid. The solidification temperature is again denoted by $T^* > 0$. In the limit that ϵ goes to zero, the solution of this problem approaches a shock-like solution as shown in [22]. In [2], it was shown that the numerical solution of the finite volume method exhibits oscillatory behavior in time for any of the standard averaging schemes. An integral average over the piecewise constant parameter k was proposed as a remedy for oscillatory behavior. This corresponds to the choice

$$a_{i-1/2} = \frac{1}{T_i - T_{i-1}} \int_{T_{i-1}}^{T_i} a(v) dv. \quad (3.89)$$

Below we test the other mimetic methods proposed in Section 3.3.3 and Section 3.4.

parameter	value	explanation
ϵ	0.01	degenerate value
Δt	0.01	time step
Δx	0.1	grid size
l	0.1	length of the domain
T^*	0.7	point of discontinuity

Table 3.2: Model parameters for Example 2 in Section 3.5.2.

NUMERICAL RESULTS

The results of the enthalpy and mimetic schemes described in Section 3.3 (enthalpy method and mimetic schemes 1 to 3) and the new mimetic schemes described in Section 3.4.1 (mimetic 4) and Section 3.4.2 (mimetic 5), are depicted in Fig. 3.6. The first two mimetic schemes perform quite well but show oscillatory behavior in time. The third mimetic scheme is applied to an adaptive grid, where an extra node at the approximated phase interface location is added in each time step. The solution is also interpolated back, with a linear polynomial to the old grid. This method performs worse, presumably

parameter	unit	value	explanation
c	.	0.55	total compressibility
k	m^2	10^{-8}	rock permeability
l	m	0.1	length of the domain
L	kJ kg^{-1}	15	latent heat gas-foam transition
μ_g	$\text{kg m}^{-1} \text{s}^{-1}$	$1.4 \cdot 10^{-5}$	viscosity gas
μ_f	$\text{kg m}^{-1} \text{s}^{-1}$	$3 \cdot 10^{-2}$	viscosity foam
ϕ	.	0.3	porosity
p^*	$\text{kg m}^{-1} \text{s}^{-2}$	0.5	critical pressure foam collapse
ρ	kg m^{-3}	1	density

Table 3.3: Model parameters for Example 3 in Section 3.5.3.

due to the significant interpolation error. The fourth mimetic method performs better, as a quadratic interpolation polynomial is applied, as described in Section 3.4.2. The solution is still oscillatory in time, and although the result is slightly better than the first mimetic method, it performs worse than the second mimetic method. This is probably due to the in-exact prediction of the phase interface. The enthalpy method and the fifth mimetic scheme show the best results, although oscillatory behavior is still present for both methods.

NUMERICAL CONVERGENCE

As can be seen from the numerical error plots in Fig. 3.7 the error is smallest for the fifth mimetic method. For these kind of problems, where the initial temperature profile of the model is reversed relative to that of the previous example, the fifth mimetic method performs similarly or better than the enthalpy method. Both methods perform much better than the standard finite volume scheme (mimetic 2) and the other mimetic schemes.

3.5.3. EXAMPLE 3: FOAM MODEL

In the third example, we look at slightly compressible foam flow in a porous medium (the rock) of length l , inspired by the local-equilibrium foam model introduced in Chapter 1. The pressure decay in the porous medium is modeled by a parabolic equation with a discontinuous diffusion coefficient given by

$$c\phi\partial_t p + \partial_x q = 0. \quad (3.90)$$

Here, the c denotes the total compressibility of the material (rock and foam), which is assumed constant, and ϕ is the porosity of the rock. To describe the flux q as a function of the pressure gradient we use Darcy's law

$$q = -\frac{k}{\mu}\nabla p, \quad (3.91)$$

where k is the permeability of the rock, μ the fluid viscosity and ∇p the pressure gradient. The parameter values are given in Table 3.3.

We assume that the fluid in the porous medium can be either in gas state (low viscosity) or foam state (high viscosity) depending on the value of the pressure. When the

pressure exceeds a critical value, denoted by p^* , foam lamellae will break and the viscosity will drop instantaneously. Hence, the viscosity of the gas contains a discontinuity at a critical pressure. We model this by setting

$$\mu := \begin{cases} \mu_g, & p > p^*, & \text{(gas)} \\ \mu_f, & p < p^*. & \text{(foam)} \end{cases} \quad (3.92)$$

The interface conditions at the gas-foam interface $\xi(t)$ are defined by

$$\phi \xi'(t) = k \partial_x p(\xi^-, t) / \mu_g - k \partial_x p(\xi^+, t) / \mu_f, \quad t > 0, \quad (3.93)$$

$$p(\xi, t) = p^*, \quad t > 0. \quad (3.94)$$

Initially, the pressure in the porous medium is low, so only foam exists. Then the pressure on the left side of the domain is increased, so that the foam collapses and turns into gas again. Hence the interface between gas and foam, given by $\xi(t)$, will move to the right. Boundary and initial conditions are given by

$$p(0, t) = 1, \quad t > 0, \quad (3.95)$$

$$p(l, t) = 0, \quad t > 0, \quad (3.96)$$

$$p(x, 0) = 0, \quad 0 < x < l, \quad (3.97)$$

$$\xi(0) = 0, \quad x \geq 0. \quad (3.98)$$

ENTHALPY FORMULATION

It is possible to define the enthalpy of gas, foam and water under reservoir conditions when assuming a constant density and temperature, and derive the necessary interface conditions at the gas-foam and foam-water interface. Since enthalpy is a function of temperature and pressure, and the reservoir temperature is assumed to be constant, we can deduce that the enthalpy of gas is higher than that of foam, and additional enthalpy needs to be added to break the lamellae films.

The additional enthalpy or latent heat, denoted by L , is not well defined for this problem. We therefore tuned the latent heat L so that the solutions of the enthalpy method best matched the analytical solutions of the foam model. This turned out to be a really low number compared to the previous experiments, and is listed in Table 3.3. Hence, the enthalpy for the simplified foam model from this example is defined as

$$E(x, t) = \begin{cases} \rho \phi c(p(x, t) - p^*), & p < p^*, & \text{(foam)} \\ \rho \phi c(p(x, t) - p^*) + \rho \phi L, & p > p^*, & \text{(gas)} \end{cases} \quad (3.99)$$

where the density ρ is assumed constant for now, and the total compressibility is multiplied with the porosity of the rock.

NUMERICAL RESULTS

The results of this simplified foam model are depicted in Fig. 3.8. The third mimetic method does not converge and is therefore not included in the results. Moreover, the enthalpy formulation we used does not converge to the analytical solution, because the definition of the enthalpy for this model is not straightforward. The mimetic methods on the contrary all converge and do not differ much from each other.

SUGGESTIONS FOR THE LOCAL-EQUILIBRIUM FOAM MODEL

Of course, this is a highly simplified projection of the local-equilibrium foam model introduced in Chapter 1. In this model, the porous rock is initially filled with water mixed with surfactants, and pure gas is injected from the left side through an injection well. When the gas comes into contact with the water mixture, the water and surfactant will form lamellae that capture the gas in bubbles. This happens only when the water saturation exceeds a critical value. The critical water saturation can be linked directly to the critical capillary pressure, the pressure difference between water and gas.

Since the water saturation present in foam is negligible, foam is usually modeled as a gas with an increased viscosity (equivalent to a decreased mobility). Thus, the local equilibrium foam model is usually viewed as a two-phase model, where gas and water are two immiscible phases, and the mobility of the gas is a highly non-linear function that accounts for the effect of foam.

Unfortunately, this simplistic view of what is really happening leads to numerical problems [2, 23, 24]. It would be a better idea to treat this model as an extension to the model above, where foam is considered as another phase and the interface between gas and foam needs an additional interface condition. The second interface between foam and water is considered immiscible, and moves because of the displacement of the foam front, which is pushing the water forward. This is a difficult situation since both interfaces move through convective forces, but the gas-foam interface is also a transition front.

In order to solve this problem appropriately, we have to split the convection-diffusion problem from the Stefan problem. This last problem is described by an additional Stefan condition that accounts for the gas-foam transition. Alternatively, an enthalpy-like formulation could possibly be defined, in which the interface condition is indirectly treated. This requires more empirical information about the thermal properties of foam in porous media. To our knowledge, this topic has not received much attention yet, and thus, the adaptive grid or hybrid methods described in Section 3.3.2 and Section 3.4, are more suitable to treat this problem at the moment.

The Stefan problem that accounts for an additional water phase can be described by Eq. 3.90, with or without time derivative, and Eq. 3.91, where k/μ is replaced by the total mobility given by the sum of the phase mobilities

$$\lambda = \lambda_w + \lambda_g + \lambda_f. \quad (3.100)$$

The phase mobilities are given by

$$\lambda_g = \frac{k(1 - S_w)^{n_g}}{\mu_g}, \quad (3.101)$$

$$\lambda_f = \frac{k(1 - S_w)^{n_f}}{\mu_f}, \quad (3.102)$$

$$\lambda_w = \frac{k(S_w)^{n_w}}{\mu_w}, \quad (3.103)$$

where S_w is the water saturation, and n_α defines the shape of the mobility functions. Since the gas-foam front $\xi(t)$ moves separately from the foam-water front $\psi(t)$, and its

movement depends only on the water saturation, we are not interested in the gas/foam saturations. The equation for water saturation is derived from mass conservation and described by the hyperbolic conservation law

$$\phi \partial_t S_w = \partial_x (q f_w), \quad (3.104)$$

where f_w is the fractional flow function of water. We will not focus on the solution of this equation here, which is described in detail in Van der Meer *et al.* [25].

To compute the location of the Stefan interface ξ we have to proceed in a similar way as for the simplified model above, except that the diffusion values are now piecewise (non-)linear instead of piecewise constant. The interface condition remains the same. Since the equations for convection and diffusion are split the total velocity of the gas-foam interface can be computed by adding equations for $\xi'(t)$ and the Darcy velocity $q(\xi(t), t)$. More information on so called mushy Stefan problems and problems including fluid flow can be found in [16, 26, 27] among others.

3.6. CONCLUSIONS

In this chapter, we reviewed the application of finite volume methods applied to parabolic equations with one or more discontinuities or strong non-linearities in the diffusion coefficient. This discontinuity often represents a phase interface, where one phase transitions in the other phase. This is a common physical problem, which proves to be complicated to solve numerically. We therefore compared and extended two classes of numerical methods tailored to this problem.

All of these methods have in common that they implicitly or explicitly incorporate interface conditions in the numerical scheme. After reviewing some of the common approaches (enthalpy method and adaptive grid methods) we proposed a combination of these classes that approximates the interface location by interpolation or computing the liquid fraction based on the enthalpy, and adapting the flux terms based on the interface location.

The flux can be adapted by viewing the diffusion coefficient as an impermeable boundary, and using the value left and right of the discontinuity to compute the flux at the grid interfaces around it, instead of averaging over the diffusion coefficient as is usually done. The other approach, indirectly adds an extra grid interface at the approximated interface location and then uses this to update the flux terms surrounding the discontinuity by using weighted averages, where the weights are chosen to be the grid sizes of the new grid cells. The grid cell is only added indirectly, since the flux through the phase interface cancels out in the finite volume scheme.

The downside of these new approaches is that we assume the solution to be almost linear or at least quadratic between two adjacent grid points. However, the jump in the diffusion coefficient causes the solutions of the parabolic model to behave like those of a hyperbolic conservation law, allowing for a shock-like solution if the diffusion coefficient is also degenerate as in [2]. Hence, a linear or quadratic interpolation of the temperature might be far from reality, and cause the approximation to be erroneous. This means that we are possibly reducing the accuracy of the final solutions by making assumptions about the place of the discontinuity. A possible solution would be to include the exact

solution of the local Riemann problem in the numerical scheme [10] and let that determine the place of discontinuity. However, the numerical solution can be shifted, and this might cause the exact discontinuity to be in a different grid block than the numerical one. Presumably, this causes further instabilities. Moreover, the exact solution is only available for a limited number of diffusion coefficients and not at all available in two-dimensional domains. Hence, a better solution would be to use either a higher-order interpolation or to use an approach for which the exact location of discontinuity is of less importance.

In the first numerical example, we solved a standard Stefan problem, with the enthalpy method and a standard finite volume scheme. From this we could conclude that the enthalpy method applied to this problem is suitable for these kinds of problems, since the interface conditions are indirectly included in the enthalpy method, and the method converges to the analytical solution. For lower resolutions the method is quite accurate throughout the domain, but gives a relatively high error around the phase interface and leads to oscillations in time. Increasing the resolution, shows less than linear convergence, but decreases the temporal oscillations occurring around the interface for lower resolutions significantly. The mimetic finite volume methods, on the contrary, did not converge for any of the averaging schemes, because these methods failed to locate the correct phase interface.

In the second example, we looked at the strongly degenerate non-linear heat equation with a discontinuous conductivity. This model was also studied in Chapter 2. The fifth mimetic method we proposed in this chapter performs better than the enthalpy method and also the original mimetic schemes that were introduced in Lipnikov *et al.* [19]. In the third example, we looked at a Darcy-flow model with a phase transition, which resembles the local-equilibrium foam model from Van der Meer *et al.* [2]. Going from this toy model to the original foam model involves coupling the static Darcy-flow model to a hyperbolic saturation equation and letting the relative permeability of the fluids depend on the saturation instead. Since the problem of temporal oscillations only occurs in the parabolic/elliptic equations, the same methods we used here can be applied to this equation when using a sequentially implicit or implicit pressure, explicit saturation solver (IMPES).

Finally, we would like to mention that in view of time constraints, we did not mention the latest developments in numerical methods treating Stefan problems. A popular and suitable method for these kind of problems is the level-set method, which implicitly captures the interface through an artificial equation. For an overview of these methods and another class of phase-field methods, we refer to Javierre *et al.* [21] and Ouazzi *et al.* [28].

REFERENCES

- [1] K. H. Karlsen, N. H. Risebro, and E. B. Storrøsten, *Practical Convergence Rates for Degenerate Parabolic Equations*, in *Innovative Algorithms and Analysis* (Springer, Cham, 2017) pp. 243–263.
- [2] J. M. Van der Meer, J. B. F. M. Kraaijevanger, M. Möller, and J. D. Jansen, *Temporal*

- oscillations in the simulation of foam enhanced oil recovery*, in *Proc. 15th European Conference on Mathematics in Oil Recovery (ECMOR XIV)* (Amsterdam, 2016).
- [3] E. F. Kaasschieter, *Solving the Buckley-Leverett equation with gravity in a heterogeneous porous medium*, *Computational Geosciences* **3**, 23 (1999).
- [4] K. H. Karlsen, *Upwind difference approximations for degenerate parabolic convection-diffusion equations with a discontinuous coefficient*, *IMA Journal of Numerical Analysis* **22**, 623 (2002).
- [5] J.-P. Dias and M. Figueira, *On the approximation of the solutions of the Riemann problem for a discontinuous conservation law*, *Bulletin of the Brazilian Mathematical Society* **36**, 115 (2005).
- [6] K. H. Karlsen, N. H. Risebro, and J. D. Towers, *L1 stability for entropy solutions of nonlinear degenerate parabolic convection-diffusion equations with discontinuous coefficients*, *Skr. K. Nor. Vidensk. Selsk* **3** (2003).
- [7] S. Tveit, *Numerical Methods for Hyperbolic Conservation Laws with a Discontinuous Flux Function*, master thesis, University of Bergen (2011).
- [8] J. D. Towers, *A Difference Scheme for Conservation Laws with a Discontinuous Flux: The Nonconvex Case*, *SIAM Journal on Numerical Analysis* **39**, 1197 (2001).
- [9] N. Pawlitta, *Numerical methods for hyperbolic balance laws with discontinuous flux functions and applications in radiotherapy*, master thesis, Technischen Hochschule Aachen (2011).
- [10] J. K. Wiens, J. M. Stockie, and J. Williams, *Riemann solver for a kinematic wave traffic model with discontinuous flux*, *Journal of Computational Physics* **242**, 1 (2013).
- [11] S. Göttlich and P. Schindler, *Optimal inflow control of production systems with finite buffers*, *Discrete and Continuous Dynamical Systems - Series B* **20**, 107 (2015).
- [12] K. H. Karlsen and J. D. Towers, *Convergence of the Lax-Friedrichs scheme and stability for conservation laws with a discontinuous space-time dependent flux*, *Chinese Annals of Mathematics* **25**, 287 (2004).
- [13] M. Bause and P. Knabner, *Numerical simulation of contaminant biodegradation by higher order methods and adaptive time stepping*, *Comput. Visual. Sci.* **7** (2), 61 (2004).
- [14] J. R. Cannon, *The One-Dimensional Heat Equation* (Cambridge University Press, 1984).
- [15] L. Tao, *A Method for Solving Moving Boundary Problems on JSTOR*, *Siam Journal for Applied Mathematics* **46**, 254 (1986).
- [16] V. R. Voller, *Advances in Numerical Heat Transfer* (CRC Press, 1996).
- [17] J. E. Castillo and G. F. Miranda, *Mimetic discretization methods* (CRC Press, 2013).

- [18] A. Veldman, *Computational Fluid Dynamics*, Tech. Rep. (University of Groningen, 2013).
- [19] K. Lipnikov, G. Manzini, J. D. Moulton, and M. Shashkov, *The mimetic finite difference method for elliptic and parabolic problems with a staggered discretization of diffusion coefficient*, *Journal of Computational Physics* **305**, 111 (2016).
- [20] D. Tarwidi and S. R. Pudjaprasetya, *Godunov Method for Stefan Problems with Enthalpy Formulations*, *East Asian Journal on Applied Mathematics* **3**, 1 (2013).
- [21] E. Javierre, C. Vuik, F. Vermolen, and S. van der Zwaag, *A comparison of numerical models for one-dimensional Stefan problems*, *Journal of Computational and Applied Mathematics* **192**, 445 (2006).
- [22] J. B. F. M. Kraaijevanger, *On the analytical solution of a quasi-linear 1-dimensional heat equation*, Tech. Rep. (Shell, 2011).
- [23] M. Namdar Zanganeh and J. B. F. M. Kraaijevanger, *Adjoint-Based Optimization of a Foam EOR Process*, *SPE journal*, 10 (2012).
- [24] W. R. Rossen, *Numerical Challenges in Foam Simulation : A Review*, in *SPE Annual Technical Conference and Exhibition held in New Orleans*, October (SPE International, New Orleans, 2013).
- [25] J. M. Van der Meer, D. E. A. Van Odyck, P. Wirnsberger, and J. D. Jansen, *High-order Simulation of Foam Enhanced Oil Recovery*, in *Proc. 14th European Conference on Mathematics in Oil Recovery (ECMOR XIV)* (Catania, 2014) pp. 8–11.
- [26] V. Voller and C. Prakash, *A fixed grid numerical modelling methodology for convection-diffusion mushy region phase-change problems*, *International Journal of Heat and Mass Transfer* **30**, 1709 (1987).
- [27] M. Farrokhnejad, A. G. Straatman, and J. T. Wood, *Numerical Simulation of Solidification and Prediction of Mechanical Properties in Magnesium Alloy Casting*, *Metallurgical and Materials Transactions B* **45**, 2357 (2014).
- [28] A. Ouazzi, H. Damanik, J. Hron, and S. Turek, *FEM Techniques for the LCR Reformulation of Viscoelastic Flow Problems*, in *Numerical Mathematics and Advanced Applications 2009* (Springer Berlin Heidelberg, Berlin, Heidelberg, 2010) pp. 747–754.

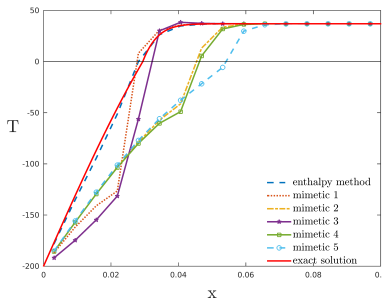
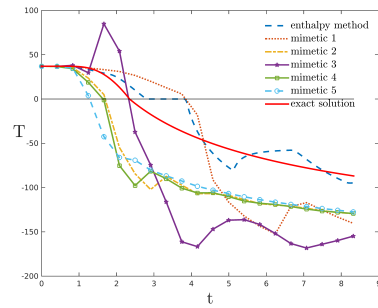
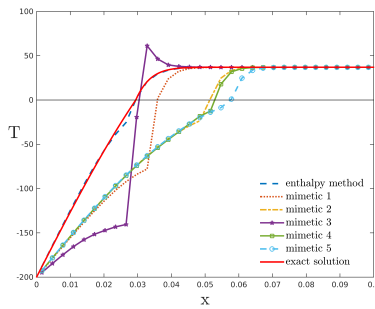
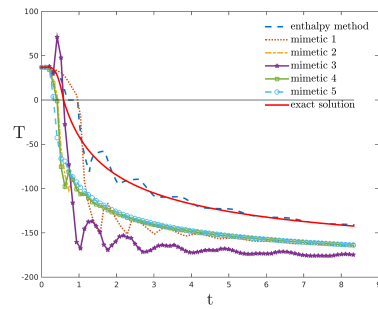
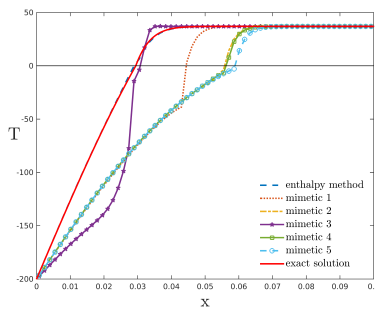
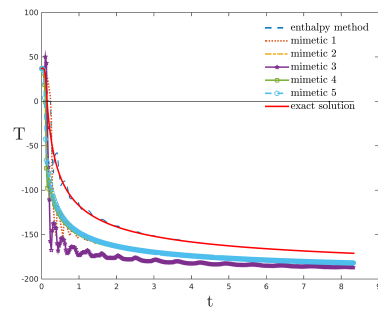
(a) $N = 16$ (b) $N = 16$ (c) $N = 32$ (d) $N = 32$ (e) $N = 64$ (f) $N = 64$

Figure 3.3: Numerical and analytical temperature profiles versus the distance in meters (left) and versus the time in minutes (right) of the heat equation with piecewise constant diffusivity coefficient given by Eq. 3.42, solved by the enthalpy method and the mimetic discretization schemes with a harmonic average in space, and a forward Euler scheme in time.

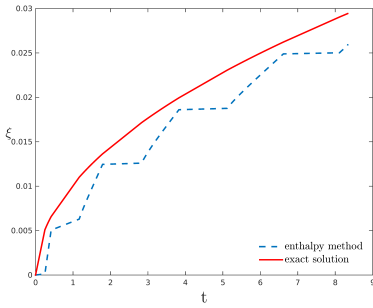
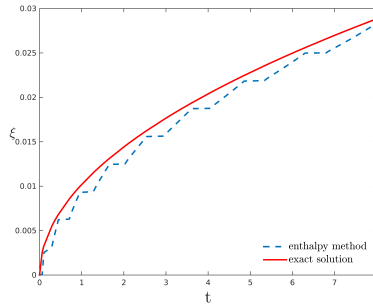
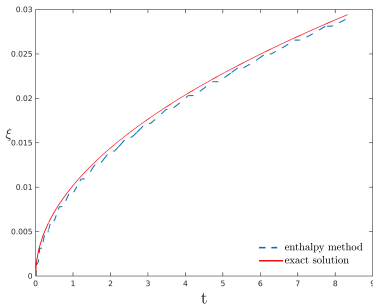
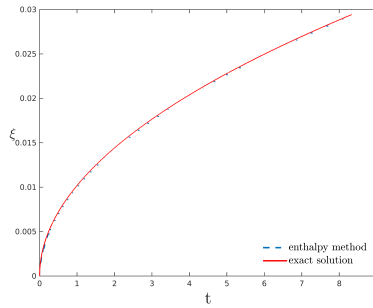
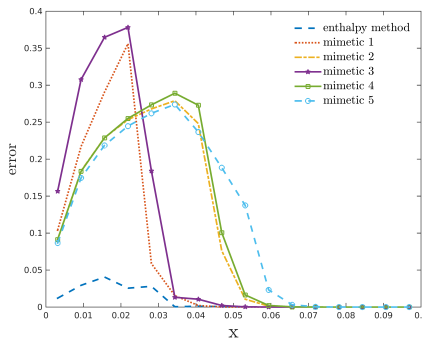
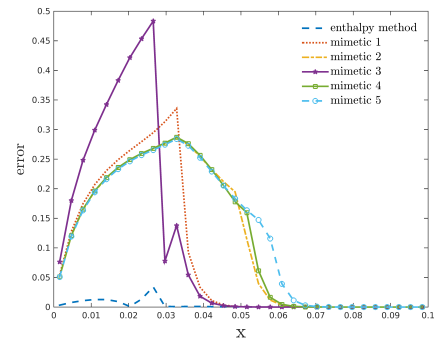
(a) $N = 16$ (b) $N = 32$ (c) $N = 64$ (d) $N = 128$

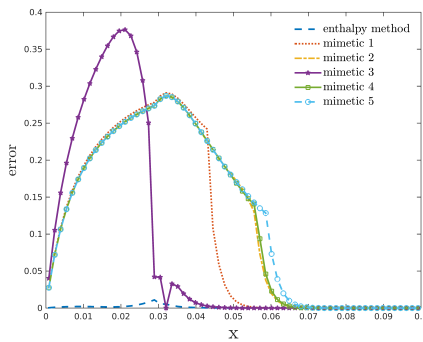
Figure 3.4: Numerical and analytical location of the phase interface versus the time in minutes for the heat equation with piecewise constant diffusivity coefficient given by Eq. 3.42, solved by the enthalpy method with harmonic average and a forward Euler scheme in time.



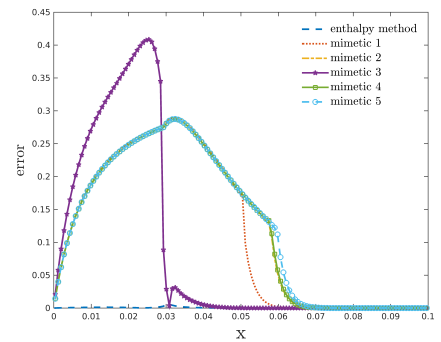
(a) N16



(b) N32

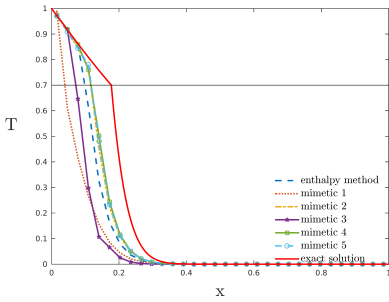


(c) N64

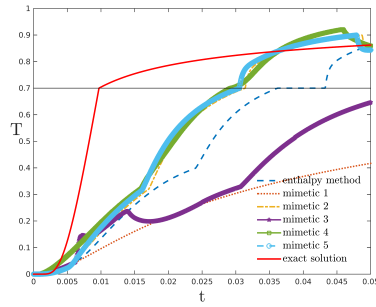


(d) N128

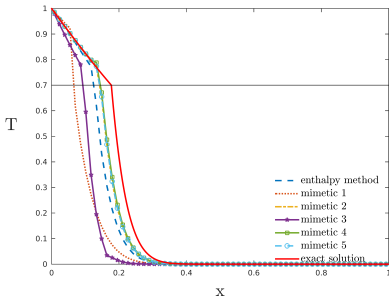
Figure 3.5: Numerical error of the enthalpy method versus the distance in meters for the heat equation with piecewise constant diffusivity coefficient given by Eq. 3.42, solved by the enthalpy method with harmonic average and a forward Euler scheme in time.



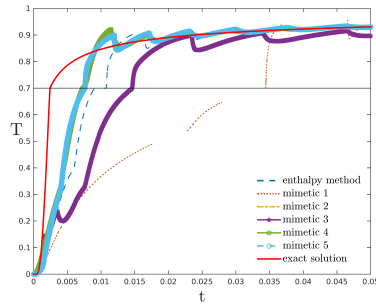
(a) $N = 32$



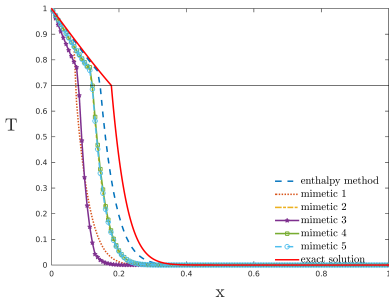
(b) $N = 32$



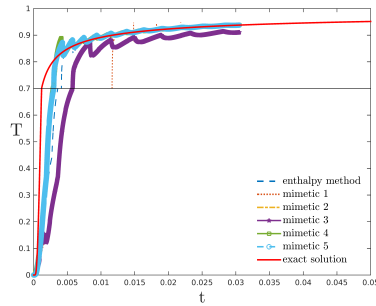
(c) $N = 64$



(d) $N = 64$



(e) $N = 128$



(f) $N = 128$

Figure 3.6: Numerical and analytical temperature profiles versus the distance in meters (left) and versus the time in minutes (right) of the heat equation with a strongly degenerate diffusivity coefficient given by Eq. 3.84, solved by the enthalpy method and the mimetic discretization schemes with harmonic average in space, and a forward Euler scheme in time.

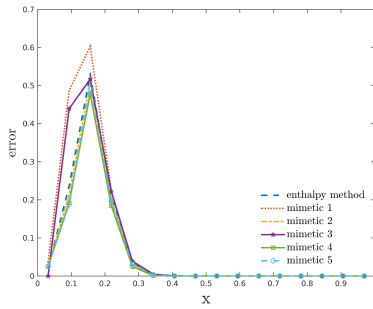
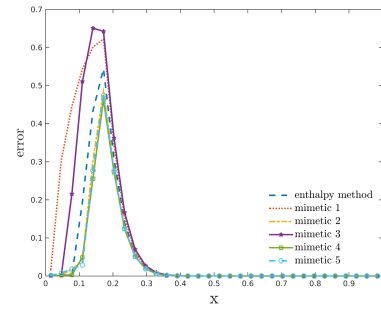
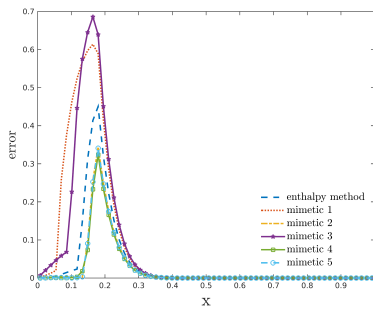
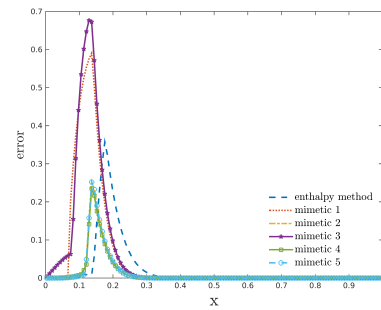
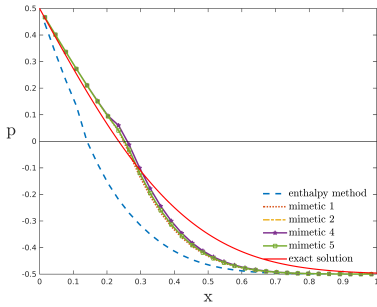
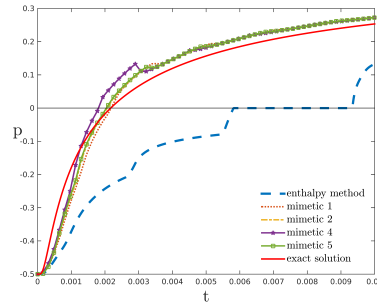
(a) $N = 16$ (b) $N = 32$ (c) $N = 64$ (d) $N = 128$

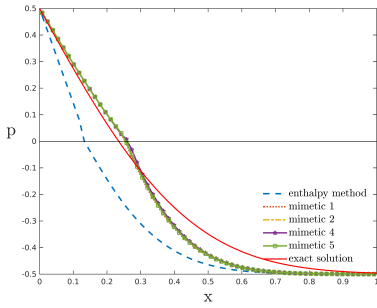
Figure 3.7: Numerical error of the enthalpy method versus the distance in meters for the heat equation with a strongly degenerate diffusivity coefficient given by Eq. 3.84, solved by the enthalpy method with harmonic average and a forward Euler scheme in time.



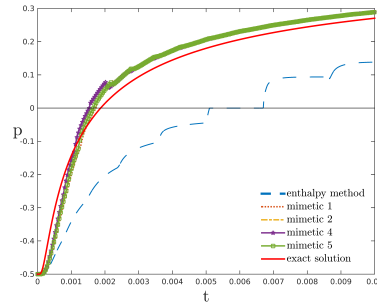
(a) $N = 32$



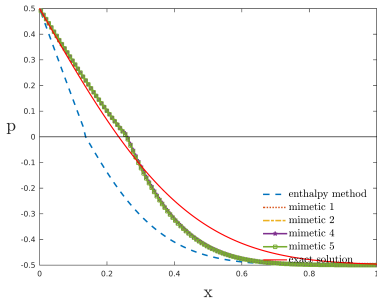
(b) $N = 32$



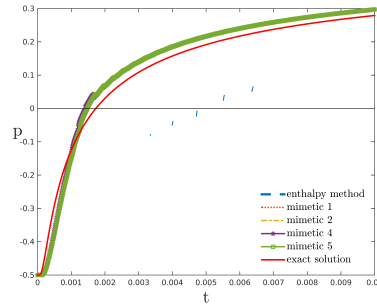
(c) $N = 64$



(d) $N = 64$



(e) $N = 128$



(f) $N = 128$

Figure 3.8: Numerical and analytical temperature profiles versus the distance in meters (left) and versus the time in minutes (right) of the pressure equation with a piecewise constant viscosity given by Eq. 3.92, solved by the enthalpy method and the mimetic discretization schemes with a harmonic average in space, and a forward Euler scheme in time.

4

HIGH-ORDER SIMULATION OF FOAM ENHANCED OIL RECOVERY

The generation of foam will cause a rapid increase of the flux function over a very small saturation scale. Consequently the derivatives of the flux function can become extremely large and impose a severe stability constraint on the numerical scheme [2]. A first-order upwind scheme might be stable but introduces a lot of numerical diffusion around the shock front. In order to improve the accuracy near the foam front we make use of a higher-order total variation diminishing (TVD) scheme that preserves the numerical stability of the solution. Two-dimensional simulations are then performed to examine the conditions under which foam exhibits viscous fingering behavior and gravity override. We use a two-dimensional quarter five-spot setup, where gas is injected at a constant injection rate via a well at the bottom-left corner and water and gas are produced at the same injection rate via the production well at the right-top corner.

Parts of this chapter were prepared for presentation at the 14th European Conference on the Mathematics of Oil Recovery held in Catania, Sicily, Italy, 8 - 11 September 2014 [1].

4.1. INTRODUCTION

Foam was first applied in the oil industry in the late 1950s to decrease gas mobility and hence reduce the undesirable effect of viscous fingering and gravity override [3]. To generate foam in an oil reservoir, usually a mixture of chemicals and water is injected into the reservoir, which together with the injected gas forms a foam. These chemicals make a large contribution to the production costs and therefore the goal is to minimize their amount. To determine the required amount of chemicals for an economically profitable production level, reliable simulations are needed.

There are several models describing foam flow in porous media in use to answer this need. We can roughly distinguish between two classes of foam models: dynamic population balance models, which take into account the strength (bubble density) of the foam, and local equilibrium methods, which incorporate the effect of the foam through a limit function [4]. The first class of models tries to capture the real dynamics of the process, while the second class assumes that there is only one equilibrium in foam strength. Because of the complex nature of the foam the first class has a higher number of degrees of freedom than the second. So from a computational point of view the second class of models is more suitable for performing large-scale reservoir simulations and therefore most useful for our purpose.

Local equilibrium methods are based on conservation laws, conserving the phases present (usually gas, water and oil), while it is assumed that the surfactant is dissolved in either the gas or the water phase. As soon as the gas comes in contact with a sufficient amount of water and surfactant a foam is generated. The foam will cause a rapid decrease of the gas mobility, because it captures the gas in bubbles that are separated by liquid films (lamellae) between the pore walls [2]. The water mobility is not influenced by foam in these models. Hence the mobility ratio between gas and water is reduced, which will increase the time that the injected gas needs to reach the production well (breakthrough time).

We describe the foam process by an immiscible two-phase flow model where gas is injected in a porous medium filled with a mixture of water and surfactants. The change from pure gas into foam is incorporated in the model through a reduction in the gas mobility. Hence the two-phase flow description of the flow stays intact. Since the total pressure drop in the reservoir is small both fluids can be considered incompressible [5]. As an example we use a two-dimensional quarter five-spot setup, where gas is injected at a constant injection rate via a well at the bottom-left corner and water and gas are produced at the same injection rate via the production well at the right-top corner.

The generation of foam will cause a rapid increase of the flux function over a very small saturation scale. Consequently the derivatives of the flux function can become extremely large and impose a severe stability constraint on the numerical scheme [2]. A first-order upwind scheme might be stable but introduces a lot of numerical diffusion around the shock front. In order to improve the accuracy near the foam front we make use of a higher-order total variation diminishing (TVD) scheme that preserves the numerical stability of the solution. Two-dimensional simulations are then performed to examine the conditions under which foam exhibits viscous fingering behavior and gravity override.

4.2. MATHEMATICAL MODEL

4.2.1. STATE VARIABLES AND PARAMETERS

The variables involved are the Darcy velocity \mathbf{u} , the pressure p , the density ρ and the viscosity μ of the fluids present. Because we deal with a porous medium we express the amount of fluid in terms of the porosity ϕ of the medium, defined by the ratio of the pore volume to the total volume, which is assumed constant. The phase saturation S , is defined as the volume fraction of the pore space occupied by a fluid phase, so that both phases make up for the total volume. The relative permeability k_r depends on specific properties of the fluid and the rock and is defined as a function of saturation. The absolute permeability k depends solely on the properties of the rock and is a function of the spatial variables only. Furthermore z is the depth, γ the gravitational acceleration and ∇ denotes the gradient operator. To denote the partial derivative of a variable q in time we write $\frac{\partial q}{\partial t}$. The divergence of a vector \mathbf{v} is denoted by $\nabla \cdot \mathbf{v} = (\partial_x, \partial_y) \cdot \mathbf{v}$.

4.2.2. CONSERVATION LAW

Starting from mass conservation, we can define a basic model for the gas saturation S_g ,

$$\phi \frac{\partial S_g}{\partial t} = -\nabla \cdot (f_g \mathbf{u} + \lambda_w f_g \Delta \rho \gamma \nabla z) + q_g, \quad (4.1)$$

where f_g is the gas fractional flow function, q_g the gas flow rate, $\Delta \rho$ the density difference between water and gas, and $\mathbf{u} = u_w + u_g$ is the total Darcy velocity that follows from Darcy's law for the fluid phase velocity,

$$u_\alpha = -\lambda (\nabla p_\alpha + \rho_\alpha \gamma \nabla z), \quad (4.2)$$

with the total mobility $\lambda = \lambda(S)$ given by the sum of the phase mobilities

$$\lambda_\alpha = k \frac{k_{r\alpha}(S_\alpha)}{\mu_\alpha}. \quad (4.3)$$

The fractional flow function is defined as the fraction of the phase mobility and the total mobility. Since the fluids are considered incompressible it follows that

$$\nabla \cdot \mathbf{u} = q, \quad (4.4)$$

where q is the total flow rate of water and gas.

4.2.3. FOAM MODEL

If gas comes into contact with a sufficient amount of water and surfactants, foam will form. This will cause a rapid decrease in the gas mobility, which can be modeled by decreasing the relative gas permeability function by a mobility reduction factor f_{mr} ,

$$k_{rg}^f := \frac{k_{rg}^0}{f_{mr}}, \quad f_{mr} = 1 + R \cdot F_w \cdot F_s, \quad (4.5)$$

where k_{rg}^0 is the relative gas permeability of the gas in its original state, R is a constant that accounts for the maximum flow resistance of the foam, and F_w and F_s are functions

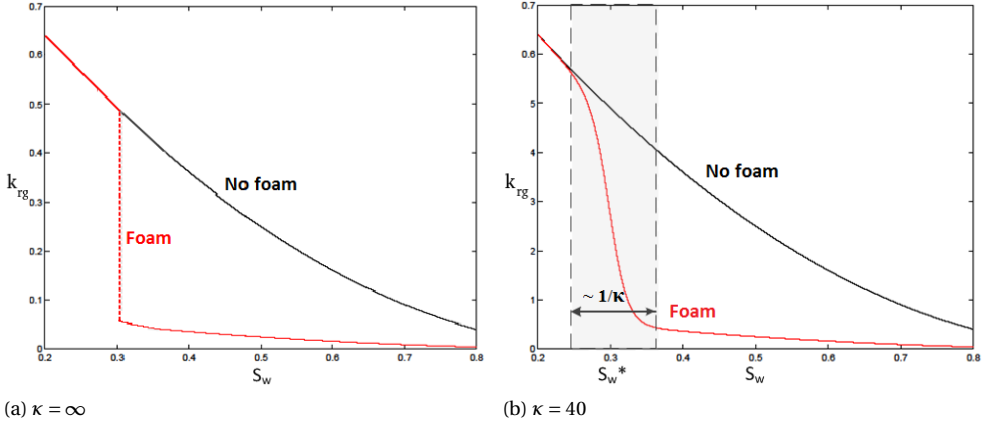


Figure 4.1: Relative permeability function for a model with and without foam for $S_w^* = 0.3$. The sudden transition due to foam for $R = 10$ is approximated by a continuous line at the right with $\kappa = 40$.

that describe the sensitivity of the foam to water saturation and surfactant concentration, respectively [6]. We assume that the surfactant concentration is the same everywhere so that $F_s = 1$. For F_w we use the STARS foam model used in Leeffink *et al.* [5],

$$F_w = 0.5 + \frac{\arctan(\kappa(S_w - S_w^*))}{\pi}, \quad (4.6)$$

where S_w^* is the least amount of water that is needed to form a foam. Since a sudden jump in the mobility of the gas at S_w^* will cause numerical problems [2], this jump in mobility is approximated by a continuous arctangent function, so that it is smeared over a width that scales with $1/\kappa$. In Figure 4.1 the relative permeability function described here is shown. The flux function and its derivative for the scaled parameters are shown in Figure 4.2.

4.2.4. SCALING THE MODEL

To reduce the number of parameters we scale the model given by equations 4.1 and 4.2 in a similar way as done by Riaz and Tchelepi [7]. If we let W be a characteristic length scale of the model, and U a characteristic velocity scale we can scale the variables as

follows

$$z = \overline{W}z^*, \quad (4.7)$$

$$\nabla = \frac{\nabla^*}{\overline{W}}, \quad (4.8)$$

$$\mathbf{u} = U\mathbf{u}^*, \quad (4.9)$$

$$t = \frac{\phi W(1 - S_{wc} - S_{gr})}{U} t^*, \quad (4.10)$$

$$p = \frac{\mu U W}{k} p^*, \quad (4.11)$$

$$q = \frac{U}{\overline{W}} q^*, \quad (4.12)$$

where the superscript $*$ denotes a non-dimensional variable. The relative permeability functions are scaled by their endpoint relative permeabilities, i.e. the relative permeability of the residual water and gas saturation, $k_{rwe} = k_{rw}(S_{gr})$ and $k_{rge} = k_{rg}(1 - S_{wc})$, respectively. The gas saturation is normalized by $S_g^* = \frac{(S_g - S_{gr})}{(1 - S_{wc} - S_{gr})}$. Substituting all of these variables into the dimensional model leads to a non-dimensionalised system of the form,

$$\frac{\partial S_g^*}{\partial t^*} = -\nabla^* \cdot \left(\frac{k_{rg}^* M}{\lambda^*} \mathbf{u}^* + \frac{k_{rw}^* k_{rg}^*}{\lambda^*} G \nabla^* z^* \right) + q_g^*, \quad (4.13)$$

$$\mathbf{u}^* = -\lambda^* \nabla^* \bar{p} + G k_{rg}^* \nabla^* z^*, \quad (4.14)$$

$$\nabla^* \cdot \mathbf{u}^* = q^*, \quad (4.15)$$

where

$$\nabla^* \bar{p} = \nabla^* p_w^* + \frac{\rho_w g k}{\mu_w U} \nabla^* z^*, \quad (4.16)$$

and $\lambda^* = M k_{rg}^* + k_{rw}^*$ is the dimensionless mobility function. The variables M and G denote the dimensionless mobility ratio and gravity number respectively, which are given by

$$M = \frac{\mu_w}{\mu_g} \frac{k_{rge}}{k_{rwe}}, \quad (4.17)$$

$$G = \frac{k \Delta \rho g}{\mu_g U}. \quad (4.18)$$

$$(4.19)$$

These two variables together with the dimensionless foam parameters R , κ and S_w^* , dimensionless injection rate I^* and porosity ϕ , now determine the entire behavior of the fluids for a certain initial boundary value problem. In the rest of the article we will drop the star superscript for readability and define S to be S_g .

4.3. NUMERICAL METHODS

The two-phase foam model described in the last section consists of a hyperbolic equation for the saturation 4.13 and an elliptic equation for the pressure 4.15. We solve this

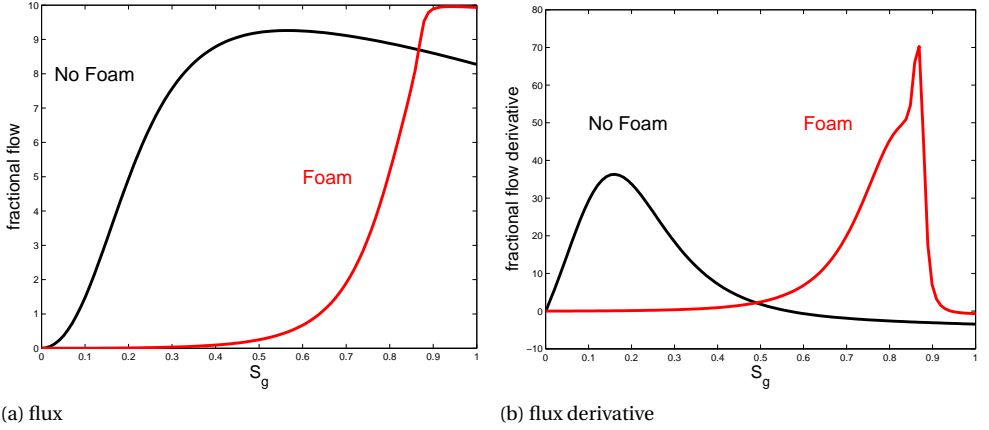


Figure 4.2: Flux function and derivative for the foam model compared with the Buckley-Leverett flux for $S_w^* = 0.13$, $\kappa = 100$, $R = 1000$, $M = 10$ and $G = 2$.

system by the implicit pressure explicit saturation (IMPES) method, which is designed for this kind of hyperbolic-elliptic problems because it takes into account the different nature of the equations.

We use a structured staggered grid representation of the problem with no-flow boundary conditions everywhere, as shown in Figure 4.3. The pressure is defined up to an additive constant, so to make sure the system is well-posed the pressure is prescribed in one of the grid cells. The no-flow boundaries are implemented by introducing additional layers of ghost cells around the boundaries. These ghost cells take the same value as the cells inside the boundary so that the net flux across the boundary is zero, i.e. the state variables saturation and pressure defined in the center of a grid cell are equal to the state variables in their corresponding ghost cells. Since we use a staggered grid for the state variables, the Cartesian components of the velocity, u and v , are not defined in the cell centers, but at the vertical and horizontal interfaces respectively. To ensure no flow through the boundaries these values are reflected through the boundary. The wells are modeled in the center of each grid cell so that the velocities at the well do not affect the boundary conditions. We represent the wells either as point-sources or as circular wells that are extended over more grid cells.

By using operator splitting, as described in Hvistendahl Karlsen *et al.* [8], we can split the saturation equation into a hyperbolic conservation law and an ordinary differential equation (ODE) for the mass flow rate. They are solved sequentially using a second-order Strang-splitting scheme, which preserves the symmetry of the operator.

4.3.1. HYPERBOLIC EQUATION

The hyperbolic equation

$$\phi \frac{\partial S}{\partial t} = -\nabla \cdot \left(\frac{k_{rg} M}{\lambda} \mathbf{u} + \frac{k_{rw} k_{rg}}{\lambda} G \nabla z \right) \quad (4.20)$$

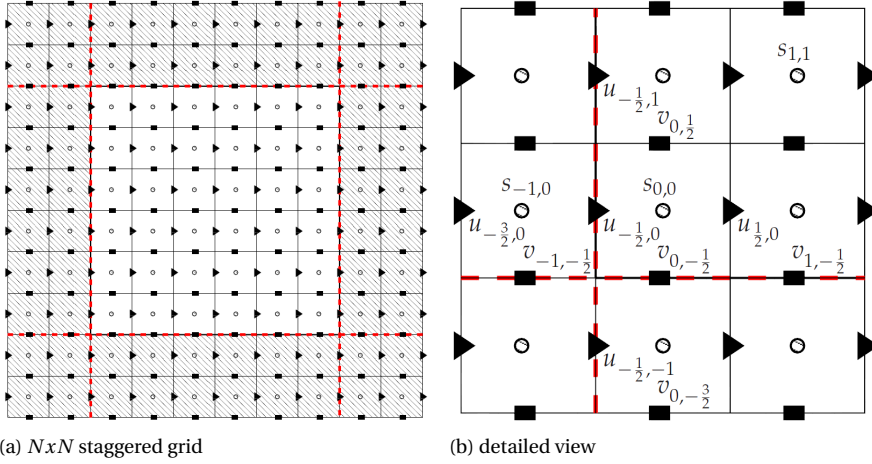


Figure 4.3: Staggered grid with two layers of ghost cells. The red dotted layers represent no-flow boundaries and the black squares and arrows the velocities in the x and y direction, respectively (from Wirsberger [9]).

is solved with a second order MUSCL scheme, which is a total variation diminishing finite volume method reconstructed from the first order Godunov's method [10]. The TVD property prevents instabilities to occur that are due to the numerical method. In other words a TVD scheme is monotonicity preserving if the Courant-Friedrichs-Levy (CFL) condition on the time step is satisfied [10]. Because of the sharp transition in the flux function when foam is generated this condition is very restrictive for the foam model, especially for large values of κ .

4.3.2. SOURCE TERM

The ODE is given by

$$\phi \frac{\partial S}{\partial t} = \begin{cases} qS_{inj}, & \text{if } q > 0, \\ qS_g, & \text{if } q < 0. \end{cases} \quad (4.21)$$

In both wells we prescribe the volume flow rate, so that $q = I/V_{well}$, where I is a constant injection rate and V_{well} is the volume of the well. The injected fluid saturation S_{inj} is constant and the produced fluid saturation depends on the saturation present at the production well. The ODE is solved by the second order trapezoidal rule, which is A-stable and therefore suitable for stiff ordinary differential equations [11]. The size of the time step of an A-stable method does not suffer from stringent restrictions and the choice only depends on the desired accuracy, but is limited because we cannot exceed the saturation range $0 \leq S \leq 1$. Consequently an additional restriction on the time step has to be made on top of the CFL condition. We incorporate this by restricting the total variation of the saturation in time for equation 4.13, so that

$$\Delta t \leq \frac{\Delta S_{max} h}{\left(\frac{\partial S^{n+1}}{\partial t}\right)_{max}} \approx \frac{\Delta S_{max} h}{\lambda_{max} \Delta S_{max} + |q|_{max} h / \phi}, \quad (4.22)$$

where ΔS_{\max} is the maximum variation allowed in the saturation per time step, λ_{\max} is the maximum wave speed and h is the grid size. Consequently, if the source term is zero everywhere, the maximum time step boils down to the CFL condition with a CFL number $C_{CFL} = 1$. To prevent unstable solutions the maximum variation in the saturation ΔS_{\max} should be of the order 10^{-3} according to Chen *et al.* [12]. The restriction caused by the source term can therefore cause the time step to decrease by a significant amount in a foam free setup with $|q|_{\max} h > \lambda_{\max} \Delta S_{\max}$. However, if foam is added, this will cause a strong restriction on the time step for large κ due to the CFL condition, and hence the restriction caused by the source term will be of minor importance.

4.3.3. ELLIPTIC EQUATION

For the elliptic equation 4.15 we use a multi-grid linear solver that combines a five-point stencil with a nine-point stencil that is rotated by 45 degrees in order to reduce the grid orientation effect [9]. The five-point stencil accounts for the unrotated coefficients and is combined with a nine-point stencil that accounts for the rotated coefficients and is projected back onto the original grid. The domain is parallelized by a Multi Processor Interface (MPI) using the Parallel High Performance Preconditioners (HYPRE) library [13] in order to speed up the computations, since roughly 73% of the simulation time is spent on the pressure solver for this model [14].

4.4. RESULTS

We will study the constant injection of pure gas in a water-surfactant filled reservoir for two test cases. In the first case the reservoir is vertical, which causes the gas to flow upwards due to a gravity force and in the second case the reservoir is horizontal and gravity does not play a role. We will take a close look at the behavior of the numerical solutions around the foam front, and compare them to simulation results for the same model without foam (gas-flooding). We use the Brooks-Corey relative permeability functions for gas and water, given by

$$k_{wr}^0 = k_{rwe} \left(\frac{S_w - S_{wc}}{1 - S_{wc} - S_{gr}} \right)^{n_w}, k_{rg}^0 = k_{rge} \left(\frac{S_g - S_{gr}}{1 - S_{wc} - S_{gr}} \right)^{n_g}, \quad (4.23)$$

where k_{rwe} and k_{rge} are the endpoint relative permeabilities, S_{wc} and S_{gr} the residual water and gas saturation and n_w and n_g power coefficients that depend on the rock type. The foam parameters we use are similar to those in the paper of Leefink *et al.* [5] and are listed in Table 4.1. The dimensionless mobility ratio and gravity number are varied for the different simulations, as well as the grid resolution, error tolerance, end time and the absolute permeability. The other parameters are taken constant (see Table 4.1).

4.4.1. CASE 1: GRAVITY OVERRIDE

Gravity override occurs when the lighter fluid (in this case gas) separates from the heavier fluid due to gravitational forces. This undesirable event diminishes the sweep area of the reservoir and should therefore be avoided. As shown in Figure 4.4, the model with foam is less inclined to gravity override than the gas-flooding model. This is caused by

parameter	value	unit	explanation
α	$\pi/2$	radians	tilting angle
ϵ	-	-	error tolerance for the linear solver
G	-	-	gravity number
k	10^{-9}	m^2	absolute permeability (mean value)
κ	$3.4 \cdot 10^4$	-	steepness parameter foam transition
I	$1.840 \cdot 10^{-4}$	$\text{m}^3 \text{s}^{-1}$	injection volume flow rate gas
k_{rge}	0.8649	-	endpoint relative permeability gas
k_{rwe}	0.6822	-	endpoint relative permeability water
L	10^3	m	length of reservoir
M	-	-	dimensionless mobility ratio
μ_g	$2 \cdot 10^{-5}$	Pa s	gas viscosity
μ_w	10^{-3}	Pa s	water viscosity
N	-	-	resolution of reservoir
n_g	2	-	power coefficient of gas
n_w	3.5	-	power coefficient of water
ϕ	0.3	-	porosity
R	10^5	-	maximum resistance foam to flow
ρ_g	1	kg m^{-3}	gas density
ρ_w	10^3	kg m^{-3}	water density
$S_{g,r}$	0.0	-	residual gas saturation
$S_{g,inj}$	1.0	-	injected gas saturation
$S_{w,c}$	0.0	-	critical water saturation
S_w^*	0.13	-	critical water saturation
U	1	m s^{-1}	characteristic velocity

Table 4.1: Simulation parameters, a value of – means that the parameter is not constant.

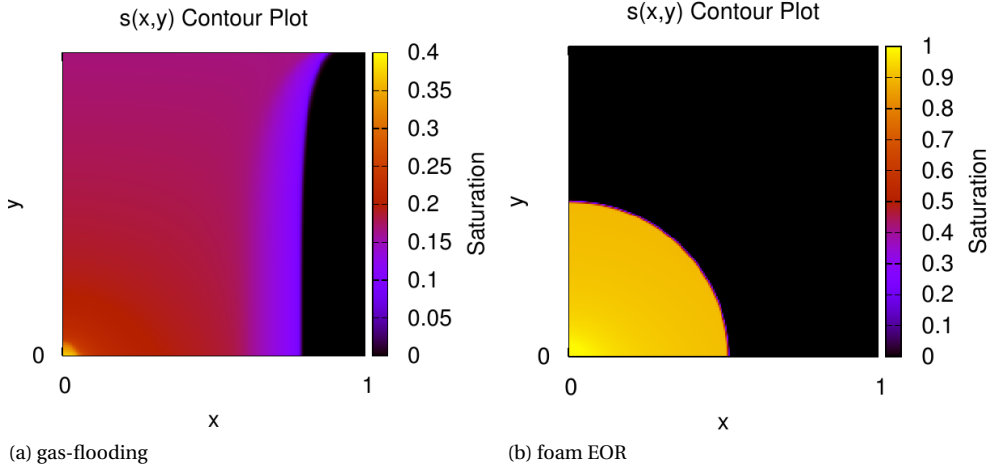


Figure 4.4: Gas saturation contour plots for a vertical reservoir with $t = 100$, $N = 200$, $M = 100$, $G = 2$, $k = 10^{-9}$ and $\epsilon = 10^{-6}$.

the sharp decrease in mobility, so that gravity has a smaller effect on the flux, which follows from the convex-hull construction of the flux as shown in Figure 4.2a.

4.4.2. CASE 2: VISCOUS FINGERING

In order to see viscous fingering a high spatial resolution is needed. We opt for a resolution of 800 grid cells in both directions. Because of the severe CFL constraint on the time step for the foam model this means we need a time step that is several orders of magnitude smaller than the time step for the same simulation without foam. Upon that it takes much longer for the foam front to reach the production well as for the gas front because the front is moving much slower through the reservoir due to the decreased gas mobility. Furthermore we introduce a random heterogeneity in the reservoir to trigger the instabilities so that they show up at an earlier stage of the simulation, to save simulation time. The absolute permeability is generated from a normal distribution with mean 10^{-9} and a standard deviation of ten percent. In Figure 4.5 and Figure 4.6 the results for these simulations are shown. There is no viscous fingering visible for the foam model, while small fingers appear for the gas-flooding simulation. The hypothesis is that these fingers are suppressed by the sharp transition between foam and water.

In Figure 4.7 the effect of the foam on the production of water is shown. Since the breakthrough time of the gas front is increased due to foam, the cumulative water production grows over a longer time range and so the total production is much larger for the foam model. The gas-flooding model is mainly producing gas after the breakthrough time is reached. We note that our model does not contain oil, and that the increased water production is therefore merely an illustration of the positive effect of foam on the gas breakthrough time.

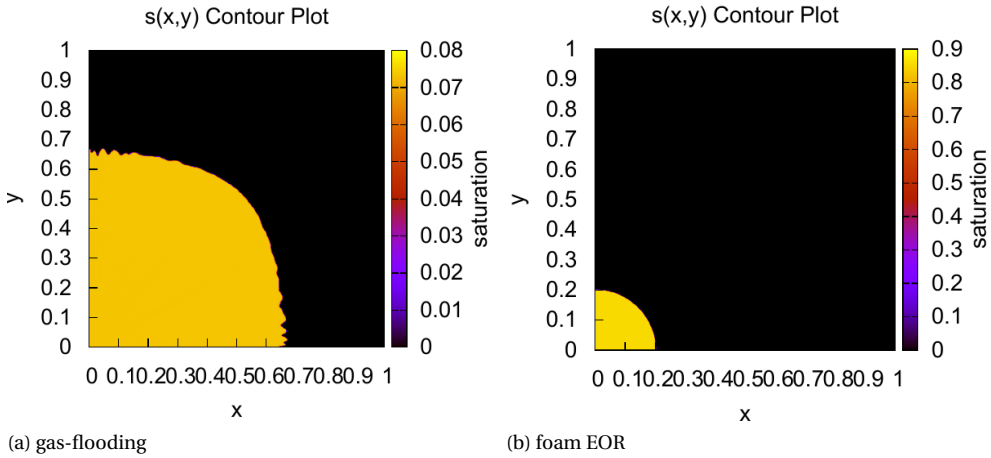


Figure 4.5: Gas saturation contour plots for a horizontal reservoir with $t = 150$, $N = 800$, $M = 50$, $G = 0$, $k = 10^{-9}$ and $\epsilon = 10^{-10}$.

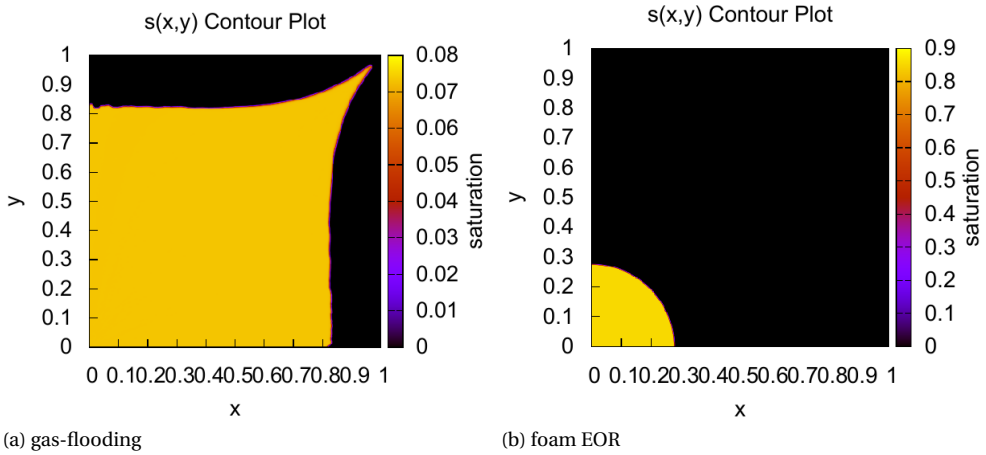


Figure 4.6: Gas saturation contour plots for a horizontal reservoir with $t = 280$, $N = 400$, $M = 50$, $G = 0$, $k = 10^{-9}$ and $\epsilon = 10^{-10}$.

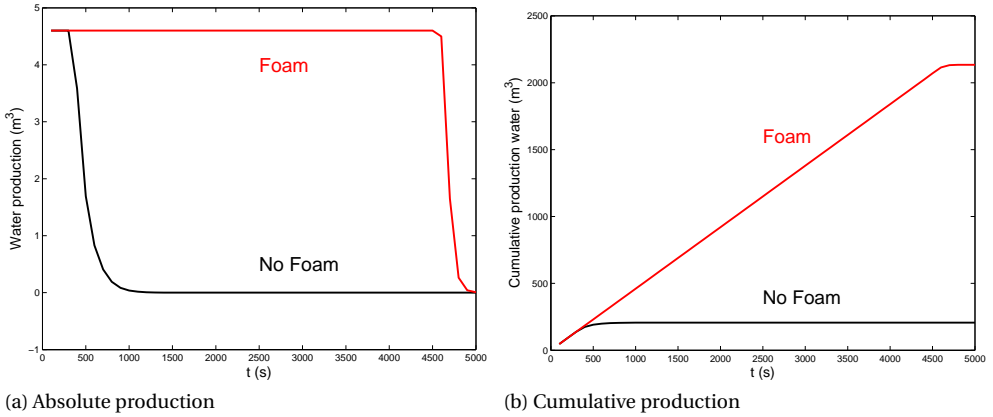


Figure 4.7: Water production for a horizontal reservoir with $N = 30$, $M = 50$, $G = 0$, $k = 10^{-9}$ and $\epsilon = 10^{-6}$.

4.5. CONCLUSIONS

The results show that foam has an effect on the shock saturation. In comparison with gas-flooding the foam solution has a much lower shock saturation for the water phase and therefore a sharper shock front. By closer examination the shock saturation is almost equal to the critical saturation. This also follows from the convex-hull construction of the flux function with foam.

It turns out that foam has a significant effect on the behavior of the gas front. As expected the simulations with foam suffer less from gravity override and viscous fingering than the simulations without foam. This leads to a better sweep of the reservoir and a much lower breakthrough time. Although these advantages of foam are already well-known in the reservoir engineering community, to our knowledge these phenomena have not yet been studied using higher-order schemes.

Ongoing work includes a quantitative analysis of the instabilities at the gas front with and without foam. In order to do this we need to increase the grid resolution, as well as the order of the numerical methods. To verify our results we plan to compare them with real-world reservoir data.

4.6. ACKNOWLEDGEMENTS

The first author would like to thank Dr. Nikiforakis for providing the opportunity to visit the Centre for Scientific Computing (Cavendish Laboratory, University of Cambridge) and to the other staff and students at the Centre for Scientific Computing for their help and hospitality. Furthermore, we thank Bill Rossen of Delft University of Technology for useful discussions.

REFERENCES

- [1] J. M. Van der Meer, D. E. A. Van Odyck, P. Wirnsberger, and J. D. Jansen, *High-order Simulation of Foam Enhanced Oil Recovery*, in *Proc. 14th European Conference on*

- Mathematics in Oil Recovery (ECMOR XIV)* (Catania, 2014) pp. 8–11.
- [2] W. R. Rossen, *Numerical Challenges in Foam Simulation : A Review*, in *SPE Annual Technical Conference and Exhibition held in New Orleans*, October (SPE International, New Orleans, 2013).
- [3] A. N. Fried, *United States Bureau of Mines Bulletin 5866*, Tech. Rep. (Bureau of Mines, 1961).
- [4] E. Ashoori, *Foam for Enhanced Oil Recovery: Modeling and Analytical Solutions*, Ph.D. thesis, Delft University of Technology (2012).
- [5] T. N. Leeftink, C. A. Latooij, and W. R. Rossen, *Injectivity errors in simulation of foam EOR*, *Journal of Petroleum Science and Engineering* **126**, 26 (2015).
- [6] M. Namdar Zanganeh, *Simulation and optimization of foam EOR processes*, Ph.D. thesis, Delft University of Technology (2011).
- [7] A. Riaz and H. A. Tchelepi, *Stability of two-phase vertical flow in homogeneous porous media*, *Physics of Fluids* **19**, 072103 (2007).
- [8] K. Hvistendahl Karlsen, K. A. Lie, J. Natvig, H. Nordhaug, and H. Dahle, *Operator Splitting Methods for Systems of Convection-Diffusion Equations: Nonlinear Error Mechanisms and Correction Strategies*, *Journal of Computational Physics* **173**, 636 (2001).
- [9] P. Wirnsberger, *The grid orientation effect in miscible displacement*, Mphil dissertation, University of Cambridge (2012).
- [10] E. F. Toro, *Riemann Solvers and Numerical Methods for Fluid Dynamics*, 3rd ed. (Springer Berlin / Heidelberg, 2009) Chap. 0, p. 540.
- [11] G. G. Dahlquist, *A special stability problem for linear multistep methods*, *BIT Numerical Mathematics* **3** (1), 27 (1963).
- [12] Z. Chen, G. Huan, and Y. Ma, *Computational methods for multiphase flows in porous media*, 1st ed. (SIAM, 2006).
- [13] R. D. Falgout and U. Meier Yang, *Hypr: a Library of High Performance Preconditioners*, in *Preconditioners, Lecture Notes in Computer Science* (ICCS, 2002) pp. 632–641.
- [14] I. Yahya Afiff, *Reservoir simulation of foam flow using Kepler GPU*, Msc. thesis, Delft University of Technology (2014).

5

THE STABILITY CHARACTERISTICS OF FOAM FLOW IN POROUS MEDIA

Accurate field-scale simulations of foam enhanced oil recovery are challenging, due to the sharp transition between gas and foam. Hence, unpredictable numerical and physical behavior is often observed, casting doubt on the validity of the simulation results. In this paper a thorough stability analysis of the foam model is presented, to validate the simulation results and lay a foundation for a tailor-made solver, which can both handle large-scale reservoir simulations and accurately resolve front instabilities. We study the effect of a strongly non-monotonous total mobility function arising from foam models on the stability characteristics of the flow. To this end, we generalize the linear stability analysis of Riaz and Tchelepi (2004-2007) to nearly discontinuous relative permeability functions, and compare the results with those of highly accurate numerical simulations. In addition, we present a qualitative analysis of the effect of different reservoir and fluid properties on the foam fingering behavior. In particular, we consider the effect of heterogeneity of the reservoir, injection rates, and foam quality. Relative permeability functions play an important role in the onset of fingering behavior of the injected fluid [2]. Hence, we can deduce that stability properties are highly dependent on the non-linearity of the foam transition. The foam-water interface is governed by a very small total mobility ratio, implying a stable front. The transition between gas and foam, however, exhibits a huge total mobility ratio, leading to instabilities in the form of viscous fingering. This implies that there is an unstable pattern behind the front. An indication of this behavior was shown in Farajzadeh et al. [3] for a similar foam model, but the authors did not provide a satisfying explanation for the cause of these instabilities. Here we closely study the influence of the foam on instabilities at and behind the front, and are able to predict the flow stability for different foam qualities. We deduce that instabilities are indeed able to grow behind the front, but are later absorbed by the expanding wave. The stability analysis, validated by

Parts of this chapter were prepared for presentation at the SPE Reservoir Simulation Conference held in Montgomery, Texas, USA, 20-22 Feb 2017 [1].

numerical simulations, provides valuable insights about the important scales and wavelengths of the foam model. In this way we remove the ambiguity regarding the effect of grid resolution on the convergence of the solutions. This insight forms an essential step towards the design of a suitable computational solver that captures all the appropriate scales, while retaining computational efficiency.

5.1. INTRODUCTION

Foam enhanced oil recovery (EOR) is applied to increase oil production by reducing disadvantageous effects like channeling, viscous fingering, and gravity override. When gas is injected in a porous medium containing a surfactant solution, a foam front forms. The foam captures the gas in bubbles and reduces its mobility. The effectiveness of the process depends on the stability of the created foam controlled by the magnitude of the capillary pressure. It has been observed that foam experiences a significant coalescence when the capillary pressure approaches the so-called limiting capillary pressure, P_c^* [4, 5]. In other words, when the water saturation drops below a critical value, called the limiting water saturation S_w^* , foam becomes too dry and collapses. The mobility of the gas, which is the ratio of the relative gas permeability and the gas viscosity, therefore contains a sharp transition around the limiting water saturation.

To reduce the operational risks associated with injectivity decline because of generation of very strong foams, material compatibility and well integrity, it has been suggested to inject gas and surfactant solution in an alternating mode, i.e., a slug (fraction of the pore volume) of surfactant followed by a slug of gas. Upon mixing of the gas and the surfactant solution in the pores, foam lamellae will form in-situ. Behind the foam front, gas reduces the water saturation to saturations close to the limiting water saturation and therefore with gradual or abrupt collapse of foam, the gas mobility increases from the foam front towards the injection well. The instabilities that might occur within this bank (between the front and the injection point) have been the subject of a recent study [3], which suggested that the fingering has physical origin and is not due to numerical artifacts discussed in the paper. This phenomenon, the extent of which depends mainly on the properties of the foam behind the front, may not be visible in simulations with poor grid resolutions.

Because of this aspect of foam, accurate field-scale simulations are challenging. Hence, unpredictable numerical and physical behavior is often observed, casting doubt on the validity of the simulation results [3, 6–9]. In this chapter a thorough stability analysis of an implicit texture (local equilibrium) foam model is presented, to validate the simulation results and lay a foundation for a tailor-made solver, which can both handle large-scale reservoir simulations and accurately resolve front instabilities. We study the effect of a strongly non-monotonous total mobility function, arising from foam models, on the stability characteristics of the flow. To this end, we generalize the linear stability analysis of Yortsos and Hickernell [10], Riaz *et al.* [11], Riaz and Tchelepi [2, 12, 13] and Meulenbroek *et al.* [14] to nearly discontinuous relative permeability functions, and compare the results with those of highly accurate numerical simulations.

In this earlier work on the stability of immiscible two-phase flow in porous media, a linear stability analysis was performed for the quasi-linearized model. This was done in a transformed coordinate frame that moves along with the front. By using a perturbation theory that exploits a normal mode decomposition strategy, it was shown that the onset of the instabilities of the displacing fluid is governed by the total mobility ratio across the shock (as opposed to the mobility ratio over the entire transition region). The shape of the relative permeability curves plays an important role at this stage [2].

We therefore propose to apply the perturbation theory to the foam model, in order to investigate the effect of the abrupt changes in the gas relative permeability on the stabil-

ity of the foam front. We are especially interested in the effect of this particular relative permeability function on the stability characteristics of the model. The function form differs from the ones described by Riaz and Tchelepi [2], because it allows for discontinuities and the corresponding total mobility function is non-monotonic, and can have an unfavorable shock-mobility ratio.

The foam-water interface has usually a very small total mobility ratio, leading to a stable front. The subsequent transition front, where foam turns into gas, exhibits a large total mobility ratio. This implies that there is an unstable pattern behind the front, which can be detected by highly-accurate numerical simulations. An indication of this behavior was shown in Farajzadeh *et al.* [3] for a two-phase incompressible immiscible foam model.

The question is to which extent the strong non-linearities in the foam model can be described by a linear stability analysis. To answer this, we compare the linear stability results with accurate numerical simulations, where we approximate several properties, like interfacial length, wave number and maximum growth number. To solve the system of saturation and pressure equations we apply a semi-implicit finite volume method. To minimize numerical diffusion around the front we use a second-order monotonic upstream-centered scheme for conservation laws (MUSCL) for the hyperbolic flux functions and a central scheme to compute the pressure values. Both equations contain a strongly non-linear mobility function, and therefore the system is considered stiff. Hence, the time step of the numerical scheme is very restricted, and the numerical scheme exhibits stability issues. To improve the stability of the numerical scheme a Taylor-Galerkin method is applied to the entire system. The non-linearity is accounted for by introducing auxiliary variables [15]. Using this scheme we are able to resolve the very fast wave speeds that emerge from the non-linearity of the model.

The structure of the chapter is as follows: first we introduce the two-phase foam model, and discuss its characteristics in Section 5.2. For this model, a linear stability analysis is performed in Section 5.3. The results from this analysis, listed in Section 5.4, are then compared to numerical simulations discussed in Section 5.5-5.8. Finally, we discuss the outcomes of both analyses in Section 5.9.

5.2. FOAM MODEL

We use the non-dimensional model described by Riaz and Tchelepi [13] for the injection of an incompressible gas into a porous rock initially filled with water, which is given by

$$\partial_t S = -\nabla \cdot \left(\frac{Mk_{rg}}{\lambda} \mathbf{u} + G \frac{k_{rg}k_{rw}}{\lambda} \nabla z + \frac{k_{rg}k_{rw}}{N_{ca}\lambda} \frac{dP_c}{dS_w} \nabla S \right) = -\nabla \cdot (k_{rw} \nabla \bar{P}), \quad (5.1)$$

$$\nabla \mathbf{u} = 0, \quad (5.2)$$

$$\mathbf{u} = -\lambda \nabla \bar{P} + G k_{rg} \nabla z + \frac{1}{N_{ca}} k_{rg} \frac{dP_c}{dS_w} \nabla S, \quad (5.3)$$

where $S = (S_g - S_{gr}) / (1 - S_{wc} - S_{gr})$ is the normalized gas saturation,

$$\nabla \bar{P} = \nabla P_w + (\rho_w g k / \mu_w U) \nabla z \quad (5.4)$$

is the derivative of the scaled pressure \bar{P} , $P_c = P_w - P_g$ the capillary pressure, u the total Darcy velocity, and $\lambda = Mk_{rg} + k_{rw}$ the dimensionless mobility function. Here, $k_{r\alpha}$

denote the relative permeability functions of phase $\alpha \in w, g$, which are defined later on. The variables M , G and N_{ca} denote the dimensionless end-point mobility ratio, gravity number and capillary number respectively, which are given by

$$M = \frac{\mu_w k_{rge}}{\mu_g k_{rwe}}, \quad (5.5)$$

$$G = \frac{k\Delta\rho g}{\mu_g U}, \quad (5.6)$$

$$N_{ca} = \frac{\mu_g UW}{\gamma_{gw}\sqrt{\phi k}}, \quad (5.7)$$

where W is a characteristic length scale of the model where viscous and capillary terms are of comparable magnitude [10], and U is a characteristic velocity, which is set equal to the gas injection rate divided by a unit surface area. The other parameters are explained in Appendix A. We consider the one-dimensional version of this equations with $\mathbf{u} = 1$, given by

$$\partial_t S + \partial_x \left(f(S) + \frac{k_{rg}k_{rw}}{N_{ca}\lambda} \frac{dP_c}{dS_w} \frac{dS}{dx} \right) = 0. \quad (5.8)$$

If capillary pressure is neglected ($Ca \rightarrow \infty$) this equation is the Buckley-Leverett equation with a non-convex flux

$$f = \frac{Mk_{rg}}{\lambda} \left(1 + G \frac{k_{rw}}{M} \right), \quad (5.9)$$

for which we can derive the characteristic solution. The characteristics of this solution depend on the form of the normalized relative permeability functions k_{rw} and k_{rg} , which are given by

$$k_{rg} = \frac{S^{n_g}}{f_{mr}}, \quad f_{mr} = 1 + R \cdot F_w, \quad (5.10)$$

$$k_{rw} = (1 - S)^{n_w}, \quad (5.11)$$

where f_{mr} is the mobility reduction factor due to foam generation, R is a constant that accounts for the maximum flow resistance of the foam. The function F_w describes the dependency of the foam strength to water saturation, and is given by [16]

$$F_w = 0.5 + \frac{\arctan(\kappa(S_w - S_w^*))}{\pi}, \quad (5.12)$$

where S_w^* represents the limiting water saturation and κ is a positive parameter that controls the width of the gas-foam transition. For $\kappa = \infty$ the gas-foam transition is instant (Fig. 5.1a), and no foam exists below S_w^* . For smaller values of κ , the mobility reduction of foam (i.e. of the foam strength) increases as the water saturation increases in the transition zone (Fig. 5.1b). In other words, foam collapse occurs over a range of water saturations whose width is determined by κ . The corresponding flux functions and derivatives are shown in Fig. 5.2.

The characteristic solution of the Buckley-Leverett equation for gas injection into a water saturated medium with the given relative permeability functions, consists of a

rarefaction and a right-moving shock wave [17] as shown in Fig. 5.3. The shock-speed v_s can be determined from

$$v_s = \left. \frac{df(S)}{dS} \right|_{S_s} = \frac{f(S_s) - f(S_i)}{S_s - S_i}, \tag{5.13}$$

where S_s is the shock saturation, and $S_i = 0$ is the initial gas saturation in the porous medium. For saturation values larger than S_s the solution consists of a rarefaction wave, for which $x/t = f'(S(x, t))$ [18].

5

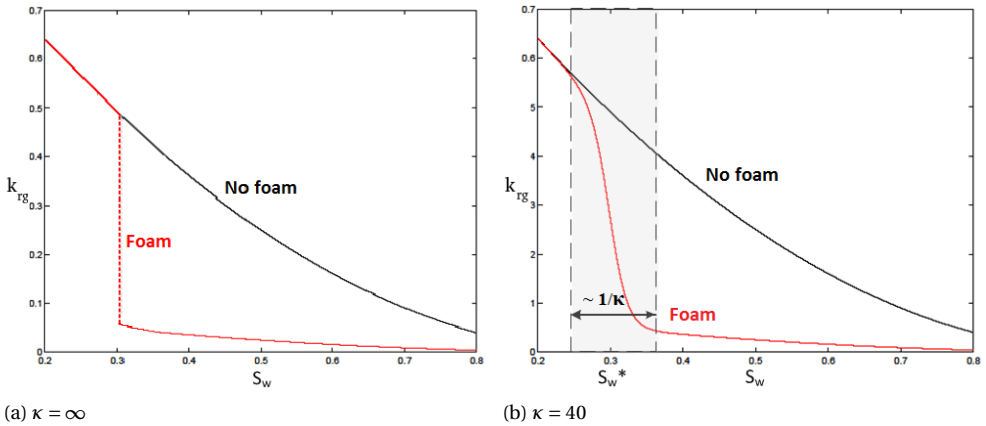


Figure 5.1: Relative permeability function of the local-equilibrium foam model with foam present ($f_{mr} > 1$) and without foam present ($f_{mr} = 1$). The sudden drop in the relative permeability of gas, due to foam, is shown for different transition rates κ , for $S_w^* = 0.3$, $R = 10$, $M = 1$ and $G = 0$ [19].

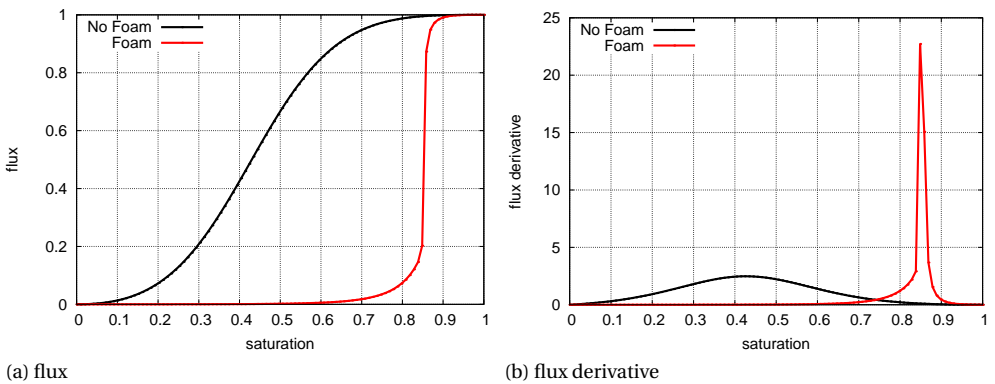


Figure 5.2: Flux function and flux derivative of the local-equilibrium foam model with and without foam present, for $S_w^* = 0.15$, $\kappa = 1000$, $R = 1000$, $M = 1$ and $G = 0$ [19].

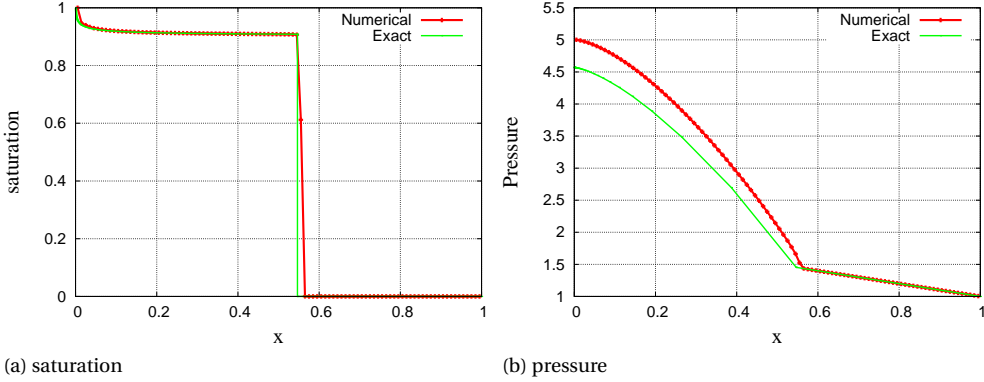


Figure 5.3: Saturation and pressure solution of the Buckley-Leverett equation at $t = 0.05$, for $S_w^* = 0.1$, $\kappa = 1000$, $R = 10000$, $M = 1$ and $G = 0$.

5.3. LINEAR STABILITY ANALYSIS

To analyze the influence of foam on the stability characteristics of the fluid displacement, we perform a linear stability analysis on Eq. 5.1 and 5.2, where we start off with the full system including capillarity. To do so, we linearize the equations around a base state that is given by the characteristic solution of the one-dimensional version of the saturation equation, Eq. 5.8. For this equation a self-similar solution exists as a function of $\xi = x - v_s t$, in the neighborhood of the Buckley-Leverett shock where $\xi = 0$, which does not change in time [10]. This solution can be used as the base state (S_0, P_0) for the stability analysis [13], which is given by

$$\frac{dS_0}{d\xi} = \frac{\lambda Ca}{k_{rw} k_{rg} P'_c} (v_s S_0 - f(S_0)), \quad (5.14)$$

$$\frac{dP_0}{d\xi} = \frac{1}{\lambda} \left(G k_{rg} + \frac{k_{rg}}{Ca} P'_c S'_0 - 1 \right). \quad (5.15)$$

In the absence of capillarity ($Ca \rightarrow \infty$) the base state satisfies

$$\frac{S_0}{d\xi} = \delta(\xi), \quad (5.16)$$

$$\frac{dP_0}{d\xi} = \frac{G k_{rg} - 1}{\lambda}. \quad (5.17)$$

We can expand the full solution in terms of the base state and a perturbation function [13]. The last is written as a set of stream-wise eigenfunctions \hat{s} and \hat{p} times a normal mode series, such that

$$(S, P)(\xi, y, t) = (S_0, P_0)(\xi) + (\hat{s}, \hat{p})(\xi) e^{iny + \sigma t}, \quad (5.18)$$

where n denotes the wavenumber of the perturbation and σ the wave growth rate. Substituting this eigenmode expansion into Eq. 5.1 and 5.2, and solving the resulting eigen-

value problem [12, 13], leads to an expression for the disturbance velocity:

$$\frac{\sigma}{n} = \frac{f_{g_1} - f_{g_0}}{S_1 - S_0} \frac{\lambda_1(1 - Gk_{rg_0}) - \lambda_0(1 - Gk_{rg_1})}{\lambda_1 - \lambda_0}, \quad (5.19)$$

where the subscripts 0 and 1 denote the front and back edge of the shock respectively. The derivation of these equations can be found in Appendix B. If there is no gravity influence ($G = 0$), i.e. if we consider a horizontally located reservoir, this becomes

$$\frac{\sigma}{n} = \frac{f_{g_1} - f_{g_0}}{S_1 - S_0} = v_s \Lambda, \quad (5.20)$$

$$\Lambda = \frac{M_s - 1}{M_s + 1}, \quad (5.21)$$

where $M_s = \lambda_1/\lambda_0$, the mobility ratio across the shock, and Λ is the disturbance number. Hence we see that this number is positive if $M_s > 1$, which means that the flow is unstable at the shock. Vice versa, a mobility ratio smaller than one leads to a stable displacement. If gravity is included it has been shown by Riaz and Tchelepi [13] that

$$G(k_{rg_1} - M_s k_{rg_0}) < 1 - M_s \quad (5.22)$$

to obtain stable displacement. If capillarity is included, apart from the shock mobility ratio, the fractional flow profiles have an influence on the stability of the flow. In the limit of small wave numbers the disturbance velocity can therefore be extended to a higher-order formulation [10], given by

$$\sigma = \Gamma_1 n + \Gamma_2 n^2 + \Gamma_3 \ln(n(s_1 - s_0)) n^2, \quad (5.23)$$

where Γ_1 is given by Eq. 5.19 and Γ_2 and Γ_3 are determined by the derivative of the total mobility and the fractional flow profiles.

5.4. STABILITY CHARACTERISTICS

The above analysis for the model without capillarity and gravity allows us to investigate the influence of foam on the viscous instability at the front. Based on the results of Farajzadeh *et al.* [3], different scenarios are addressed: a weak foam (low mobility reduction factor, case 1), three cases of a strong foam (high mobility reduction factor, case 2 to 4) with different transition lengths from foam to gas (see Fig. 5.4), and a fifth case with the effect of gravity included.

Since we only looked at the linearized model without capillarity, there is no damping at large wave numbers [13], and hence the wave growth is a linear increasing function of the wave number. Moreover, the base state of the model without capillarity contains a shock wave at $S_0 = S_s = \max_S \frac{f_g(S) - f_g(S_R)}{S - S_R}$, which marks the interface between gas and water. The shock wave is followed by a rarefaction wave, where water and gas co-exist. As shown in Fig. 5.5a the shock saturation of water (gas) is almost everywhere smaller (larger) than the limiting water (gas) saturation, i.e. the saturation that marks the transition from gas to foam. Therefore, only due to a numerically and/or physically dispersed shock (denoted by red dashed lines), or a very wide transition range of foam (denoted by

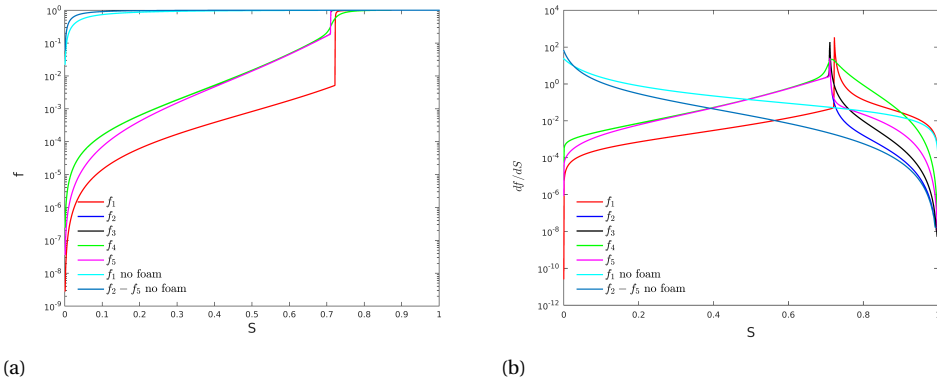


Figure 5.4: (a) Flux functions and (b) flux derivative/wave speed of the five test cases of Farajzadeh *et al.* [3] and two reference cases without foam.

blue dashed lines), foam can exist in this model. The second plot (Fig. 5.5b) shows that the shock speed increases with the limiting water saturation, because strong foam slows down the front significantly. It follows from Eq. 5.20 that the viscous instability increases linearly with the shock speed. Thus a strong foam has less instabilities than a weak foam, according to this analysis. This corresponds to the results obtained by Farajzadeh *et al.* [3].

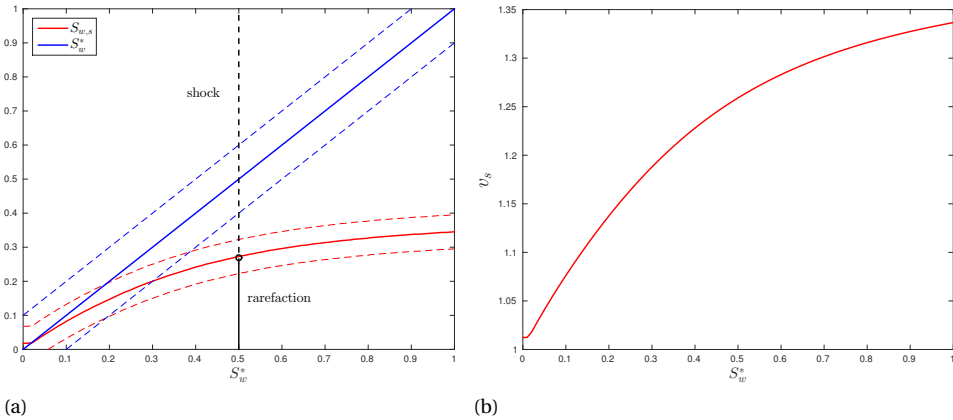


Figure 5.5: (a) Shock saturation, S_S , versus the limiting water saturation, S_W^* , for $\kappa = 1000$, $R = 1000$, and $G = 0$. (b) Shock speed, v_S , versus the limiting water saturation, for $\kappa = 1000$, $R = 1000$, and $G = 0$. The red dashed lines indicate the diffusion around the shock, because of capillarity and/or numerical diffusion. The blue dashed lines indicate the transition width of the foam, which is governed by the inverse of κ .

We can also examine the influence of the mobility ratio on the growth rate of the various test cases described in Farajzadeh *et al.* [3], as depicted in Fig. 5.6a. As the mo-

bility ratio increases the growth rate also increases. For a small mobility ratio the growth rate increases very fast for the fifth test case f_5 , after which it scales with approximately $M^{1/2}$, which is similar to what Riaz and Tchelepi [12] observed for their test cases without foam. The first three cases including foam (denoted by f_1, f_2, f_3), show an overall increase of $M^{1/2}$ and the fourth test case f_4 has a more or less constant growth number which is always smaller than zero. This implies that the fourth test case is always stable, whereas the first test case is always unstable ($\sigma/n > 0$). The other three test cases are unstable at the shock front for larger mobility ratios only, according to this analysis. Also, if we have a look at the mobility ratio across the shock depicted in Fig. 5.6b, we see the same pattern. For the fourth test case the shock ratio $M_s < 1$ for all M , which is according to our expectations and implies a stable displacement for all values of M . For the first test case $M_s > 1$ for all M , implying an unfavorable displacement, with instabilities. The other three test cases have an unfavorable mobility ratios for values of $M > 10$. Moreover, for large viscosity ratios we observe a oscillatory pattern due to the total mobility values, which are very sensitive to small changes in the parameters (see Fig. 5.11a).

5

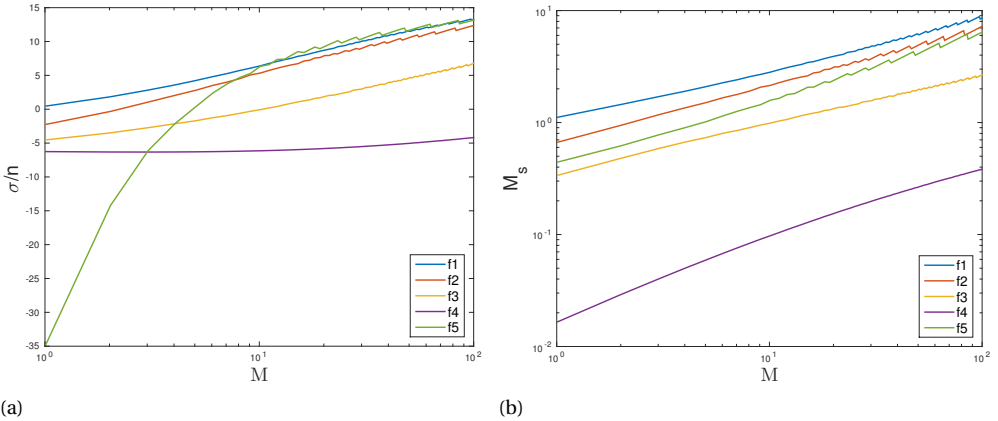


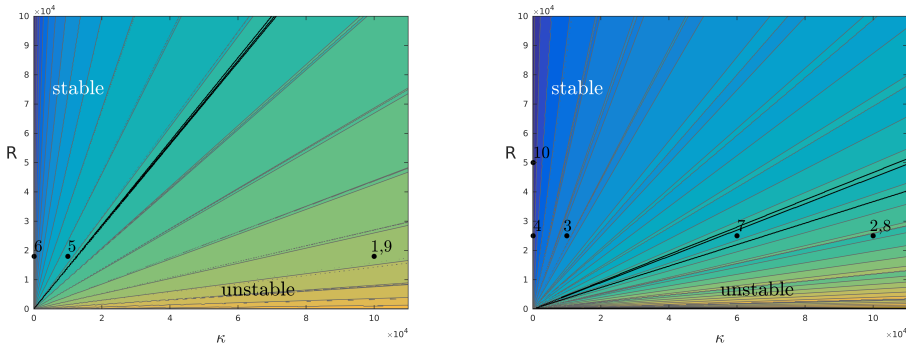
Figure 5.6: (a) Growth rate versus the mobility ratio M (b) Total mobility ratio across the shock versus M , for the five test cases of Farajzadeh *et al.* [3]

Since the foam models are characterized by the parameters R , κ and S_w^* , we studied the influence of these parameters on the dimensionless growth number Λ . Figure 5.7 shows the contour lines of the growth number in the $\kappa - R$ plane, for the remaining parameter sets of test case one and two of Farajzadeh *et al.* [3]. The stable region for the parameter set of the first parameter set defined in Table C.1 is much larger than for the parameter set of test case 2 to 4. This is probably an effect of the mobility ratio, which is larger for the second parameter set ($M_2 = 235$ vs $M_1 = 61$). We also observe that the stability contour lines, which are set by the dimensionless growth number, are all straight with a positive angle. This means that an increasing mobility reduction factor (R) has a stabilizing effect, while an increasing non-linearity (κ) has a destabilizing effect. Hence, a strong foam (higher R with a small transition width κ) is usually stable, while a weak foam (lower R) can become unstable quickly for relatively low values of κ . Test case 1

and 2, are examples of a weak and a strong foam that are unstable, while test case 3, 4 and 5 are stable according to this analysis. Finally we see, that between the region of instability and stability there is a zone, which can be both stable and unstable. This is due to a strong sensitivity of the shock mobility, to the foam parameters κ and R , which becomes larger if R increases. Overall, we can deduce that the isolines of the dimensionless growth number are linear and hence we can write

$$\frac{\partial \Lambda}{\partial R} + a \frac{\partial \Lambda}{\partial \kappa} = 0, \quad (5.24)$$

where $a = \frac{\Delta \kappa}{\Delta R}$ is a constant wave propagation speed, which can be linked to the growth of disturbances in the $\kappa - R$ space. This speed is highest for low R and high κ values.



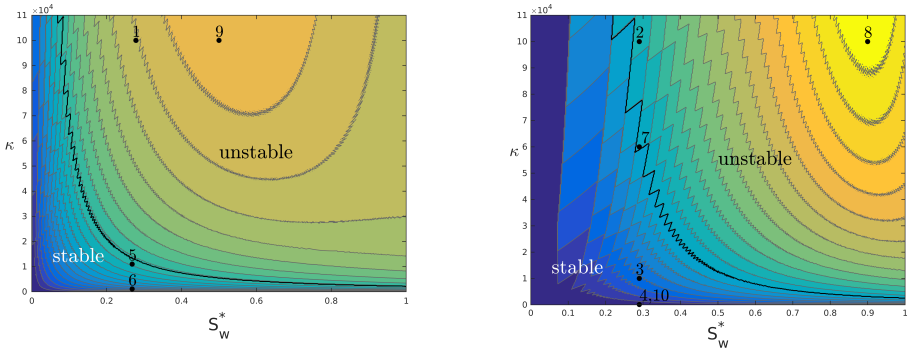
(a)

(b)

Figure 5.7: Stability regions in the $\kappa - R$ plane for the rest of the parameter set of (a) test case one, and (b) test case two of Farajzadeh *et al.* [3]. The stable and unstable regions are separated by the thick black lines and the different test cases are denoted by thick black dots.

The influence of the limiting water saturation S_w^* is more complicated, as can be seen in Fig. 5.8 and 5.9. These figures depict the disturbance velocity, and show that the solutions are stable only for low values of the limiting water saturation. This can be partly explained by Fig. 5.5a, which shows that the region where foam can exist for this model is limited to values of $S_w^* < 0.4$. Hence, a limiting water saturation that is larger implies that there is no foam present such that instabilities at the front are not subdued. Moreover, we observe that the region of the highest disturbance velocities is located around $S_w^* = 0.6$ for the first parameter set, and around $S_w^* = 0.9$ for the second parameter set. As can be deduced from Fig. 5.7, the growth number is highest for low R and high κ . So, even if there is no foam present, the choice of S_w^* influences the stability of the solutions, since both the shock saturation and the shock velocity increase with an increasing limiting water saturation (see Fig. 5.5). The disturbance velocity scales linearly with the shock velocity and hence will increase too, and the dimensionless growth number depends on the mobility ratio around the shock, which will be larger if the shock saturation increases. Hence, we see that large values of S_w^* introduce a non-physical effect in the model by changing the shock saturation, although foam is absent. However, foams effective in

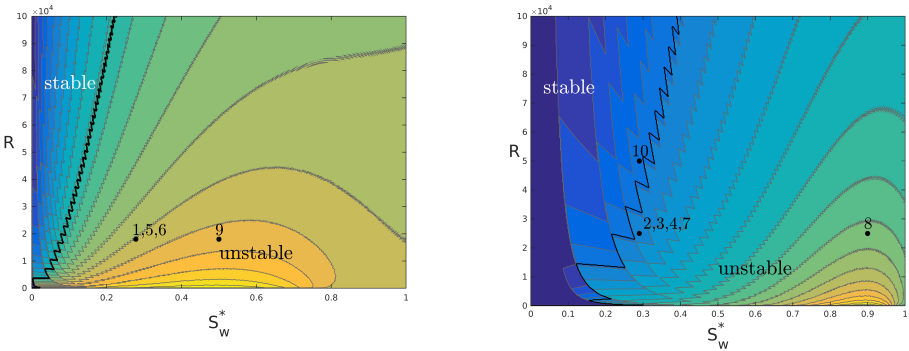
surfactant-alternating-gas (SAG) applications are expected to have a small limiting water saturation in combination with a non-zero transition width [20].



(a)

(b)

Figure 5.8: Stability regions in the $S_w^* - \kappa$ plane for the rest of the parameter set of (a) test case one, and (b) test case two of Farajzadeh *et al.* [3]. The stable and unstable regions are separated by the thick black lines and the different test cases are denoted by thick black dots.



(a)

(b)

Figure 5.9: Stability regions in the $S_w^* - R$ plane for the rest of the parameter set of (a) test case one, and (b) test case two of Farajzadeh *et al.* [3]. The stable and unstable regions are separated by the thick black lines and the different test cases are denoted by thick black dots.

In Section 5.8 of this chapter we introduce six additional test cases that are located in highly unstable or stable parts of the parameter space, or around the boundaries of the stable parameter range. Those are also depicted in Figs. 5.7 to 5.9 and support the conclusions that can be drawn from this linear stability analysis.

5.5. NUMERICAL METHODS

The results from the linear stability analysis can be compared with the results obtained by high resolution two-dimensional numerical simulations of foam on a rectilinear grid with a horizontal injection well. The two-dimensional reservoir simulator was further developed by the first author for this purpose, and based on the numerical simulator described in Van der Meer *et al.* [19]. We address the same test cases as in Farajzadeh *et al.* [3]. For the second case, an interesting artifact was observed in the apparent viscosity of the foam, in the form of a fingering pattern behind the foam front (Fig. 5.10). These fingers did not significantly influence the saturation behind the front. Therefore it was not clear from these results whether this is a physical effect or a numerical artifact. To analyze this effect, and validate the numerical simulations of the foam model, we repeat the first four test cases of Farajzadeh *et al.* [3]. Instead of solving the equations in a fully

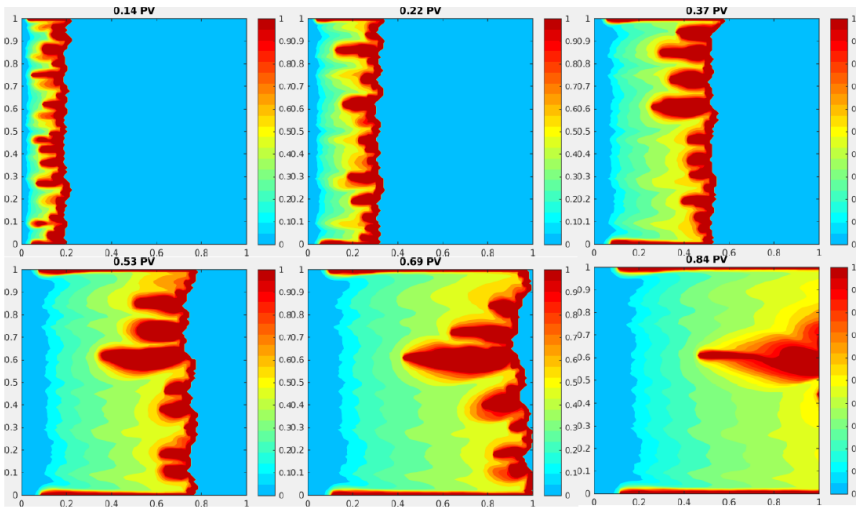


Figure 5.10: Instabilities in the apparent foam viscosity (from Farajzadeh *et al.* [3]).

implicit way, we opt for the implicit pressure explicit saturation (IMPES) method, which is designed for this kind of hyperbolic-elliptic problems because it takes into account the different nature of the equations. Because of the non-linearity in the foam parameters, the numerical stability of the foam simulations is a major concern [21]. To improve the stability of the numerical scheme a Taylor-Galerkin method is applied to the entire system. The non-linearity is accounted for by introducing auxiliary variables [15]. Using this scheme we are able to resolve the very fast wave speeds that emerge from the non-linearity of the model. Additionally, solving the saturation equation explicitly with a higher-order scheme introduces less artificial diffusion. This is important in this case, because we are interested in the detailed fingering behavior at the front and behind the front. By using operator splitting, as described in Hvistendahl Karlsen *et al.* [22] and Van der Meer *et al.* [19], we can split the saturation equation into a hyperbolic conservation law and an ordinary differential equation (ODE) for the mass flow rate. They are solved sequentially using a second-order Strang splitting scheme, which preserves the sym-

metry of the operator. The hyperbolic equation is solved with a second-order MUSCL scheme, which is a total variation diminishing finite volume method reconstructed from the first-order Godunov's method [23]. The TVD property prevents instabilities to occur that are due to the numerical method. In other words, a TVD scheme is monotonicity preserving if the Courant-Friedrichs-Levy (CFL) condition on the time step is satisfied [23]. The ODE is solved by the second-order trapezoidal rule, which is A-stable and therefore suitable for stiff ODEs [24]. The size of the time step of an A-stable method does not suffer from stringent restrictions and the choice only depends on the desired accuracy. For the elliptic equation 5.2 we use a multi-grid linear solver that combines a five-point stencil with a nine-point stencil that is rotated by 45 degrees to reduce the grid-orientation effect [25]. The five-point stencil accounts for the unrotated coefficients and is combined with a nine-point stencil that accounts for the rotated coefficients and is projected back onto the original grid. The domain is parallelized by MPI using the HYPRE library [26] to speed up the computations, since roughly 73% of the simulation time is spent on the pressure solver for this model [27].

5

5.6. NUMERICAL RESULTS

The foam displacement is modeled in a reservoir of size $1 \times 1 \times 1$ m, discretized using 300 grid blocks in the first two directions and one grid block in the z -direction (hence we have a 2D model). The porous medium used in the model has porosity $\psi = 0.2$, and a log-random permeability field with an average permeability $K = 5 \cdot 10^{-13}$ m², a Dykstra-Parsons coefficient of 0.1 and correlation lengths $L_x = 0.01$ and $L_y = 0.01$. Initially the reservoir is filled with water mixed with surfactants, and pure gas is injected at a fixed injection rate I , via a horizontal injector along the entire left side of the reservoir. Water and gas are then produced via a horizontal producer along the right side of the reservoir, keeping the pressure constant at 50 bar. In Table C.1 the parameter values for each of the cases are specified. The resulting saturation and apparent viscosity profiles for the first four test cases and two reference cases are discussed below.

The apparent gas viscosity is given by the product of the gas viscosity and the mobility reduction factor,

$$\mu_f = \mu_g \cdot f_{mr}(S), \quad (5.25)$$

and is therefore a function of the saturation. This quantity will be greatest at the foam front and decrease quickly up to the injection point as shown in Fig. 5.11b.

5.6.1. TEST CASE 1

Test case 1 describes a foam displacement process with a relatively low resistance of foam to flow (R), and a low limiting water saturation (S_w^*), which means that the effective foam viscosity μ_f is still much higher than the water viscosity μ_w . Hence the flow is characterized by instabilities like viscous fingering, as shown in Fig. 5.12. This is reflected in the interfacial length, growth rate and vorticity norm of the simulation (see Fig. 5.18). These consist of three stadia: first there is a quick increase visible in the growth rate, whereafter it is more or less linear, and then becomes constant.

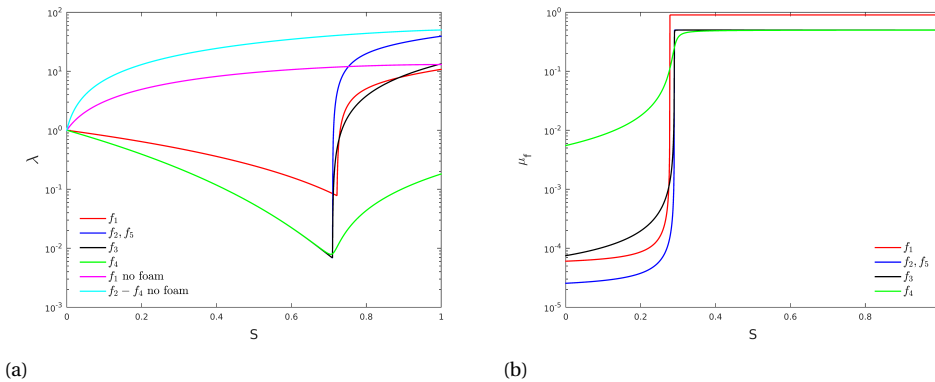


Figure 5.11: (a) Total mobility and (b) apparent viscosity of the five test cases of Farajzadeh *et al.* [3].

5.6.2. TEST CASE 2

The second test case describes a strong foam, with a high resistance of foam to flow and high limiting water saturation, and a very sharp transition from gas to foam (κ). This sharp transition from gas to foam could potentially lead to numerical instability, if not treated with appropriate care [21, 28]. It was for this test case that Farajzadeh *et al.* [3] observed the viscous fingering pattern behind the front in the apparent viscosity of the foam (see Fig. 5.13).

5.6.3. TEST CASE 3

The third test case resembles test cases 2 and 4, apart from the transition speed from gas to foam, which is a factor 10 lower here than for test case 2 and a factor 10 higher than test case 4. The simulation results are shown in Fig. 5.14.

5.6.4. TEST CASE 4

Test case 4 simulates a strong foam, with a relatively wide transition zone between gas and foam. This means that the numerical method will have no major stability issues, and the restriction on the time step is less than for the three preceding cases. As shown in Fig. 5.15 the foam front is stable, since the foam is strong and no fingering behind the front is observed, which is in agreement with the results of Farajzadeh *et al.* [3].

5.6.5. REFERENCE CASES WITHOUT FOAM

As a reference, we repeat the above simulations without foam for test case 1 and 2 (case 3 and 4 only differ in foam transition width from case 2). The simulation results are shown in Fig. 5.16 and 5.17. Since there is no foam present, the apparent foam viscosity is equal to the gas viscosity, which is constant everywhere. Therefore we show the total viscosity in the figures on the right. The difference in the solutions with foam is striking, since the fingers for these two cases are less pronounced, because the shock is much more diffused. Also, gas breakthrough is almost immediate for these cases and the difference

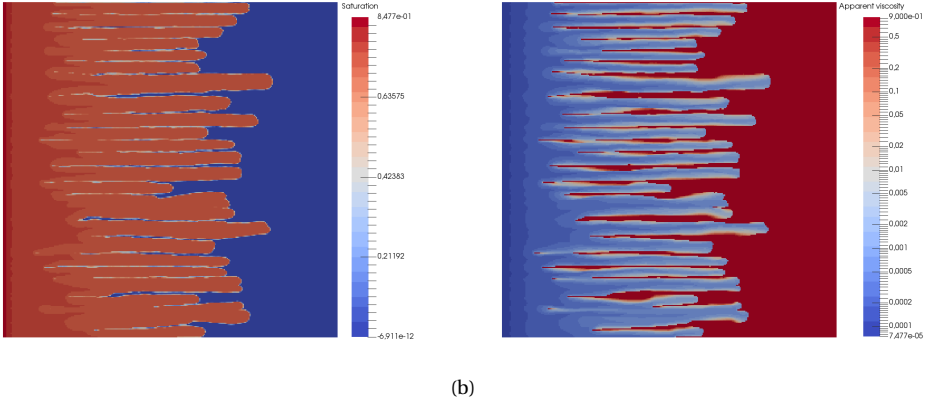


Figure 5.12: (a) Saturation profile and (b) logarithm of the apparent foam viscosity, for the first test case of Farajzadeh *et al.* [3] after 0.4 PV of injected gas.

5

between case 1 and 2 without foam is much less, than in the presence of foam.

5.7. NUMERICAL STABILITY ANALYSIS

We can approximate the growth rate σ numerically [12], by the vorticity norm

$$\bar{\omega} = \sqrt{\int_0^1 \int_0^1 \omega^2 dx dy}, \quad (5.26)$$

where

$$\omega = \frac{1}{\lambda_T} \frac{d\lambda_T}{dS} \nabla S \times u, \quad (5.27)$$

is a measure of the rotation at the finger tips. The maximum growth rate can then be approximated by:

$$\sigma_{\max} \approx \ln \left(\frac{\bar{\omega}(t)}{\bar{\omega}(t - \Delta t)} \right) / \Delta t. \quad (5.28)$$

The dominant mode can be measured numerically as a function of time, using the energy spectrum of the solutions, so that

$$n_{\max} \approx \frac{\int_0^K k E(k, t) dk}{\int_0^K E(k, t) dk}, \quad (5.29)$$

where E is the energy spectrum [29], which is computed by

$$E(k, t) = \left(\int_0^1 \left[\int_0^1 \omega(x, y, t) dx \right] e^{-ikt} dy \right)^2. \quad (5.30)$$

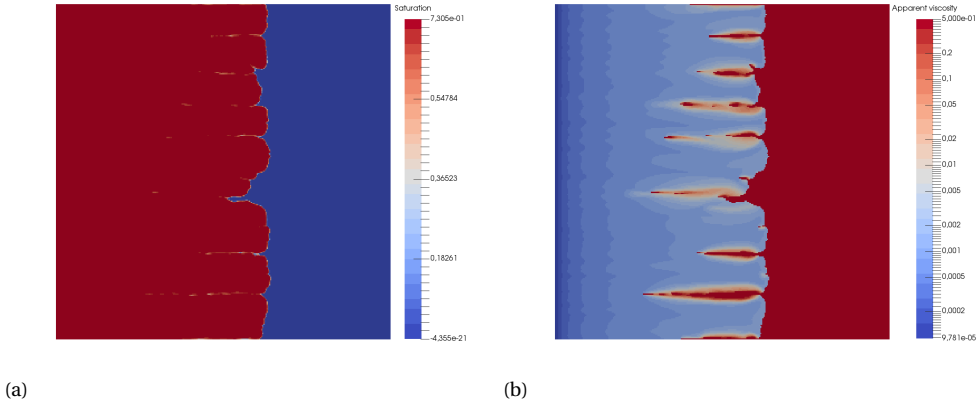


Figure 5.13: (a) Saturation profile and (b) logarithm of the apparent foam viscosity, for the second test case of Farajzadeh *et al.* [3] after 0.35 PV of injected gas.

The disturbance number Λ_{num} , which is a measure of perturbation growth with respect to the front speed, can then be approximated by

$$\Lambda_{\text{num}} = \frac{\sigma_{\text{max}}}{n_{\text{max}}}. \quad (5.31)$$

Likewise the interfacial length Γ , which is a measure of the amount of fingering or instability going on, can be approximated numerically [12] by

$$\Gamma \approx \int_0^1 \int_0^1 \sqrt{\left(\frac{\partial S}{\partial x}\right)^2 + \left(\frac{\partial S}{\partial y}\right)^2} dx dy \quad (5.32)$$

In the figures below, those quantities were approximated for the same test cases as above (see Fig. 5.18, 5.19, 5.20, 5.21) and compared to each other in Fig. 5.22. In Fig. 5.18 we see that the interfacial length shows three stages, starting off very fast for small times, and then very slowly descending, while finally becoming almost constant. Compared to the case without foam, the initial growth is larger, but while the no-foam case slows down eventually due to merging of small fingers into big ones [10, 12], the interfacial length for this weak foam case keeps increasing over the observed period of time. It could be the case that a larger reservoir is needed for the interfacial length to decrease. Also we have to mention that the approximated interfacial length sums over the squared partial derivatives in each grid block. Since the foam model contains a peak in the derivative around the limiting water saturation, this approximation overestimates the total interfacial length at the front. This measure is therefore more suited to compare the quantitative behavior of the fingers with each other, than to give a qualitative measure for the front interfacial length. The same is true for the growth rate, which takes into account the derivative of the mobility, which is highest behind the front, and thus does not directly reflect the instabilities at the front. However, it was the unstable behavior behind

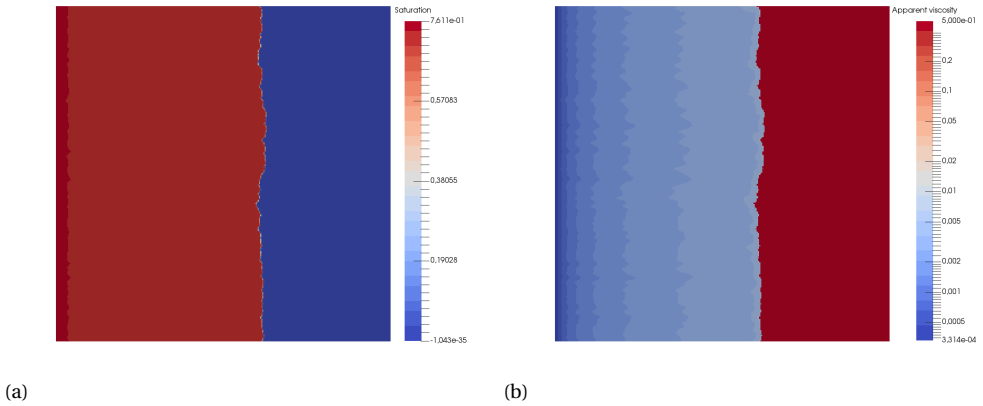


Figure 5.14: (a) Saturation profile and (b) logarithm of the apparent foam viscosity, for the third test case of Farajzadeh *et al.* [3] after 0.42 PV of injected gas.

5

the front that is of interest in this chapter. The consequence of this is that the growth rate of instability measure shows a much higher variation than for the foam case. The average growth rate is more or less constant after an initial increase. The growth rate for the case without foam is decreasing first and later showing a small increase, that could be due to numerical issues since it was not observed by Riaz and Tchelepi [12]. The vorticity norm gives a more consistent pattern, which resembles the interfacial length, and after a fast initial growth, shows a slight decrease, after which it increases very slowly.

For the second test case we see the same initial increase of the interfacial length as for the first test case in Fig. 5.19, after which it remains constant. The same case without foam shows a gradual increase which becomes constant after some time. The growth rate decreases for the model without foam after which it becomes negative (due to the gas reaching the right boundary). For the strong-foam model we see again a huge variation in the growth rate, and the vorticity norm shows a steep increase after which it becomes constant. Again, the vorticity norm is higher than for the case without foam, due to the large derivatives of the mobility behind the front.

Test case 3, depicted in Fig. 5.20, gives results almost identical to the second test case, but an order 10 smaller for the growth rate and the interfacial length. The same holds for the fourth test case in Fig. 5.21, in which the growth rate is reduced by an order 1000 with respect to test case 2. Hence, we can assume that the vorticity norm of the simulations depends linearly on the parameter κ , for a strong foam (test case 2, 3 and 4), i.e.

$$\bar{\omega} \sim \kappa. \quad (5.33)$$

This means that reducing κ by approximately a factor 10 leads to a reduction in the vorticity norm by a factor 10. This can also be seen in Fig. 5.22, where the test cases are compared to each other. However, it shows that the vorticity of test case 1 is an order 10 lower than of test case 2, although they have the same transition width. This can be due to a lower mobility reduction factor for test case 1 (see Table C.1), which causes a

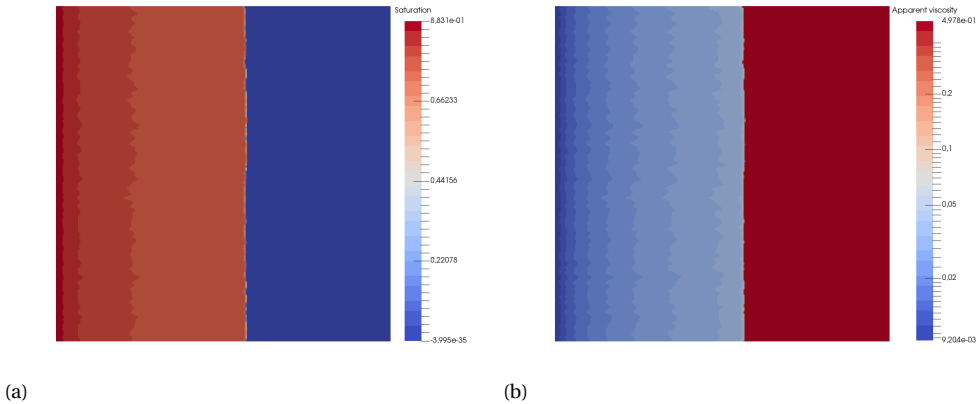


Figure 5.15: (a) Saturation profile and (b) logarithm of the apparent foam viscosity, for the fourth test case of Farajzadeh *et al.* [3] after 0.42 PV of injected gas.

smaller mobility derivative around the limiting water saturation. Hence a lower vorticity is expected behind the front, whereas an increase in fingering at the front should partly compensate for this. The interfacial length is largest for the cases without foam (until the front in the second case reaches the right side of domain, and the interfacial length drops below that of the first foam case). After that, weak foam shows the highest interfacial length, as we could also observe from the saturation plots. The strong-foam cases are all really stable at the front and therefore more or less constant around the same value. On the other hand the average growth rate for test case 2 is almost as large as for test case 1, which implies that instabilities behind the front must contribute to this result. The average growth rate of the other two test cases are smaller and almost zero. The growth rate of the case without foam is not comparable here, because of the chosen measure, as was explained before. If we compare the results with the linear stability analysis, we see that indeed a higher non-linearity (i.e. a smaller transition width from gas to foam) leads to more instability.

5.8. ADDITIONAL TEST CASES

The first four test cases that were studied before by Farajzadeh *et al.* [3] confirmed the linear stability results of this chapter numerically, but span only a very small range of the total parameter set. Therefore we introduce six additional test cases that are located in highly unstable or stable parts of the parameter space, or around the boundaries of the stable parameter range. Hence, we can see whether the patterns described in Section 5.3 can be observed also for their numerical counterparts. The parameters of the additional test cases are listed in Table C.2, and their values are depicted in the stability regions of Section 5.3 in Figs. 5.7-5.9 of Section 5.4.

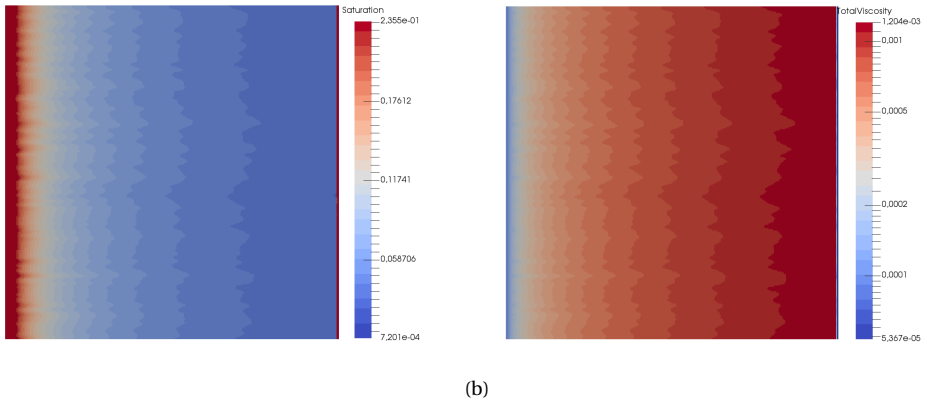


Figure 5.16: (a) Saturation profile and (b) total viscosity, for simulation case 1 without foam after 0.12 PV of injected gas.

5

5.8.1. TEST CASE 5 AND 6

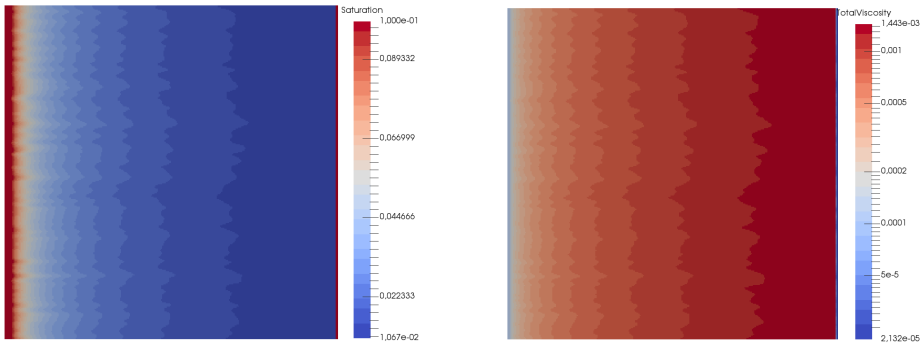
Test cases 5 and 6 are given by the same parameter set as test case 1 of Farajzadeh *et al.* [3], but with a wider transition zone ($\kappa = 10000$ and $\kappa = 100$ respectively). According to Fig. 5.7a and 5.8a, test case 5 is on the boundary between the stable and unstable region and test case 6 is in the stable region, whereas test case 1 is unstable. The simulation results of these two cases are given in Fig. 5.23.

5.8.2. TEST CASE 7

Test case 7 is an extension to test case 2 to 4, but the transition width κ is chosen such that it is located at the boundary between the stable and unstable region of Fig. 5.7b and 5.8b. This means it can exhibit both stable and unstable behavior, depending on the heterogeneity of the reservoir. In Fig. 5.24 the simulation results for this case are shown. The resulting foam front is very stable, but exhibits fingering behind the front. The results are similar to test case 2, but show less fingering behind the front, due to a longer transition width.

5.8.3. TEST CASE 8 AND 9

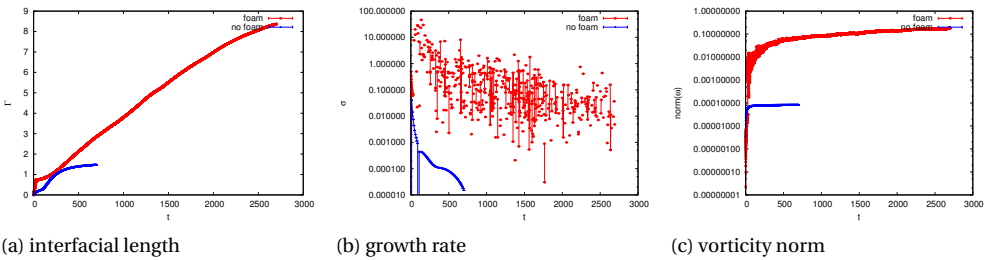
Test case 8 and 9 are extensions of test case 1 and 2 respectively, but with a higher limiting water saturation. Because of the high value of S_w^* a foam is not formed, but the effect is still there because of the model definition. This can be deduced by the fact that the analytical solution contains a shock, such that the low mobilities that are induced by the foam are bypassed. As shown in Fig. 5.5a, the shock saturation of the water phase is always below the limiting water saturation, meaning that in the 1D analytical problem there is no foam present at the shock and behind the shock, since there is not enough water present. In front of the shock there is no gas to form a foam, which means that a foam does not exist. The limiting water saturations are chosen such that the test cases are located in the most unstable region of Figs. 5.9a and 5.9b respectively. The simulation



(a)

(b)

Figure 5.17: (a) Saturation profile and (b) total viscosity, for simulation case 2 without foam after 0.06 PV of injected gas.



(a) interfacial length

(b) growth rate

(c) vorticity norm

Figure 5.18: Numerical approximation of the interfacial length, growth rate and vorticity norm for test case 1 of Farajzadeh *et al.* [3].

results are indeed both highly unstable as shown in Fig. 5.25. To investigate the influence of foam on these simulation results, we compare to the reference cases without foam, which are depicted in Figs. 5.16 and 5.17. Obviously, the results are completely different. The front is much steeper for test cases 8 and 9 compared to the two reference cases.

5.8.4. TEST CASE 10

Finally we study a test case where the mobility reduction factor of test case 2 is increased (i.e. a stronger foam). According to our analysis in Section 5.3, a higher mobility reduction implies more stable front, which can be seen in Fig. 5.26a. However, the main gain in stability is obtained behind the front, which shows less fingering, as visible in the total viscosity plot in Fig. 5.26b. If we compare this result with Fig. 5.13b of test case 2, we see that the fingering behind the front is still present for test case 10, but much less pronounced than for test case 2. An increased mobility reduction factor also has a stabilizing effect on these instabilities, and not just at the front. An increased foam strength is hence subduing the very fast waves of the gas phase, that are moving into the foam front.

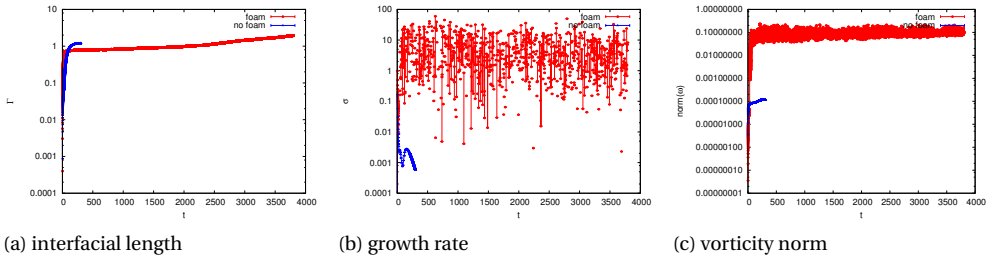


Figure 5.19: Numerical approximation of the interfacial length, growth rate and vorticity norm for test case 2 of Farajzadeh *et al.* [3].

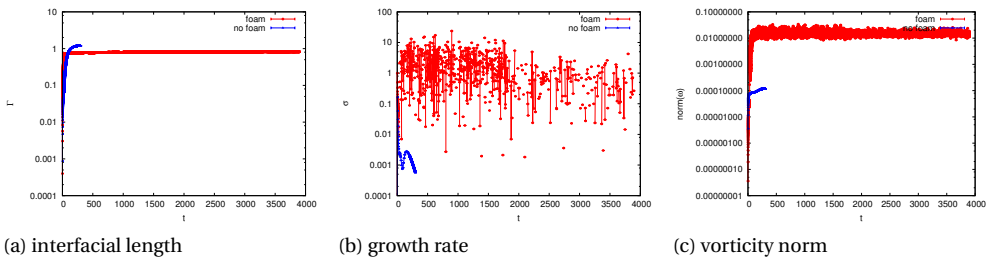


Figure 5.20: Numerical approximation of the interfacial length, growth rate and vorticity norm for test case 3 of Farajzadeh *et al.* [3].

Hence we can assume that the main trigger for these instabilities is the transition width of the gas-foam interface. Moreover, the front of test case 10 is a little bit ahead of the front of test case 2, for the same time instance. The increased stability behind the front is thus also favorable for the sweep-efficiency of the foam.

5.8.5. NUMERICAL STABILITY ANALYSIS

For the extended test cases we performed a numerical stability analysis, which shows once more that increasing the limiting water saturation (case 8 and 9) leads to a large increase in the interfacial length, even though foam is not present in theory (see Fig. 5.27a). It also shows that the cases with a smaller transition width (case 7, 8, 9 and 10) have a relatively high growth rate and viscosity norm (see Fig. 5.27b), due to fingering behind the front. The cases with a broader transition width between gas and foam, do not exhibit this fingering behavior and show a much lower growth rate and vorticity norm. Case 5 resembles case 1 except for a lower κ , and has a very unstable front like test case 1, but is more stable behind the front, due to a wider transition zone.

5.9. CONCLUSIONS

The physical instabilities that were observed behind the front in Farajzadeh *et al.* [3] seem to be inherent to the non-linearity in the mobility of foam. The linear stability

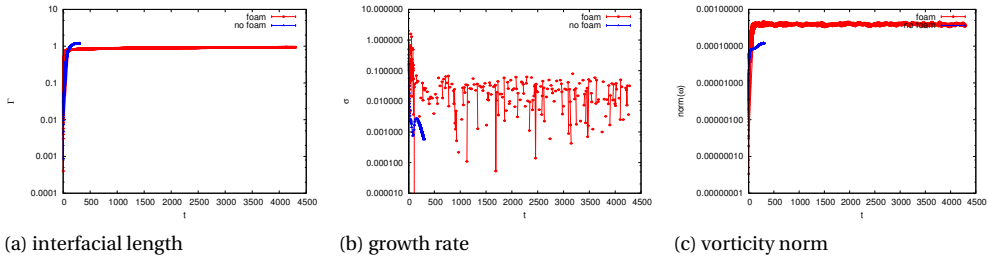


Figure 5.21: Numerical approximation of the interfacial length, growth rate and vorticity norm for test case 4 of Farajzadeh *et al.* [3].

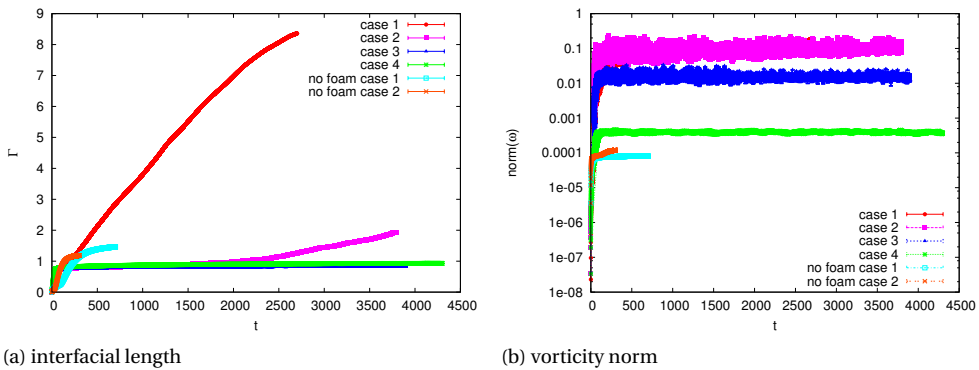


Figure 5.22: Numerical approximation of the interfacial length and vorticity norm for the first four test cases of Farajzadeh *et al.* [3].

analysis made it clear that the foam parameters κ , R and S_w^* had a significant influence on the physical stability of the results. We could identify stability regions based on the dimensionless disturbance number, which show for which parameter sets the solutions are potentially stable or unstable. The first four test cases studied in Section 5.4, and the six additional test cases in Section 5.8, confirmed these results numerically.

We found that a strong foam with a narrow transition width between gas and foam (test case 2) shows the highest growth rate of all test cases, although the front is most stable. We investigated the influence of the parameters that determine foam strength, transition width and critical water saturation on the stability characteristics of the solutions. It shows that a high mobility reduction factor (foam strength) has a stabilizing effect on the solutions, while a higher non-linearity of the gas-foam transition (shorter transition width) has a destabilizing effect. It turns out that the growth rate of instabilities is linearly dependent on both the inverse foam strength and transition width control parameters ($1/R$ and κ). There is also a strong effect of the critical water saturation on the stability characteristics.

In this research we neglected the influence of capillarity in both the linear stability

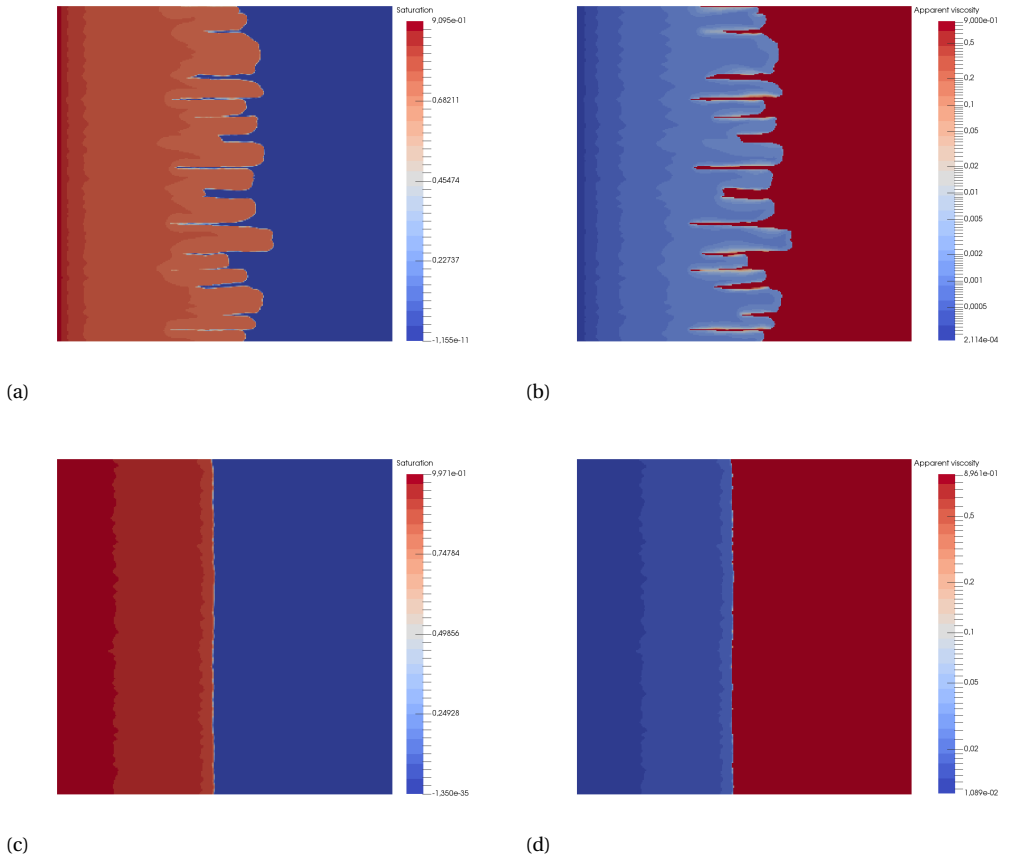


Figure 5.23: (a) Saturation profile and (b) logarithm of the apparent foam viscosity for the 5th and 6th test case, after 0.35 of injected gas.

analysis and the simulations, because it has a damping effect on the instabilities at the front. For a more realistic outcome, the effect of additional diffusion could be investigated. Furthermore we could extend this analysis to a quarter-five spot setup. This would add an extra complexity to the model due to a spatially varying strain field that affects the stability front, as was shown for a miscible flow case in Chen and Meiburg [30].

Moreover, we recommend to extend the current local equilibrium foam models to more complex models at the front, to gain more insight in the nature of instabilities that occur behind the foam front and to investigate whether they are able to cause an unstable displacement. In this case models that take into account the gas-foam interface might give an outcome.

In this thesis we did not compare our stability or numerical results with experimental results, since those experiments do not exist for this particular study. Experiments that

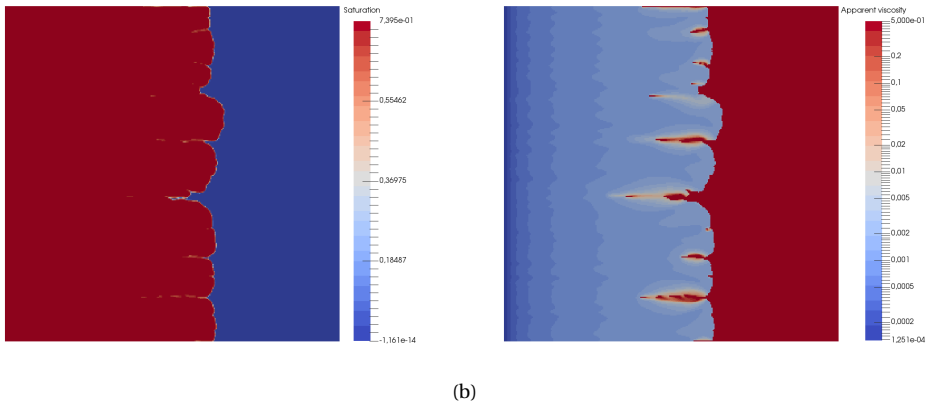


Figure 5.24: (a) Saturation profile and (b) logarithm of the apparent foam viscosity for the 7th test case, after 0.42 PV of injected gas.

look at fingering phenomena of a highly mobile gas being injected in the low-mobile foam would be very valuable to validate numerical simulations of foam enhanced oil recovery processes. One way to do this would be to create a foam between two glass plates with obstacles in between, to mimic the porous rock in two dimensions. After this gas is injected through a hole in the middle of the plates, to study the fingering behavior in a porous medium, in the presence of foam. These results can then be compared to highly accurate simulations in two dimensions.

Finally the results from the stability analysis can be used to identify important scales and wave lengths of the problem, which in turn can be adapted in building an efficient numerical solver that is able to capture both the fast waves that occur due to the foam, and the slow waves occurring in the rarefaction wave.

5.10. ACKNOWLEDGEMENTS

This research was carried out within the context of the Recovery Factory project at Delft University of Technology (TU Delft), sponsored by Shell Global Solutions International. We would like to thank Dr. Hajibeygi of TU Delft for useful discussions and suggestions about the stability analysis of the foam model.

REFERENCES

- [1] J. M. Van der Meer, R. Farajzadeh, and J. D. Jansen, *Influence of foam on the stability characteristics of immiscible flow in porous media*, in *Proc. SPE Reservoir Simulation Symposium (RSS)* (2017).
- [2] A. Riaz and H. A. Tchelepi, *Influence of Relative Permeability on the Stability Characteristics of Immiscible Flow in Porous Media*, *Transport in Porous Media* **64**, 315 (2006).

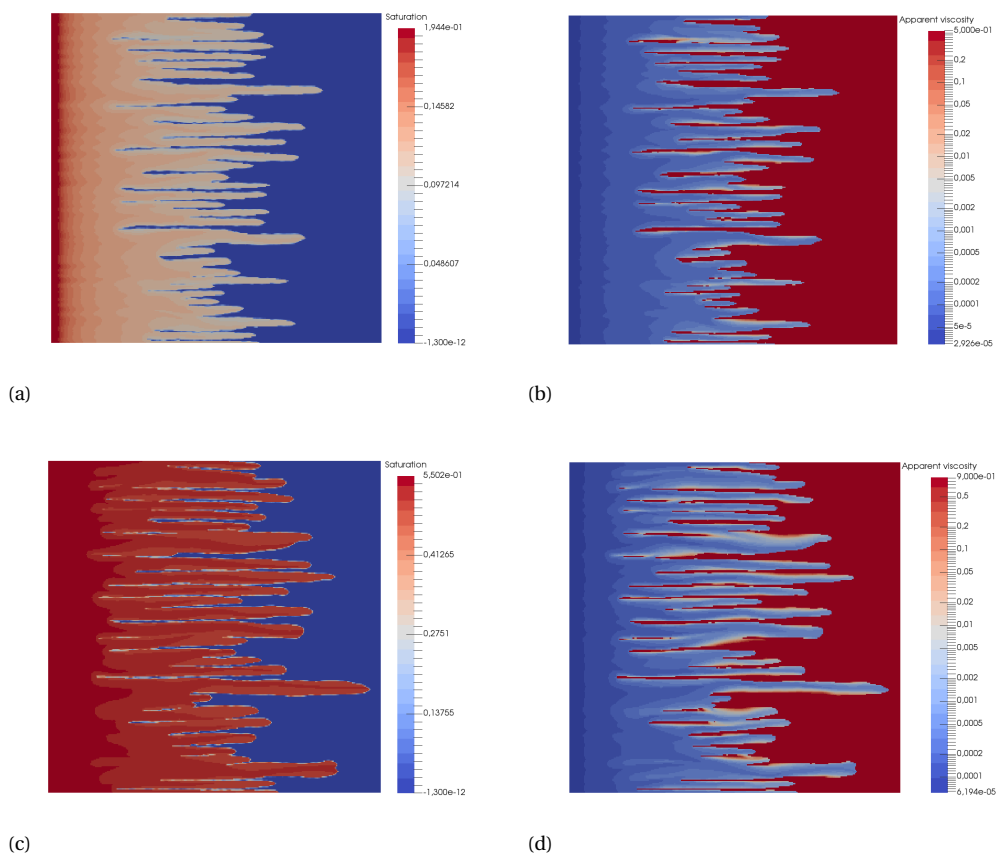


Figure 5.25: (a) Saturation profile and (b) logarithm of the apparent foam viscosity for the 8th and 9th test case, after 0.7 and 0.35 PV of injected gas respectively.

- [3] R. Farajzadeh, A. A. Eftekhari, H. Hajibeygi, S. Kahrobaei, J. M. van der Meer, S. Vincent-Bonnieu, and W. R. Rossen, *Simulation of instabilities and fingering in surfactant alternating gas (SAG) foam enhanced oil recovery*, [Journal of Natural Gas Science and Engineering](#) **34**, 1191 (2016).
- [4] Z. Khatib, G. Hirasaki, and A. Falls, *Effects of Capillary Pressure on Coalescence and Phase Mobilities in Foams Flowing Through Porous Media*, [SPE Reservoir Engineering](#) **3**, 919 (1988).
- [5] R. Farajzadeh, M. Lotfollahi, A. Eftekhari, W. R. Rossen, and G. J. H. Hirasaki, *Effect of Permeability on Implicit-Texture Foam Model Parameters and the Limiting Capillary Pressure*, [Energy & Fuels](#) **29**, 3011 (2015).
- [6] E. Ashoori, D. Marchesin, and W. R. Rossen, *Roles of transient and local equilibrium*

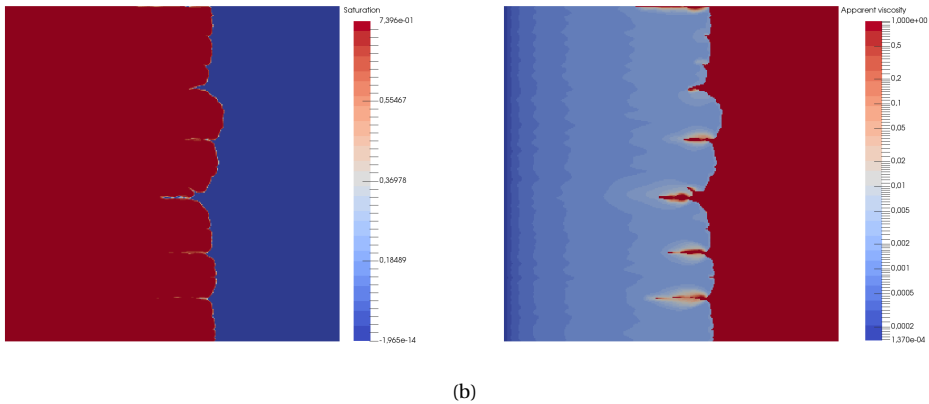


Figure 5.26: (a) Saturation profile and (b) logarithm of the apparent foam viscosity for the 10th test case, after 0.42 PV of injected gas.

foam behavior in porous media: Traveling wave, Colloids and Surfaces A: Physico-chemical and Engineering Aspects **377**, 228 (2011).

- [7] E. Ashoori, D. Marchesin, and W. R. Rossen, *Stability Analysis of Uniform Equilibrium Foam States for EOR Processes*, Transport in Porous Media **92**, 573 (2012).
- [8] M. N. Zanganeh, J. F. B. M. F. M. Kraaijevanger, H. W. Buurman, J. D. Jansen, W. R. Rossen, M. Namdar Zanganeh, J. F. B. M. F. M. Kraaijevanger, H. W. Buurman, J. D. Jansen, W. R. Rossen, and M. N. Zanganeh, *Challenges in adjoint-based optimization of a foam EOR process*, Computational Geosciences **18**, 563 (2014).
- [9] C. S. Boeije and W. R. Rossen, *Fitting Foam-Simulation-Model Parameters to Data: II. Surfactant-Alternating-Gas Foam Applications*, SPE Reservoir Evaluation & Engineering **18**, 273 (2015).
- [10] Y. Yortsos and F. J. Hickernell, *Linear Stability of Immiscible Displacement Processes in Porous Media*, SIAM J. Appl. Math. **49**, 730 (1989).
- [11] A. Riaz, M. Hesse, H. A. Tchelepi, and F. M. Orr, *Onset of convection in a gravitationally unstable diffusive boundary layer in porous media*, Journal of Fluid Mechanics **548**, 87 (2005).
- [12] A. Riaz and H. A. Tchelepi, *Linear stability analysis of immiscible two-phase flow in porous media with capillary dispersion and density variation*, Physics of Fluids **16**, 4727 (2004).
- [13] A. Riaz and H. A. Tchelepi, *Stability of two-phase vertical flow in homogeneous porous media*, Physics of Fluids **19**, 072103 (2007).

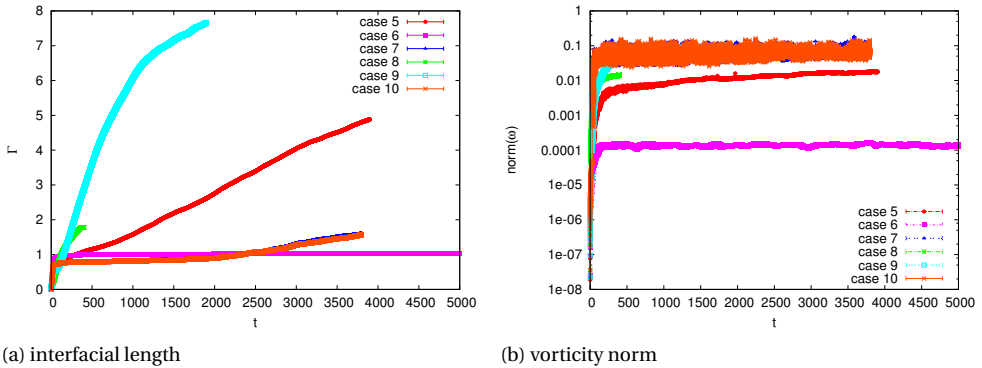


Figure 5.27: Numerical approximation of the interfacial length and vorticity norm for the last six test cases.

- [14] B. Meulenbroek, R. Farajzadeh, and H. Bruining, *The effect of interface movement and viscosity variation on the stability of a diffusive interface between aqueous and gaseous CO₂*, *Physics of Fluids* **25**, 074103 (2013).
- [15] D. Ambrosi and L. Quartapelle, *A Taylor–Galerkin Method for Simulating Nonlinear Dispersive Water Waves*, *Journal of Computational Physics* **146**, 546 (1998).
- [16] L. Cheng, A. B. Reme, D. Shan, D. A. Coombe, and W. R. Rossen, *Simulating Foam Processes at High and Low Foam Qualities*, in *SPE (Tulsa, Oklahoma, 2000)* pp. 1–15.
- [17] D. Shan and W. R. Rossen, *Optimal Injection Strategies for Foam IOR*, *SPE* **6**, 131 (2004).
- [18] R. J. LeVeque, *Numerical Methods for Conservation Laws*, 2nd ed. (Birkhauser Verlag, 1992) p. 214.
- [19] J. M. Van der Meer, D. E. A. Van Odyck, P. Wirnsberger, and J. D. Jansen, *High-order Simulation of Foam Enhanced Oil Recovery*, in *Proc. 14th European Conference on Mathematics in Oil Recovery (ECMOR XIV)* (Catania, 2014) pp. 8–11.
- [20] C. S. Boeije and W. R. Rossen, *Fitting Foam Simulation Model Parameters for SAG Foam Applications*, in *SPE Enhanced Oil Recovery Conference* (Society of Petroleum Engineers, 2013).
- [21] J. M. Van der Meer, J. B. F. M. Kraaijevanger, M. Möller, and J. D. Jansen, *Temporal oscillations in the simulation of foam enhanced oil recovery*, in *Proc. 15th European Conference on Mathematics in Oil Recovery (ECMOR XIV)* (Amsterdam, 2016).
- [22] K. Hvistendahl Karlsen, K. A. Lie, J. Natvig, H. Nordhaug, and H. Dahle, *Operator Splitting Methods for Systems of Convection-Diffusion Equations: Nonlinear Error Mechanisms and Correction Strategies*, *Journal of Computational Physics* **173**, 636 (2001).

- [23] E. F. Toro, *Riemann Solvers and Numerical Methods for Fluid Dynamics*, 3rd ed. (Springer Berlin / Heidelberg, 2009) Chap. 0, p. 540.
- [24] G. G. Dahlquist, *A special stability problem for linear multistep methods*, BIT Numerical Mathematics **3** (1), 27 (1963).
- [25] P. Wirsberger, *The grid orientation effect in miscible displacement*, Mphil dissertation, University of Cambridge (2012).
- [26] R. D. Falgout and U. Meier Yang, *Hypr: a Library of High Performance Preconditioners*, in *Preconditioners, Lecture Notes in Computer Science* (ICCS, 2002) pp. 632–641.
- [27] I. Yahya Afiff, *Reservoir simulation of foam flow using Kepler GPU*, Msc. thesis, Delft University of Technology (2014).
- [28] W. R. Rossen, *Numerical Challenges in Foam Simulation : A Review*, in *SPE Annual Technical Conference and Exhibition held in New Orleans*, October (SPE International, New Orleans, 2013).
- [29] A. Riaz and H. A. Tchelepi, *Numerical simulation of immiscible two-phase flow in porous media*, *Physics of Fluids* **18**, 014104 (2006).
- [30] C.-Y. Y. Chen and E. E. Meiburg, *Miscible porous media displacements in the quarter five-spot configuration. Part 2. Effect of heterogeneities*, *Journal of Fluid Mechanics* **371**, 269 (1998).

6

CONCLUSIONS AND DISCUSSION

6.1. CONCLUSIONS

In the introduction (Chapter 1), a number of questions were raised. The main question was:

How to improve the accuracy and stability of the numerical solutions of the local-equilibrium foam model?

We will try to answer this question in the following sections, by addressing the sub-questions that were asked in the introduction. The sub-questions were separated in two categories, for each model studied.

6.1.1. NON-LINEAR HEAT EQUATION WITH A DISCONTINUOUS COEFFICIENT

1. IS THE EQUATION WELL-POSED?

To answer this question, we need to go back to some of the basic mathematical concepts in the field of partial differential equations. For a problem to be well-posed it needs to have:

- An unique solution,
- a solution that depends continuously on the initial condition.

The non-linear heat equation with a continuous coefficient, two boundary conditions and an initial condition, is well-posed. However, if a discontinuity is occurring in the coefficients or initial conditions this is not necessarily true. In fact, for such a problem, additional (boundary) conditions are required at the discontinuous phase interface. Therefore, the solution is split in a left and a right solution that are connected through the moving phase interface (Chapter 3). In case of a highly non-linear coefficient this is not necessary, and hence we can derive an unique analytic solution for these kind of problems.

2. HOW DOES A PIECEWISE CONTINUOUS DIFFUSIVITY COEFFICIENT AFFECT THE NUMERICAL SOLUTIONS OF THE EQUATION?

If the equation is solved with a standard finite volume method that does not take into account the discontinuity in its coefficient, this will lead to temporal oscillations in the solutions that were observed in Chapter 2 and 3. The oscillations worsen, when the number of discontinuities increases.

3. HOW CAN WE IMPROVE THE FINITE VOLUME METHOD TO HANDLE DISCONTINUOUS COEFFICIENTS IN THE EQUATION?

Improved averaging schemes and adapted discretization methods can be used to smoothen the solutions (Chapter 2, 3). For the adapted grid methods it is important to enforce the necessary interface conditions at the discontinuous interface. Moreover, if an enthalpy formulation is available, for example in the case of phase change problems, one can use an enthalpy formulation and solve this instead, to improve the solutions. This will still contain some temporal oscillations, and therefore the improved averaging scheme in Chapter 2 is the easiest and most efficient solution.

6.1.2. LOCAL-EQUILIBRIUM FOAM MODEL

4. HOW DOES A HIGHLY NON-LINEAR DIFFUSION COEFFICIENT AFFECT THE NUMERICAL SOLUTIONS OF THE MODEL?

The numerical solution of the model suffers from temporal oscillations in the pressure solution, due to the highly non-linear diffusion coefficient in the pressure equation. The solution of the saturation equation is not affected when the time step is small enough. The temporal oscillations become more pronounced as the transition zone between gas and foam becomes shorter (i.e. the mobility function is steeper) and when the difference between the gas and foam mobility is larger. Moreover, due to the non-linearity, the model is very sensitive to small changes in the parameters, and hence the accuracy of the solutions and the convergence rate of the numerical solver is an issue.

5. WHAT IS THE CAUSE OF THE TEMPORAL OSCILLATIONS OBSERVED IN THE NUMERICAL SOLUTIONS OF THE MODEL?

The highly non-linear mobility function or diffusion coefficient of the model causes the temporal oscillations in the pressure solution. The non-linearity in the mobility function happens around the critical saturation, where the gas-foam front is located. The gas-foam front is in general just behind the foam-water front, and moves through the grid, when gas is injected on one side of the water-filled porous medium. Each time the gas-foam interface passes a grid block, the mobility in this grid block drops over several orders of magnitude, causing the pressure value in this grid block to shoot up. When the phase-interface passes through the next grid block the same happens here, and the pressure in the previous grid block drops again as the front proceeds. Hence, we will observe an oscillatory pressure pattern in time in each grid block, that damps out when the front moves further away from that grid block.

6. WHAT IS THE CONNECTION BETWEEN THE TWO MODELS STUDIED?

Both the non-linear heat equation with a piecewise discontinuous coefficient and the local-equilibrium foam model exhibit temporal oscillations, due to the (almost) discon-

tinuous diffusion coefficient in the diffusion equation. In the heat equation the equation is parabolic. In the incompressible local-equilibrium foam model the pressure equation containing the diffusion term is elliptic, but it becomes parabolic if a slight compressibility is added to the equation. Hence, we could say that the non-linear heat equation is a simplified version of the pressure equation in the slightly compressible local-equilibrium foam model. The main difference is that the diffusion term in the parabolic pressure equation, does not depend directly on the pressure, but on the phase saturations. Therefore the origin of the temporal oscillations of the foam model are difficult to resolve, while this is much easier for the non-linear heat equation (Chapter 2).

7. HOW CAN WE IMPROVE THE NUMERICAL SOLUTIONS OF THE MODEL?

Throughout this thesis it became clear that the local equilibrium foam model used, is extremely sensitive to small changes in the parameters, due to the gas-foam interface, which is highly unstable. Therefore, it is essential for convergence to use improved averaging schemes (Chapter 2) in combination with an adaptive grid method, like a front-tracking scheme, level-set method, or the hybrid methods that we proposed in Chapter 3. Moreover, to obtain an accurate solution, it is recommended to use a high-resolution grid or high-order solver both in space and time, as shown in Chapter 4. These numerical measures are still not able to completely avoid non-physical oscillatory behavior, which is especially a problem for models with a narrow transition zone between gas and foam. Besides that, applying adaptive grid methods and a high resolution in time and space, leads to complex numerics and a high computational effort.

8. WHAT IS THE EFFECT OF FOAM ON THE TWO-DIMENSIONAL SOLUTIONS OF THE MODEL?

It turns out that foam has a significant effect on the behavior of the gas front. As expected the simulations with foam suffer less from gravity override and viscous fingering than the simulations without foam. This leads to a better sweep of the reservoir and a much lower breakthrough time (Chapter 4). The numerical solutions in two dimensions, suffer from instabilities behind the foam-water front, due to the gas-foam front, which is highly unstable (Chapter 5). Also, we observed a severe grid-orientation effect in simulations that use a quarter five-point stencil, due to the high sensitivity of the model to the grid and model parameters (Chapter 4).

9. HOW STABLE AND ACCURATE ARE THE SOLUTIONS OF THE MODEL IN TWO DIMENSIONS?

The physical instabilities that were observed behind the front in Farajzadeh *et al.* [1] seem to be inherent to the non-linearity in the mobility of foam. We found that a strong foam with a narrow transition width between gas and foam (test case 2) shows the highest growth rate of all test cases, although the front is most stable. We investigated the influence of the parameters that determine foam strength, transition width and critical water saturation on the stability characteristics of the solutions. It shows that a high mobility reduction factor (foam strength) has a stabilizing effect on the solutions, while a higher non-linearity of the gas-foam transition (shorter transition width) has a destabilizing effect. It turns out that the growth rate of instabilities is linearly dependent on both the inverse foam strength and transition width control parameters ($1/R$ and κ). There is also a strong effect of the critical water saturation on the stability characteristics. In Chapter 5 we approximate the stability of the foam solutions 'a priori', which makes it

possible to adjust the choice of grid and the grid resolution, based on this. This will lead to a better accuracy of the solutions.

10. HOW SUITABLE IS THE MODEL? ARE THERE ANY SUITABLE ALTERNATIVES?

The severe challenges on the numerical solver and grid, described in the previous sub-questions, are not in balance with the gain we observe in the accurateness and convergence of the solutions. In other words we are jumping "out of the frying pan, into the fire". Therefore, we propose to use a more robust model to describe foam, for example by taking into account bubble density of the foam as in Chen *et al.* [2]. This will add an additional diffusion term to the model. Hence the model does no longer give a shock solution, leading to a more robust model, for which there is no need to make corrections in order to avoid non-physical oscillations.

Another problem of the foam model studied, is that the physics of the model are not coherent with the numerics. This can be deduced by the fact that the analytical solution contains a shock, such that the low mobilities that are induced by the foam are bypassed. This was explained further in Chapter 5, where it is shown in Fig. 5.5a that the shock saturation of the water phase is always below the critical water saturation. This implies that in the one-dimensional analytical problem there is no foam present at the shock and behind the shock, since there is not enough water present. In front of the shock there is no gas to form a foam, which means that a foam does not exist. However, the foam still has an effect on the analytical solution through the shock-speed, which is significantly lower when the critical water saturation is reduced. This is not in agreement with the physics of the foam process, since the model without foam should represent a normal gas-flooding process. When numerical or physical diffusion is present in the numerical solutions of the model respectively, the shock is diffused and therefore foam does exist and the low-mobility values are no longer bypassed. In some literature, among others [1] and [3], these values are called non-physical and ought to be avoided. This claim is not true because the model is not representing the actual physics. Therefore instead of adapting the numerical method in order to avoid these low mobility values, the model needs to be revised in order to describe the foam process at the front more accurately.

6.1.3. SUMMARY

In summary, we can conclude that highly non-linear parameters in the diffusion equation cause temporal instabilities that are non-physical, which can be mollified by improving the discretization of the scheme. Physical instabilities behind the front are inherent to the non-linearity in the mobility of foam. A numerical scheme that resolves both the gas-foam interface and the foam-water interface accurately, is recommended.

6.2. SUGGESTIONS FOR FUTURE RESEARCH

6.2.1. IMPROVED MODEL FOR GAS-FOAM FRONT

A next step forward could be to use a more complex model, describing the gas-foam front directly instead of indirectly as for the current local-equilibrium model studied in this thesis. The population balance model contains an extra equation for the bubble density, which means that we have an additional degree of freedom per grid block. However, the

gain in stability is making up for this deficiency, because a lower resolution grid can be applied.

6.2.2. ADAPTIVE GRID METHODS

Also, adaptive grid methods, that have a higher resolution around the gas-foam interface, the foam-water interface and the injection well, are recommended in order to increase the accuracy of the outcome and reduce the overall computational costs by allowing a low resolution in the rest of the reservoir. However, one needs to take into account that the gas-foam transition is taking place on a scale that is several orders in magnitude smaller than the reservoir scale, and hence the refinement of the grid might not be enough to solve all stability issues arising from the drop in mobility at the gas-foam interface.

6.2.3. BUBBLE-FLOW MODELS FOR POROUS MEDIA

From a scientific point of view it would be interesting to study the inflow of gas in a foam filled porous medium, where one includes the effects of gas trapping, foam breakage and coalescence on pore-scale. Bubbly flow has been studied extensively in other areas, but in porous media flow the main efforts have been made in experimental work (Among many others [4–9]). For simulators there lie a lot of opportunities for modeling foam in porous media on the pore-scale. For example, one could apply the volume-of-fluid method [10] or use the Lattice-Boltzmann equations to model bubbles in a porous medium (See for example for the modeling of bubbly flow [11–13]). This could lead to new insights that can be utilized when improving the models for foam in porous media on a larger scale.

6.2.4. INFLUENCE OF OIL ON THE STABILITY OF FOAM EOR

Finally, the influence of oil on foam flow in porous media is not treated in this thesis, but is still largely unknown. There are some experimental and modeling studies about this topic [14–18], but good simulations that support the results from these studies are not available. Rather, they suffer from hysteresis effects and instabilities, especially when a local-equilibrium model is used. Because the oil relative permeability adds another highly non-linear effect to the model, this poses an additional challenge on numerical solvers. Apart from this, there is mixing of phases, which makes local-equilibrium models a poor choice for these kind of physics. We recommend to extend the phase-change techniques that were studied in Chapter 3 to foam models that include oil. In that case more phase interfaces have to be tracked and solved for. Insights from experimental studies could help to provide appropriate interface conditions to avoid numerical instabilities. Moreover, the linear stability analysis of Chapter 5 can be extended to models that include oil.

REFERENCES

- [1] R. Farajzadeh, A. A. Eftekhari, H. Hajibeygi, S. Kahrobaei, J. M. van der Meer, S. Vincent-Bonnieu, and W. R. Rossen, *Simulation of instabilities and fingering in*

- surfactant alternating gas (SAG) foam enhanced oil recovery*, *Journal of Natural Gas Science and Engineering* **34**, 1191 (2016).
- [2] Q. Chen, M. G. Gerritsen, and A. R. Kavscek, *Modeling foam displacement with the local-equilibrium approximation: theory and experimental verification*, *Society of Petroleum Engineers Journal* **15**, 171 (2010).
- [3] W. R. Rossen, *Numerical Challenges in Foam Simulation : A Review*, in *SPE Annual Technical Conference and Exhibition held in New Orleans*, October (SPE International, New Orleans, 2013).
- [4] Z. Khatib, G. Hirasaki, and A. Falls, *Effects of Capillary Pressure on Coalescence and Phase Mobilities in Foams Flowing Through Porous Media*, *SPE Reservoir Engineering* **3**, 919 (1988).
- [5] Z. F. Zhang, V. L. Freedman, and L. Zhong, *Foam Transport in Porous Media – A Review*, Doe (2009).
- [6] F. A. Skoreyko, A. P. Villavicencio, H. Rodriguez Prada, and Q. P. Nguyen, *Development of a New Foam EOR Model From Laboratory and Field Data of the Naturally Fractured Cantarell Field*, in *SPE Reservoir Characterisation and Simulation Conference and Exhibition* (Society of Petroleum Engineers, 2011).
- [7] L. Kapetas, W. van El, and W. R. Rossen, *Representing Slow Foam Dynamics in Laboratory Corefloods for Foam Enhanced Oil Recovery*, *SPE Improved Oil Recovery Symposium* (2014), 10.2118/169059-MS.
- [8] J. Gauteplass, K. Chaudhary, A. R. Kavscek, and M. A. Fern, *Pore-level foam generation and flow for mobility control in fractured systems*, *Colloids and Surfaces A: Physicochemical and Engineering Aspects* **468** (2015), 10.1016/j.colsurfa.2014.12.043.
- [9] R. Farajzadeh, M. Lotfollahi, A. Eftekhari, W. R. Rossen, and G. J. H. Hirasaki, *Effect of Permeability on Implicit-Texture Foam Model Parameters and the Limiting Capillary Pressure*, *Energy & Fuels* **29**, 3011 (2015).
- [10] A. Q. Raeini, M. J. Blunt, and B. Bijeljic, *Modelling two-phase flow in porous media at the pore scale using the volume-of-fluid method*, (2012).
- [11] O. Busaryev, T. K. Dey, H. Wang, and Z. Ren, *Animating bubble interactions in a liquid foam*, *ACM Transactions on Graphics* **31**, 1 (2012).
- [12] S. Shu and N. Yang, *Direct Numerical Simulation of Bubble Dynamics Using Phase-Field Model and Lattice Boltzmann Method*, *Industrial & Engineering Chemistry Research* **52**, 11391 (2013).
- [13] D. Anderl, M. Bauer, C. Rauh, U. Rde, and A. Delgado, *Numerical Simulation of Bubbles in Shear Flow*, *Pamm* **14**, 667 (2014).

- [14] K. Mannhardt, J. Novosad, and L. Schramm, *Comparative Evaluation of Foam Stability to Oil*, *SPE Reservoir Evaluation & Engineering* **3**, 23 (2000).
- [15] T. J. Myers and C. J. Radke, *Transient Foam Displacement in the Presence of Residual Oil: Experiment and Simulation Using a Population-Balance Model*, *Ind. Eng. Chem. Res.* **39**, 2725 (2000).
- [16] M. Namdar Zanganeh, S. I. Kam, T. LaForce, and W. R. Rossen, *The Method of Characteristics Applied to Oil Displacement by Foam*, *SPE Journal* **16**, 8 (2011).
- [17] R. Farajzadeh, A. Andrianov, R. Krastev, G. J. Hirasaki, and W. R. Rossen, *Foam–oil interaction in porous media: implications for foam assisted enhanced oil recovery*, *Elsevier - Advances in Colloid and Interface Science* **183–184**, 1 (2012).
- [18] J. Tang, M. Ansari, and W. Rossen, *Modelling the Effect of Oil on Foam for EOR*, in *ECMOR XV - 15th European Conference on the Mathematics of Oil Recovery* (2016).

ACKNOWLEDGEMENTS

First of all I would like to thank my promotor, Prof. Jan Dirk Jansen. I appreciate his broad knowledge in the field of geosciences and engineering and his special interest in the mathematical sides of it. We are both fascinated by mathematics, an interest which he always encouraged me to pursue further. Also, I'm very thankful for all the opportunities I had to broaden my view through visiting research groups and conferences all over the world.

Secondly, I would like to thank my copromotor, Dr. Matthias Möller for his support during the second phase of my PhD. He assisted me with the necessary mathematical background of my research and his comments on my work were always very thorough and insightful.

Thirdly, I would like to acknowledge Dr. Hans Kraaijevanger, my supervisor from Shell, who has helped me with the oscillation studies of my thesis. His good eye for small details was very helpful, and he has learned me to be a more accurate writer, especially when it comes to notation. I also thank my other supervisors from Shell, Dr. Hans Groot and Dr. Johan Romate, who assisted me during the first and last phase of my PhD, respectively.

I'd like to thank Prof. William Rossen for all the useful discussions we had about foam. Without his assistance it would have been difficult to gain all the necessary knowledge in the area of foam enhanced oil recovery. Also, many thanks to Prof. Hans Bruining, who helped me to gain a better insight in the field of Geosciences, and guided me now and then during the last years of my PhD.

Furthermore I would like to thank my first supervisor, Dr. Daniel van Odyck, who left after the first year of my PhD, for his assistance during this year. Moreover, thanks to Dr. Hadi Haijbegi, for his help and good suggestions, and for his enthusiasm in research, which is very motivating.

I'm grateful for the possibility to visit the research group of Petroleum engineering in Stanford for a few weeks and present my research there. Many thanks also to the ICES group at the University of Texas in Austin for their kind invitation to visit the group and present my work. Moreover, I would like to thank the people of the Centre for Scientific Computing at the University of Cambridge to provide me with the opportunity to visit and help me with building my own reservoir simulator.

Of course I would also like to give a warm thanks to my colleagues, friends and house mates, who made my time in Delft so much more enjoyable. Thanks also to friends from Groningen and Texel, in particular Evelien, Ariane and Emma; although we live quite far apart, you would always find time to visit. And thank you dear Roberto, for showing up in my life when I least expected it, and for giving me a very good reason to finish my thesis as soon as possible.

Finally I would like to acknowledge my brothers, Anton and Luuk for making me very proud to be their sister. A special thanks to my brother Anton and his girlfriend

Anaïs, who were always there for me during my years in Delft. Many thanks also to my parents, for encouraging me to keep learning and challenging myself. For always buying me more books, which is something I can't have enough of. And although I still do not agree with the saying "Wie A zegt moet B zeggen" ("In for a penny, in for a pound"), I do acknowledge some truth in it, as it became such a part of me that quitting is often not an option. So thanks even for teaching me this, because without it this thesis would not have been there.

A

APPENDIX A: DERIVATION TWO-PHASE FLOW EQUATIONS

In the following sections we give a derivation of the non-dimensional incompressible, immiscible two-phase flow equations for gas, foam and water in a porous medium.

A.1. CONSERVATION LAWS

Mass conservation of each phase, is described by a mass-balance equation for the phase saturation $S_\alpha \in [0, 1]$, given by

$$\phi \partial_t S_\alpha = -\nabla \cdot \mathbf{u}_\alpha, \quad (\text{A.1})$$

where the subscript $\alpha \in \{w, g, f\}$ denotes the phase (water, gas or foam in this case), ϕ denotes the reservoir porosity, and \mathbf{u}_α the phase velocity that is given by

$$\mathbf{u}_\alpha = -\lambda_\alpha (\nabla P_\alpha + \rho_\alpha \mathbf{g}). \quad (\text{A.2})$$

Here P_α is the phase pressure, ρ_α is the phase density, \mathbf{g} is the gravitational force, and λ_α is the phase mobility

$$\lambda_\alpha = k \frac{k_{r\alpha}(S_\alpha)}{\mu_\alpha}, \quad (\text{A.3})$$

where k is the absolute permeability, μ_α the phase viscosity and $k_{r\alpha}$ the phase relative permeability, which is defined in the main part of this article.

A.2. TWO-PHASE FLOW

In case of two fluids, the difference between the phase pressures is described by the capillary pressure, defined as

$$P_c \equiv P_w - P_g, \quad (\text{A.4})$$

such that

$$\mathbf{u}_w = -\lambda_w (\nabla P_c + \nabla P_g + \rho_w \mathbf{g}), \quad (\text{A.5})$$

$$\mathbf{u}_g = -\lambda_g (\nabla P_g + \rho_g \mathbf{g}). \quad (\text{A.6})$$

The total velocity, which is the sum of the phase velocities, is thus equal to

$$\mathbf{u} = -[\lambda_T \nabla P_g + \lambda_w \nabla P_c + (\lambda_w \rho_w + \lambda_g \rho_g) \mathbf{g}], \quad (\text{A.7})$$

where λ_T is the total mobility (sum of mobilities). Hence, we can express the phase velocity of water in terms of the total velocity as follows

$$\begin{aligned} \mathbf{u}_w &= -\lambda_w \nabla P_c + \frac{\lambda_w}{\lambda_T} (\mathbf{u} + \lambda_w \nabla P_c + \lambda_g (\rho_g - \rho_w) \mathbf{g}) \\ &= \frac{\lambda_w}{\lambda_T} \mathbf{u} - \frac{\lambda_w \lambda_g}{\lambda_T} (\nabla P_c + \Delta \rho \mathbf{g}) \\ &= f_w \mathbf{u} - \lambda_w f_g (\nabla P_c + \Delta \rho \mathbf{g}), \end{aligned} \quad (\text{A.8})$$

where $f_\alpha = \lambda_\alpha / \lambda_T$ is the phase fractional flow function and $\Delta \rho = \rho_w - \rho_g$. Hence we can express Eq. A.1 as

$$\phi \partial_t S_w = -\nabla \cdot (f_w (\mathbf{u} - \lambda_g (P'_c \nabla S_w + \Delta \rho \mathbf{g}))), \quad (\text{A.9})$$

where P'_c is the derivative of the capillary pressure with respect to the phase saturation [1], that is approximated by

$$P'_c = \sqrt{\frac{\phi}{k}} \gamma_{gw} \sin(\theta). \quad (\text{A.10})$$

where γ_{gw} is the interfacial tension between gas and water and θ the tilting angle of the rectangular domain with respect to the gravitational force. From the definition of saturation it follows that the sum of the phase saturations is one everywhere, i.e.

$$\sum_{\alpha} S_{\alpha} = 1, \text{ with } \alpha \in \{w, g\}, \quad (\text{A.11})$$

so that we only have to solve for one phase. Hence, Eq. A.8, A.9 and A.11 imply that

$$\nabla \cdot \mathbf{u} = 0. \quad (\text{A.12})$$

which describes the pressure decay in the porous medium.

A.3. NON-DIMENSIONAL FORMULATION

To reduce the number of parameters we scale the model given by Eq. A.1, A.2 and A.12, in a similar way as done by Riaz and Tchelepi [1]. If we let U be a characteristic velocity scale, L a characteristic length scale of the model, and W a characteristic width scale,

such that $A = L/W$ is the aspect ratio, we can scale the other variables as follows

$$x = L\tilde{x}, \quad (\text{A.13})$$

$$y = W\tilde{y}, \quad (\text{A.14})$$

$$\nabla = \frac{\tilde{\nabla}}{L}, \quad (\text{A.15})$$

$$\mathbf{u} = U\tilde{\mathbf{u}}, \quad (\text{A.16})$$

$$t = \frac{\phi L(1 - S_{wc} - S_{gr})}{U} \tilde{t}, \quad (\text{A.17})$$

$$P = \frac{\mu UL}{k} \tilde{P}, \quad (\text{A.18})$$

$$P'_c = \gamma_{gw} \sqrt{\frac{\phi}{k}} \tilde{P}'_c, \quad (\text{A.19})$$

where the tilde denotes a non-dimensional variable. The relative permeability functions are scaled by their endpoint relative permeabilities, i.e. the relative permeability of the residual water and gas saturation, $k_{rwe} = k_{rw}(S_{gr})$ and $k_{rge} = k_{rg}(1 - S_{wc})$, respectively. The gas saturation is normalized by $\tilde{S}_g = \frac{(S_g - S_{gr})}{(1 - S_{wc} - S_{gr})}$. Substituting these variables into the two-dimensional model leads to a non-dimensional system of the form

$$\partial_{\tilde{t}} \tilde{S}_g = -\tilde{\nabla} \cdot \left[M \frac{\tilde{k}_{rg}}{\tilde{\lambda}} \left(\tilde{\mathbf{u}} - \frac{\tilde{k}_{rw}}{N_{ca}} \tilde{P}'_c \tilde{\nabla} \tilde{S}_g - \tilde{k}_{rw} \frac{G}{M} \tilde{\nabla} z \right) \right], \quad (\text{A.20})$$

$$\tilde{\mathbf{u}} = -\tilde{\lambda}_w \tilde{\nabla} \tilde{P}_c - \tilde{\lambda} \tilde{\nabla} \tilde{P}_g - \lambda_w G \nabla z, \quad (\text{A.21})$$

$$\tilde{\nabla} \tilde{\mathbf{u}} = \mathbf{0}, \quad (\text{A.22})$$

where $\tilde{\lambda} = M\tilde{k}_{rg} + \tilde{k}_{rw}$ is the dimensionless mobility function. Here, the variables M , G and N_c denote the end-point mobility ratio, gravity number and capillary number respectively, which are given by

$$M = \frac{\mu_w k_{rge}}{\mu_g k_{rwe}}, \quad (\text{A.23})$$

$$G = \frac{k\Delta\rho g}{\mu_g U}, \quad (\text{A.24})$$

$$N_{ca} = \frac{U\mu_w}{\gamma_{gw} \sin(\theta)}, \quad (\text{A.25})$$

where g is the magnitude of the gravitational force. The mobility ratio together with the dimensionless foam parameters R , κ and S_w^* , the dimensionless injection rate \tilde{I} and the porosity ϕ , determine the entire behavior of the fluids for a certain initial boundary value problem. In the rest of the article we will drop the tilde for readability and define $S \equiv S_g$ and $f \equiv \frac{k_{rg}M}{\lambda}$.

REFERENCES

- [1] A. Riaz and H. A. Tchelepi, *Linear stability analysis of immiscible two-phase flow in porous media with capillary dispersion and density variation*, [Physics of Fluids](#) **16**, 4727 (2004).

B

APPENDIX B: DERIVATION PERTURBATION EQUATIONS

Here we derive the equations used for the stability analysis, that is described in Riaz and Tchelepi [1]. For this we rewrite Eq. 5.1 and 5.2 in terms of the transformed variable $\xi = x - v_s t$, y and t , so that

$$\partial_t S - v_s \partial_\xi S + \nabla \cdot (k_{rw} \nabla \bar{P}) = 0, \quad (\text{B.1})$$

$$\nabla \cdot \left(\lambda \nabla \bar{P} - G k_{rg} \nabla z - \frac{k_{rg}}{\text{Ca}} P'_c \nabla S \right) = 0 \quad (\text{B.2})$$

Substitute $(S, P)(\xi, y, t) = (S_0, P_0)(\xi) + (\hat{s}, \hat{p})(\xi) e^{iny + \sigma t}$ in Eq. B.1 gives

$$\partial_t S - v_s \partial_\xi S + \partial_{xi} (k_{rw} \partial_{xi} \bar{P}) + \partial_y (k_{rw} \partial_y \bar{P}) = 0, \quad (\text{B.3})$$

and hence,

$$\partial_t S + \partial_\xi (k_{rw} \partial_\xi \bar{P} - v_s S) + k_{rw} \partial_{yy} \bar{P} + k'_{rw} \partial_y S \partial_y \bar{P} = 0. \quad (\text{B.4})$$

Evaluating all derivatives to y and t leads to

$$\begin{aligned} \sigma \hat{s} e^{iny + \sigma t} + \partial_\xi \left(k_{rw} \left(P'_0 + \hat{p}' e^{iny + \sigma t} \right) - v_s \left(S_0 + \hat{s} e^{iny + \sigma t} \right) \right) \\ = n^2 k_{rw} \hat{p} e^{iny + \sigma t} + n^2 k'_{rw} \hat{s} \hat{p} (e^{iny + \sigma t})^2. \end{aligned} \quad (\text{B.5})$$

Multiplying the equation with $e^{-(iny + \sigma t)}$ gives

$$\begin{aligned} \sigma \hat{s} + \partial_\xi \left(k_{rw} P'_0 e^{-(iny + \sigma t)} + k_{rw} \hat{p}' - v_s S_0 e^{-(iny + \sigma t)} - v_s \hat{s} \right) \\ = n^2 k_{rw} \hat{p} + n^2 k'_{rw} \hat{s} \hat{p} e^{iny + \sigma t}. \end{aligned} \quad (\text{B.6})$$

Now, we express $k_{rw}(S)$ in terms of S_0 by using a Taylor expansion, such that

$$\begin{aligned} k_{rw}(S) &= k_{rw}(S_0) + k'_{rw}(S_0)(S - S_0) + \mathcal{O}((\Delta S)^2) \\ &= k_{rw}(S_0) + k'_{rw}(S_0) \hat{s} e^{iny + \sigma t} + \mathcal{O}((\hat{s})^2). \end{aligned} \quad (\text{B.7})$$

Substituting this in the above equation we obtain

$$\begin{aligned} & \sigma \hat{s} + \partial_\xi (k_{rw}(S_0) P'_0 e^{-(iny+\sigma t)} + k'_{rw}(S_0) P'_0 \hat{s} + k_{rw}(S_0) \hat{p}' \\ & \quad + k'_{rw}(S_0) \hat{p} \hat{s}' e^{iny+\sigma t} - v_s S_0 e^{-(iny+\sigma t)} - v_s \hat{s}) \\ & = n^2 k_{rw}(S_0) \hat{p} + n^2 k'_{rw}(S_0) \hat{s} \hat{p} e^{iny+\sigma t} + n^2 k''_{rw}(S_0) \hat{s}^2 \hat{p} e^{2(inx+\sigma t)} + \mathcal{O}((\hat{s})^2). \end{aligned} \quad (\text{B.8})$$

Neglecting all the higher order terms that include $\hat{s} \hat{p}$, \hat{s}^2 and $\hat{s} \hat{p}'$, and assuming that $e^{-(iny+\sigma t)} \rightarrow 0$ if $\sigma > 0$ and $t > 0$, we find that

$$\sigma \hat{s} + \partial_\xi (k_{rw}(S_0) \hat{p}' + (k'_{rw}(S_0) P'_0 - v_s) \hat{s}) = n^2 k_{rw}(S_0) \hat{p}. \quad (\text{B.9})$$

We apply the same technique to Eq. B.2, such that

$$\partial_\xi \left(\lambda \partial_\xi \bar{P} - G k_{rg} - \frac{k_{rg}}{\text{Ca}} P'_c \partial_\xi S \right) = -\partial_y \left(\lambda \partial_y \bar{P} - \frac{k_{rg}}{\text{Ca}} P'_c \partial_y S \right), \quad (\text{B.10})$$

so that

$$\begin{aligned} & \partial_\xi \left(\lambda (P'_0 + \hat{p}' e^{iny+\sigma t}) - G k_{rg} - \frac{k_{rg}}{\text{Ca}} P'_c (S'_0 + \hat{s}' e^{iny+\sigma t}) \right) \\ & = n^2 \lambda \hat{p} e^{iny+\sigma t} - n^2 \frac{k_{rg}}{\text{Ca}} P'_c \hat{s} e^{iny+\sigma t}, \end{aligned} \quad (\text{B.11})$$

and hence

$$\begin{aligned} & \partial_\xi \left(\lambda (P'_0 e^{-(iny+\sigma t)} + \hat{p}') - G k_{rg} e^{-(iny+\sigma t)} - \frac{k_{rg}}{\text{Ca}} P'_c (S'_0 e^{-(iny+\sigma t)} + \hat{s}') \right) \\ & = n^2 \lambda \hat{p} - n^2 \frac{k_{rg}}{\text{Ca}} P'_c \hat{s}. \end{aligned} \quad (\text{B.12})$$

We can express $\lambda(S)$, $k_{rg}(S)$ and $P'_c(S)$ in terms of S_0 with a second order accurate Taylor expansion. Neglecting higher order terms, that contain multiples of \hat{s} and \hat{p} or \hat{p}' , and letting $e^{-(iny+\sigma t)} \rightarrow 0$ leads to

$$\partial_\xi \left(\lambda \hat{p}' + \left(\lambda' P'_0 - G k'_{rg} - \frac{1}{\text{Ca}} (k_{rg} P'_c)' S'_0 \right) \hat{s} - \frac{k_{rg}}{\text{Ca}} P'_c \hat{s}' \right) = n^2 \lambda \hat{p} - n^2 \frac{k_{rg}}{\text{Ca}} P'_c \hat{s}. \quad (\text{B.13})$$

Eq. B.9 and B.13 described an eigenvalue problem with eigenvalue σ , in terms of the eigenfunctions \hat{s} and \hat{p} :

$$\sigma \hat{s} + \partial_\xi (k_{rw} \hat{p}' + (k'_{rw} P'_0 - v_s) \hat{s}) = n^2 k_{rw} \hat{p}, \quad (\text{B.14})$$

$$\partial_\xi \left(\lambda \hat{p}' + \left(\lambda' P'_0 - G k'_{rg} - \frac{1}{\text{Ca}} (k_{rg} P'_c)' S'_0 \right) \hat{s} - \frac{k_{rg}}{\text{Ca}} P'_c \hat{s}' \right) = n^2 \lambda \hat{p} - n^2 \frac{k_{rg}}{\text{Ca}} P'_c \hat{s}, \quad (\text{B.15})$$

where the functions k_{rw} , k_{rg} and P_c are functions of S_0 , and the apostrophe denotes the derivative with respect to S_0 or ξ respectively. The base state functions S_0 and P_0 obey the boundary values of the Buckley-Leverett problem and obtain their maximum gradient at $\xi = 0$, and the eigenfunctions $(\hat{s}, \hat{p}) = 0$ and $(\hat{s}', \hat{p}') = 0$ at $\xi = \pm\infty$. This system

can be solved numerically [2], or by matched asymptotic expansions [1].

In the absence of capillarity ($\text{Ca} \rightarrow \infty$) the base state satisfies

$$\frac{S_0}{d\xi} = \delta(\xi), \quad (\text{B.16})$$

$$\frac{dP_0}{d\xi} = \frac{Gk_{rg} - 1}{\lambda}, \quad (\text{B.17})$$

so that it follows from the interface and boundary conditions, that $\hat{s} = c_1 \delta(\xi)$, $\forall \xi \in (-\infty, \infty)$ and $c_1 \in \mathbb{R}$ [1]. Away from the discontinuity at $\xi = 0$, Eq. B.14 implies that

$$\partial_\xi (k_{rw} \hat{p}') = n^2 k_{rw} \hat{p} \Rightarrow \hat{p}'' = n^2 \hat{p} \Rightarrow \hat{p} = c e^{\pm n\xi}. \quad (\text{B.18})$$

Since $\hat{p} = \hat{p}' = 0$ at $\xi = \pm\infty$ it follows that

$$\hat{p}^{+0} = c_2 e^{-n\xi}, \quad \forall \xi > 0, c_2 \in \mathbb{R}, \quad (\text{B.19})$$

$$\hat{p}^{-0} = c_3 e^{+n\xi}, \quad \forall \xi < 0, c_2 \in \mathbb{R}. \quad (\text{B.20})$$

Integrating the full system with capillarity given by Eq. B.14 and B.15 over the discontinuity (from 0^{-0} to 0^{+0}), gives us two equations in terms of p^{+0} , p^{-0} and σ :

$$k_{rw}(S_0(0^{+0}))\hat{p}'^{+0} - k_{rw}(S_0(0^{-0}))\hat{p}'^{-0} = -c_1 \sigma, \quad (\text{B.21})$$

$$\lambda(S_0(0^{+0}))\hat{p}'^{+0} - \lambda(S_0(0^{-0}))\hat{p}'^{-0} = 0. \quad (\text{B.22})$$

Evaluating the indefinite integral of Eq. B.14 over ξ leads to

$$\hat{p}' + c_1(\lambda' P_0 - Gk_{rg})\delta(\xi) = c_4/\lambda + n^2 \int \hat{p} d\xi. \quad (\text{B.23})$$

Rewriting the terms between brackets as $-P_0''/\delta(\xi)$ by differentiating Eq. B.17 with respect to ξ , gives

$$\hat{p}' - c_1 P_0'' = c_4/\lambda + n^2 \int \hat{p} d\xi. \quad (\text{B.24})$$

Integrating this expression over the discontinuity gives a third equation in terms of \hat{p}^{+0} and \hat{p}^{-0} :

$$\hat{p}^{+0} - \hat{p}^{-0} = c_1(P_0'^{+0} - P_0'^{-0}). \quad (\text{B.25})$$

Eq. B.21, B.22 and B.25 then lead to an expression for the disturbance velocity:

$$\frac{\sigma}{n} = \frac{f_{g1} - f_{g0}}{S_1 - S_0} \frac{\lambda_1(1 - Gk_{rg0}) - \lambda_0(1 - Gk_{rg1})}{\lambda_1 - \lambda_0}, \quad (\text{B.26})$$

where the subscripts 0 and 1 denote the front and back edge of the shock respectively.

REFERENCES

- [1] A. Riaz and H. A. Tchelepi, *Stability of two-phase vertical flow in homogeneous porous media*, *Physics of Fluids* **19**, 072103 (2007).
- [2] A. Riaz and H. A. Tchelepi, *Linear stability analysis of immiscible two-phase flow in porous media with capillary dispersion and density variation*, *Physics of Fluids* **16**, 4727 (2004).

C

APPENDIX C: MODEL PARAMETERS

In Table C.1 and Table C.2 the model parameters used in Chapter 5 are listed.

Parameter [unit]	Case 1	Case 2	Case 3	Case 4
foam strength R [-]	$1.8 \cdot 10^4$	$2.5 \cdot 10^4$	$2.5 \cdot 10^4$	$2.5 \cdot 10^4$
critical saturation S_w^* [-]	0.268	0.29	0.29	0.29
foam transition width κ [-]	10^5	10^5	10^4	10^2
end point gas permeability k_{rge} [-]	0.94	0.94	0.94	0.94
end point water permeability k_{rwe} [-]	0.2	0.2	0.2	0.2
gas viscosity μ_g [Pa s]	$5 \cdot 10^{-5}$	$2 \cdot 10^{-5}$	$2 \cdot 10^{-5}$	$2 \cdot 10^{-5}$
water viscosity μ_w [Pa s]	$0.65 \cdot 10^{-3}$	10^{-3}	10^{-3}	10^{-3}
power coefficient gas n_g [-]	1.8	1.3	1.3	1.3
power coefficient water n_w [-]	2	4.2	4.2	4.2
gas density ρ_g [kg m ⁻³]	10^{-5}	10^{-5}	10^{-5}	10^{-5}
water density ρ_w [kg m ⁻³]	10^{-5}	10^{-5}	10^{-5}	10^{-5}
residual gas saturation $S_{g,r}$ [-]	0.0	0.0	0.0	0.0
residual water saturation $S_{w,c}$ [-]	0.0	0.0	0.0	0.0
injected gas saturation $S_{g,inj}$ [-]	1.0	1.0	1.0	1.0
injection rate gas I [m ³ s ⁻¹]	$3.5 \cdot 10^{-5}$	$3.5 \cdot 10^{-5}$	$3.5 \cdot 10^{-5}$	$3.5 \cdot 10^{-5}$
absolute permeability K [m ²]	$5 \cdot 10^{-10}$	$5 \cdot 10^{-10}$	$5 \cdot 10^{-10}$	$5 \cdot 10^{-10}$
porosity ϕ [-]	0.2	0.2	0.2	0.2

Table C.1: Simulation parameters for the four test cases of Farajzadeh *et al.* [1].

Parameter [unit]	Case 5	Case 6	Case 7	Case 8	case 9	case10
R [·]	$1.8 \cdot 10^4$	$1.8 \cdot 10^4$	$2.5 \cdot 10^4$	$2.5 \cdot 10^4$	$1.8 \cdot 10^4$	$5 \cdot 10^4$
S_w^* [·]	0.268	0.268	0.29	0.9	0.5	0.29
κ [·]	10^4	10^2	$6 \cdot 10^4$	10^5	10^5	10^5
μ_g [Pa s]	$5 \cdot 10^{-5}$	$5 \cdot 10^{-5}$	$2 \cdot 10^{-5}$	$2 \cdot 10^{-5}$	$5 \cdot 10^{-5}$	$2 \cdot 10^{-5}$
μ_w [Pa s]	$0.65 \cdot 10^{-3}$	$0.65 \cdot 10^{-3}$	10^{-3}	10^{-3}	$0.65 \cdot 10^{-3}$	10^{-3}
n_g [·]	1.8	1.8	1.3	1.3	1.8	1.3
n_w [·]	2	2	4.2	4.2	2	4.2

Table C.2: Simulation parameters for the additional test cases in Section 5.8 that support the linear stability results of Section 5.3

REFERENCES

- [1] R. Farajzadeh, A. A. Eftekhari, H. Hajibeygi, S. Kahrobaei, J. M. van der Meer, S. Vincent-Bonnieu, and W. R. Rossen, *Simulation of instabilities and fingering in surfactant alternating gas (SAG) foam enhanced oil recovery*, [Journal of Natural Gas Science and Engineering](#) **34**, 1191 (2016).

CURRICULUM VITÆ

Jakolien Marianne van der Meer was born on March 31, 1988, in 's-Gravenhage, The Netherlands.

Between 2000 and 2006 she followed secondary school at OSG De Hogeberg (Texel). After that she began her studies in Mathematics and Chemistry at the University of Umeå (Sweden) in 2006, after which she moved to Groningen to obtain a BSc degree in Mathematics at Rijksuniversiteit Groningen (The Netherlands), between 2007 and 2010. She obtained her MSc degree in Applied Mathematics at the same University. Her MSc thesis, supervised by Dr. F.W. Wubs and Dr. A.E. Sterk, was entitled "The effect of the discretization resolution on the dynamics of an atmospheric PDE model". During this thesis work she spent three months at the Climate Research Center of the University of Exeter (United Kingdom) to investigate the dynamical behavior of the barotropic vorticity model when the discretization resolution is increased.

In December 2012 she started a PhD in Geosciences & Engineering at Technische Universiteit Delft (The Netherlands) on the Numerical Simulation and Optimization of Foam Enhanced Oil Recovery with Prof. dr. J.D. Jansen and Dr. D.E.A. van Odyck. As a PhD candidate she started working on applying higher order numerical solvers to a two-dimensional foam model, for which she wrote her own reservoir simulator in C++. In 2013 she won the Best Poster Award for this work during the second International Conference on Non-Linearities and Upscaling in Porous Media, in Bergen (Norway). After Dr. Van Odyck left the university in 2014, she changed topic, shifting the focus to discretization methods in order to stabilize the model solutions. End 2014 she continued with Dr. M. Möller, working on adaptive grid and advanced averaging methods applied to a one-dimensional foam model. Besides that, she worked on a project studying the stability characteristics of foam flow in porous media, in collaboration with Dr. R. Farajzadeh and Prof. W.R. Rossen. During the second half of 2017 she finished her thesis.

LIST OF PUBLICATIONS

Journal papers

4. **Van der Meer, J. M., M. Möller, and J. D. Jansen**, *Mimetic discretization schemes for phase change problems* (Submitted).
3. **Van der Meer, J. M., J. F. B. M. Kraaijevanger, M. Möller, and J. D. Jansen**, *Discretization schemes for the simulation of foam enhanced oil recovery* (Submitted).
2. **Van der Meer, J. M., R. Farajzadeh, W.R. Rossen, and J. D. Jansen**, *Influence of foam on the stability characteristics of immiscible flow in porous media*, *Physics of Fluids* (Accepted).
1. **Farajzadeh, R., A. A. Eftekhari, H. Hajibeygi, S. Kahrobaei, J. M. van der Meer, S. Vincent-Bonnieu, and W. R. Rossen**, *Simulation of instabilities and fingering in surfactant alternating gas (SAG) foam enhanced oil recovery*, *Journal of Natural Gas Science and Engineering*, 34, 1191–1204 (2016).

Conference papers

4. **Van der Meer, J. M., R. Farajzadeh, and J. D. Jansen**, *Influence of foam on the stability characteristics of immiscible flow in porous media*, In *Proc. SPE Reservoir Simulation Conference (RSC)*, Houston (2017).
3. **Van der Meer, J. M., J. F. B. M. Kraaijevanger, M. Möller, and J. D. Jansen**, *Temporal oscillations in the simulation of foam enhanced oil recovery*, In *Proc. 15th European Conference on Mathematics in Oil Recovery (ECMOR XIV)*, Amsterdam (2016).
2. **Farajzadeh, R., A. A. Eftekhari, H. Hajibeygi, J. M. van der Meer, S. Vincent-Bonnieu, and W. R. Rossen**, *Simulation of instabilities and fingering in surfactant alternating gas (SAG) foam enhanced oil recovery*, In *Proc. SPE Reservoir Simulation Symposium (RSS)*, Houston (2015).
1. **Van der Meer, J. M., D. E. A. van Odyck, P. Wirnsberger, and J. D. Jansen**, *High-order Simulation of Foam Enhanced Oil Recovery*, In *Proc. 14th European Conference on Mathematics in Oil Recovery (ECMOR XIV)*, Catania, pp. 8–11 (2014).

